Photothermal Responses of Noble Metal Nanoparticles under Laser Irradiation: Direct Observation of Nanoscale Heat Dissipation and Its Application to Photoprocessing

KENJI SETOURA

MARCH 2017

Photothermal Responses of Noble Metal Nanoparticles under Laser Irradiation: Direct Observation of Nanoscale Heat Dissipation and Its Application to Photoprocessing

A dissertation submitted to

THE GRADUATE SCHOOL OF ENGINEERING SCIENCE

OSAKA UNIVERSITY

in particular fulfillment of the requirements for the degree of

DOCTOR OF PHILOSOPHY IN ENGINEERING

BY

KENJI SETOURA

MARCH 2017

Abstract

The present thesis describes photothermal effects of noble metal nanoparticles (NPs). The NPs are of great use as nanoscale remote heaters under laser irradiation, owing to the efficient photothermal conversion arising from Localized Surface Plasmon Resonance (LSPR). Controlling temperature elevation of NPs and their surrounding environments through laser irradiation is crucially important for applications of nanoheaters.

In the present thesis, various spectroscopic techniques have been applied for direct observation of nanoscale heat dissipation. Temperature measurement of individual NPs was performed by means of scattering micro-spectroscopy, on the basis of thermal lensing effects around NPs. Ultrafast transient absorption spectroscopy had been performed to measure the dynamics on temperature elevation of NPs in water and subsequent formation of nanobubbles. To gain deeper insights into the control of photothermal effect, numerical models were developed on the basis of Mie theory, general heat diffusion equation, and Navier-Stokes equation. From the comparison between experimental and computational results, it has been revealed that temperature elevation of NPs, diameters of nanobubbles, and fluid convection around NPs can be precisely controlled by changing irradiation parameters of the heating laser. This thesis provides various insights into the control of photothermal conversion of NPs, which are important for a broad range of applications ranging from photodynamic therapy, nanofabrication, to optical manipulation.

Table of Contents

1-1. General Introduction

Nanoparticles (NPs) are small materials between 1 and 100 nm in their size, which exhibit unique electronic/optical properties different from those of bulk materials, molecules, or atoms. These unique properties of NPs arise from various factors depending on the size of NPs, such as the quantum confinement effect and the large surface-to-volume ratio.[1] Noble metals[2], semiconductors[3], carbon[4], and some organic compounds[5] are used as the materials of NPs.

The present thesis deals with nanostructures of noble metals. They exhibit strong light absorption and scattering in the visible to near infrared wavelength region. Optical responses of them vary depending on the size and the shape of nanostructures. The strong interaction between the light and metal nanostructures stems from a collective oscillation of the conduction electrons. The collective oscillation can be resonantly excited under visible light illumination owing to the characteristic permittivity of noble metals. This phenomenon is called as Localized Surface Plasmon Resonance (LSPR).[6,7] Hence, metal nanostructures act as the light antennas in near-field regime, promoting 10^6-fold enhancement of the incident field. Over the last decades, the antenna effect of metal nanostructures has been used for photochemical reactions[8], nonlinear nanophotonics[9], and surface enhanced spectroscopy[10] (Scheme 1-1a).

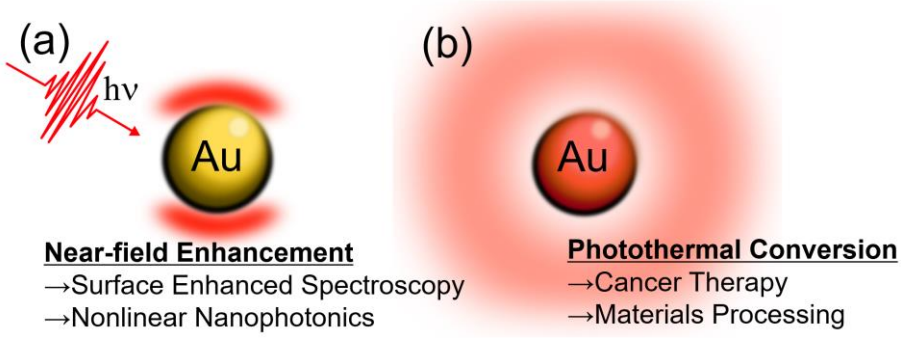

Scheme 1-1. (a) Plasmonic enhancement in the optical near-field. (b) Photothermal conversion under illumination of LSPR band.

On the other hand, most of the photo-energy absorbed by NPs turns into heat owing to low emission yields of noble metals: *e.g.*, $\phi_E < 10^{-6}$ for gold.[11] This means that metal NPs work as nanoscale heat sources upon photoexcitation of LSPR band. The photothermal effect of NPs has been attracting much attention for potential applications in cancer therapy and nanofabrication (Scheme 1-1b).[12] To utilize NPs as the nanoheaters, gold is the suitable material because of its high physicochemical stability at high temperatures.[13]

1-2. Gold Nanoparticles (Au NPs) as Nanoscale Heat Sources

The photothermal effect of Au NPs has attracted growing interest in nanoheater applications, such as photothermal imaging[14], cancer therapy[12], drug delivery[15], nanofabrication[11], and nanobubble generation[16]. While the term '*Plasmonics*' refers to the research field employing the near-field enhancement of LSPR, a new term "*Thermo-plasmonics*" has emerged for the photothermal effect.[17] Before illustrating the scope of this thesis, we briefly review physical aspects of the photothermal conversion in the present section.

Au NPs have LSPR bands around 520 nm that corresponds to electron transitions within the conduction band (6sp band). The peak position of LSPR bands shifts depending on the size, shape of nanostructures, and the refractive index of surrounding environment. In contrast, the 5d-6sp interband transition in the UV region is insensitive to the NP size. For either the intraband and the interband transition, an electronic excitation creates the non-equilibrium Fermi distribution. Excited state dynamics of metal nanostructures has been intensively studied by femtosecond optical pump-probe spectroscopy, and can be described as follows[18]: **i)** the electronic excitation promotes the non-thermal electron distribution, **ii)** after a few hundreds of femtoseconds, a thermal equilibrium is reached obeying the Fermi distribution as a result of electron-electron scattering, **iii)** then the electron energy is transferred to the lattice energy via electron-phonon coupling, **iv)** finally, the lattice energy is dissipated to the surrounding medium, resulting in the cooling of the NP. The relaxation process **i) – vi)** can be described from Two Temperature Model (TTM) [11,18], as shown in Fig. 1-1b. In contrast to the pulsed laser excitation, the temperature increase of Au NPs reaches stationary state under continuous (CW) laser illumination (Fig. 1-1c).[19] The above phenomena indicate that the photothermal effect

of Au NPs can be controlled by changing the irradiation parameters, such as the light intensity or the temporal pulse duration.

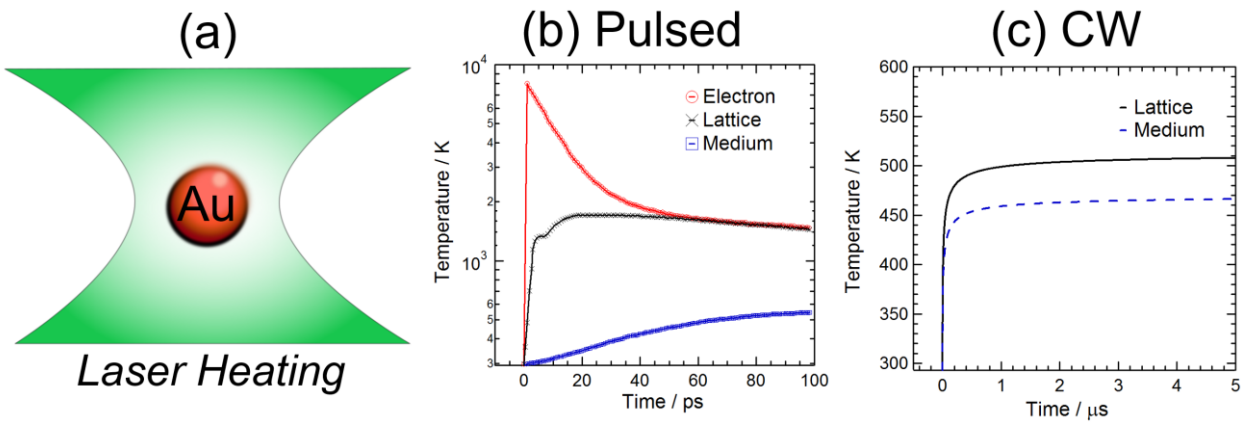

Figure 1-1. (a) A schematic representation (b) Transient temperature changes of Electron, lattice, and medium triggered by the pulsed laser irradiation (c) steady-state heating of an Au NP under CW laser illumination.

1-3. Purpose of the Present Thesis

The relaxation dynamics of LSP, studied by ultrafast time-resolved spectroscopy, revealed that the transient temperature changes of a NP are governed by the general heat diffusion equation.[20] In addition, the stationary temperature increase of a NP under continuous illumination can be predicted from the heat conduction theory.[13,19] Thus, the photothermal response of Au NPs is well understood for the simplified system consisting of a spherical NP and a homogeneous surrounding medium (Scheme 1-2a). In practical cases of the application of photothermal effect, however, one can generally expect that there are complexed surrounding environments around NPs, such as microscopic inhomogeneities in cells or polymer matrices. Further, thermal phase transitions of surrounding environments should be taken into account at high temperatures.

In particular, following three factors should be considered for the detailed elucidation of the photothermal processes: **i)** super heating of the surrounding liquid at temperatures above bulk boiling point, **ii)** nanobubble formation at temperatures above spinodal temperatures, **iii)** thermal convection of liquid medium around an Au NP and a nanobubble. At nanometer scale, it has been reported that liquid water can be superheated

up to 550 K around the surface of an Au NP (Scheme 1-2b).[20] This high temperatures of liquid water can provide a new reaction field for solvothermal chemistry. At temperatures above the spinodal point of the medium, vapor nanobubbles are produced around Au NPs (Scheme 1-2c).[16,20] Nanobubble generation induced by laser irradiation can be used for cancer therapy and nanofabrication. In addition, the nanoscale heating can induce thermal convection of fluid around the focal spot of a laser beam, which has emerged as a method to control the motion of fluid in microscopic region (Scheme 1-2d).[21]

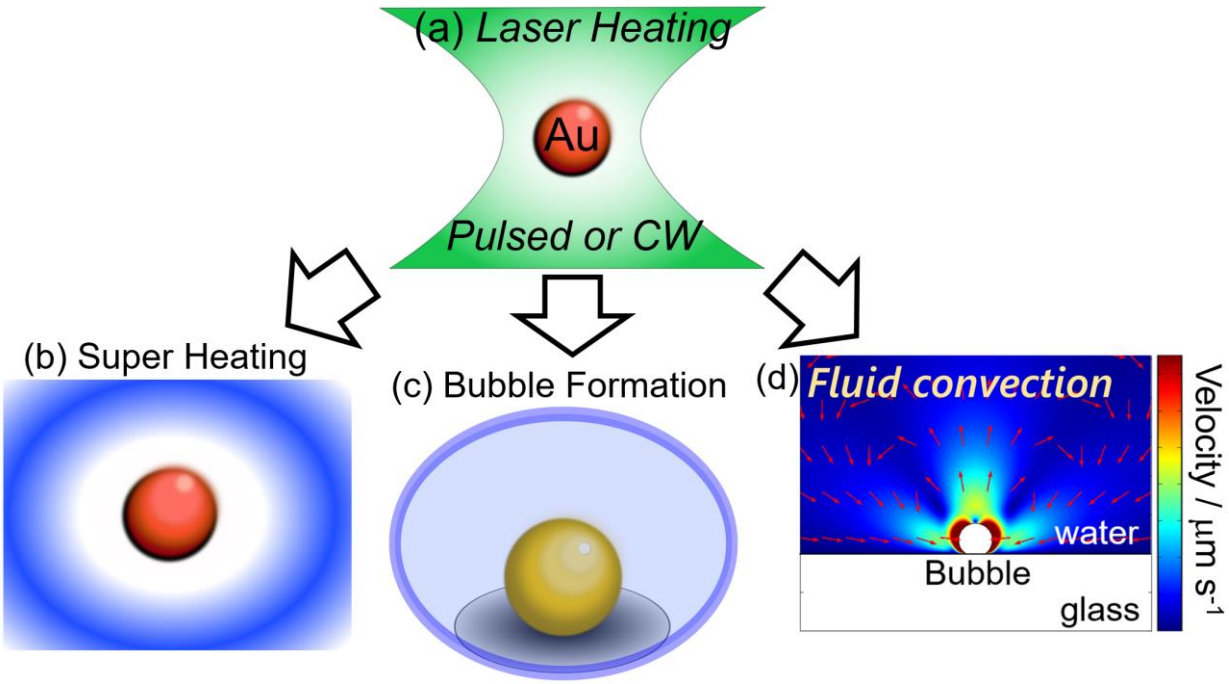

Scheme 1-2. (a) Laser heating (b) super heating of water (c) bubble formation (d) fluid convection around a stationary bubble.

In the present thesis, I have focused on the photothermal effect of Au NPs under the irradiation in the practical and complexed surrounding environments, as shown in Scheme 1-2. The scopes of this work are the elucidation of heat transfer from Au NPs to surrounding environments including solids, liquids or gas, and the demonstration of photothermal nanofabrication.

1-4. Content of This Thesis

The present thesis consists of six chapters including the present introductory part.

Chapter 2 describes a simulation model developed to evaluate the temperature increase of an Au NP under illumination. This model is mainly based on the Mie theory, which describes optical absorption and scattering of a dielectric nanosphere. The photothermal effect on LSPR spectral changes was taken into account by considering the local temperature gradient and the temperature dependent optical properties of the materials. Computational results revealed that LSPR bands shift and damp with as increase in temperature. The temperature-induced shifts in LSPR spectra were used for the direct evaluation of the NP temperature under illumination by spectroscopic techniques.

Chapter 3 reports the picosecond-to-nanosecond dynamics of transient temperature changes of Au NPs and the formation of nanobubbles around Au NPs by means of optical pump-probe spectroscopy. The transient absorption spectra of LSPR bands were analyzed with the numerical model developed in the chapter 2. At low excitation intensity, weak bleaching signals in LSPR bands were detected, indicating the superheating of water layer adjacent to the NP surface. At high excitation intensity, strong scattering signals arising from the formation of nanobubble around Au NPs were obscured. The combination of ultrafast transient extinction spectral measurements and spectral simulations provided insights into the transient vapor nanobubble dynamics.

Chapter 4 presents the temperature measurement of single Au NPs by light scattering micro-spectroscopy. The thermometry under CW laser illumination was performed for individual Au NPs immersed in various surrounding media, such as air, glycerol, and water. The experimental LSPR shifts allowed the estimation of the particle temperature in the range of 300− 700 K with an accuracy of ±20 K on the basis of the modified Mie calculation. The temperature increase of an Au NP in air was roughly 4 times greater than that in water. This result indicated that the thermometry based on the shifts of LSPR spectra is quite sensitive to detect the microscopic inhomogeneity of surrounding medium on heat transfer.

Chapter 5 describes the formation of stationary microbubbles and subsequent fluid convection induced by CW laser heating of Au NPs in water. Once the bubble is generated, the Au NP is thermally insulated from water due to a poor thermal conductivity of the bubble, resulting in the huge temperature jump of NPs. For such

a complex system consisting of an Au NP, the bubble, water, and the glass substrate, I presented a model of photothermal convection by integrating the knowledge obtained in the chapter 2 to 4. It was revealed that a temperature derivative of surface tension at the bubble surface is a key factor to control the fluid convection. The photothermal manipulation and fabrication are demonstrated by controlling the bubble-induced convection through CW laser irradiation.

In chapter 6, I summarize the outcomes and achievements in this thesis as a general conclusion.

REFERENCES

(1) Schmid, G., *Nanoparticles*, Wiley-Vch: Berlin, **2004**.

(2) Moores, A.; Goettmann, F. *New J. Chem*., **2006**, 30, 1121-1132.

(3) Zhang, J. Z., *Acc. Chem. Res*. **1997**, 30, 423-429.

(4) Liu, H.; Ye, T.; Mao, C., *Angew., Chem., Int., Ed*. **2007**, 46, 6473-6475.

(5) Gesquiere, A. J.; Uwada, T.; Asahi, T.; Masuhara, H.; Barbara., P. F. *Nano Lett.* **2005**, 5, 1321-1325.

(6) Keiburg, U.; Vollmer, M. *Optical Properties of Metal Clusters*; Springer, Berlin, **1995**.

(7) Mayer, K. M.; Hafner, J. H. *Chem. Rev.* **2011**, 111, 3828-3857.

(8) Ueno, K.; Misawa, H. *J. Photochem. Photobiol. C* **2013**, 15, 31-52.

(9) Kauranen, M.; Zayats, A. V. *Nature Photonics* **2012**, 6, 737-748.

(10) Stiles, P. L.; Dieringer, J. A.; Shah, N. C.; Van Duyne, R. P. *Annu. Rev. Phys. Chem*. **2008**, 1, 601-626.

(11) Hashimoto, S.; Werner, D.; Uwada, T. *J. Photochem. Photobiol. C* **2012**, 13, 28-54.

(12) Dreaden E. C.; Alkilany, A. M.; Huang, X.; Murphy, C. J.; El-Sayed, M. A. *Chem. Soc. Rev.* **2012**, 41, 2740-2779.

(13) Richardson, H. H.; Govorov, A. O. *Nano today* **2007**, 2, 30-38.

(14) Boyer, D.; Tamarat, P.; Maali, A.; Lounis, B.; Orrit, M. *Science* **2002**, 297, 1160-1163.

(15) Dreaden, E. C.; Austin, L. A.; A Mackey, M. A.; El-Sayed, M. A. *Therapeutic Delivery* **2012**, 3, 457-478.

(16) Lukianova-Hleb, E. Y.; Ren, X.; Sawant, R. R.; Wu, X.; Torchilin, V. P.; O Lapotko, D. O. *Nature Med.* **2013**, 778-784.

(17) Baffou, G.; Quidant, R. *Laser Photonics Rev*. **2013**, 7, 171-187.

(18) Hartland, G. V. *Chem. Rev*. **2011**, 111, 3858–3887.

(19) Keblinski, P.; Cahill, D. G.; Bodapati, A.; Sullivan, C. R.; Taton, T. A. *J. Appl. Phys*. **2006**, 100, 054305.

(20) Siems, A.; Weber, S. A. L.; Boneburg, J.; Plech, A. *New. J. Phys*. **2011**, 3, 043018.

(21) Liu, G. L.; Kim, J.; Lu, Y.; Lee, L. P. *Nature Mater.* **2006**, 5, 27-32.

2. Physical Aspects of Optical Absorption and Scattering of a Dielectric Nanosphere and The Effect of Local Heating

ABSTRACT

Thermometry for single gold nanoparticles (Au NPs) is a crucial technique to elucidate the fundamental aspects of photothermal effects. Information on the temperature of individual Au NPs (placed on glass substrate, and immersed in water / exposed to air) can be directly evaluated through the spectral changes in extinction, absorption, and scattering under pulsed or CW laser irradiation. In the present study, we developed a numerical model for the spectroscopic thermometry on the basis of a concentric core-shell model with Mie theory, which describes optical absorption and scattering of a dielectric nanosphere. The effect of laser heating was taken into account by considering the temperature-dependent dielectric function of gold, and medium refractive index. Spectral damping and blue shifts were mainly attributed to the decrease in refractive index of water, whereas red shifts were observed in air arising from the temperature-dependent intrinsic optical property of gold. The wavelength shifts provide the NP temperature in the range of 300−700 K.

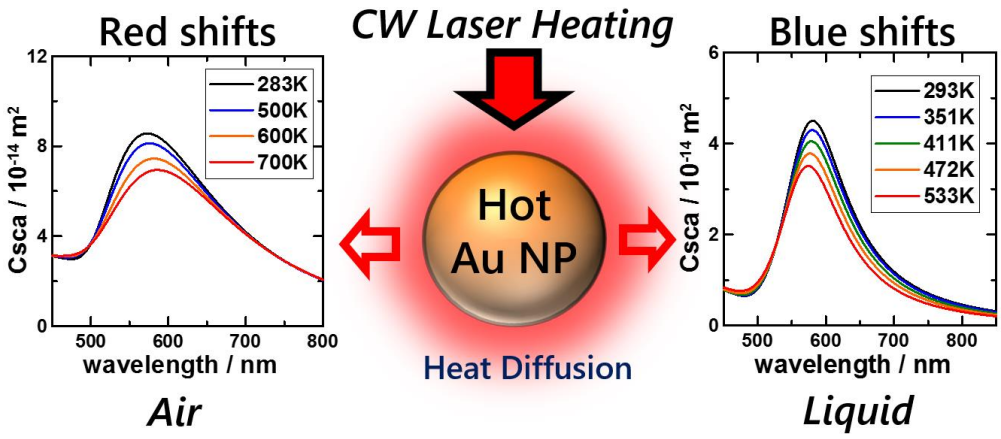

2-1. Introduction

Local temperature around the NP under the irradiation by the laser light at the resonant wavelength is an indispensable physical property for the elucidation of the photothermal response of NPs and surrounding medium. Owing to the small size of NPs (typically ≤ ca. 100 nm), however, it is rather difficult to precisely determine the temperature with high spatial resolution. For this purpose, several methods have been so far proposed and demonstrated as the nanoscale thermometry based on the temperature sensor approach.[1-3] For instance, Kawata group utilized 40-nm diameter Au NPs coated with thermosensitive polymer, poly(N-isopropylacrylamide) (PNIPAM), to monitor the localized heating effect through the spectral shift of SPR (surface plasmon resonance) scattering,[1] which is due to the temperature-dependent change of refractive indices of the surrounding polymer medium through a phase transition from a swollen hydrated state to a shrunken dehydrated state. Although this method could provide the detailed information on the local temperature, the peak shift was quite sensitive to the particle size, coating thickness, and particle−substrate distance. Moreover, it is necessary to obtain the relation between the scattering peak and the temperature for the calibration. Accordingly, it was rather difficult to generally utilize this method for the estimation of the temperature of NPs which have distribution in size and inhomogeneity in the environment.

Carlson and coworkers took another approach using a photo-luminescent thin film of $Al_{0.94}Ga_{0.06}N$ incorporated with Er^{3+} to image the temperature profile around photo-excited gold NP or nanodot lithographically prepared.[2] Also in this measurement, calibration of the sensor was performed to give local temperature of a hot NP by comparing the measured temperature change of a spherical 40-nm Au NP with the theoretical temperature change calculated from the absorption cross section, effective medium refractive index, and effective medium thermal conductivity. This is because the true image size of the temperature profile for the NP is much smaller than the collection volume (~500 nm diameter), and the temperature extracted from the luminescence measurement represents a weighted average temperature from the sample volume. Therefore, the method is not free from the optical diffraction limited size and the spatial resolution as comparable as the particle size was not attained.

In the present work, we adopted more straightforward method for the determination of the temperature of the NP, which is based on the analysis of the LSPR spectral peak shifts induced by CW laser irradiation. The extinction (absorption and scattering) of a single Au NP exhibits temperature-dependence. That is, the spectrum broadens as the temperature increases[4-5] and the temperature dependence of the refractive index of the surrounding medium induce the spectral shift. Although the temperature effect of the SPR broadening of Au NPs has been previously studied in bulk solutions, the spectral shift has been paid little attention.[6-7] This is partly because experimental results are limited for temperature-dependent refractive indices of $n(\omega, T)$ and $\kappa(\omega, T)$ to obtain the complex refractive index defined by $\bar{n} = n + i\kappa$.[8-9] Therefore, temperature-dependent spectra have been explored for only a limited temperature range.[9-10] In the following, we introduce the method of the temperature effect, by acquiring n and κ in wide temperature range to calculate temperature-dependent absorption and scattering cross sections by applying Mie theory.[11] Our method has three advantages: (1) we need no information on the laser beam diameter for the estimation of laser power on samples because the information on the temperature is involved in the experimental scattering spectra, (2) the temperature of the particle can be obtained without using a calibration coefficient such as a heat transfer coefficient[2] that contains unknown parameters, and (3) the particle temperature determined by the present method is not affected by the spatial resolution of the optical setup.

2-2. Mie Theory

In the present section, we will briefly describe the optical properties of Au NPs. First, we consider an electromagnetic interaction between an incident plane wave and a dielectric nanosphere of radius *R* immersed in a homogeneous medium (Scheme 2-1). For the nanosphere smaller than the wavelength of incident light ($R << \lambda$), one can treat the nanosphere as an electric point dipole. This approximation is called as Rayleigh approximation. Au NPs of 10-20 nm in diameter exhibit the absorption maximum around 520 nm, which is insensitive to the size of NPs.[12] In contrast, Au NPs larger than 30 nm in diameter, show spectral shifts to longer wavelength with increasing NP diameter.[13] This size effect arises from size-dependent polarizabilities and highly ordered oscillation modes, such as quadrupole and hexapole modes. The German physicist Gustav Mie solved the Maxwell equations to explain the size-dependent spectral shifts for the system shown in Scheme 2-1, and obtained a set of solutions describing optical absorption and scattering of a nanosphere, which is called as Mie Theory.[11]

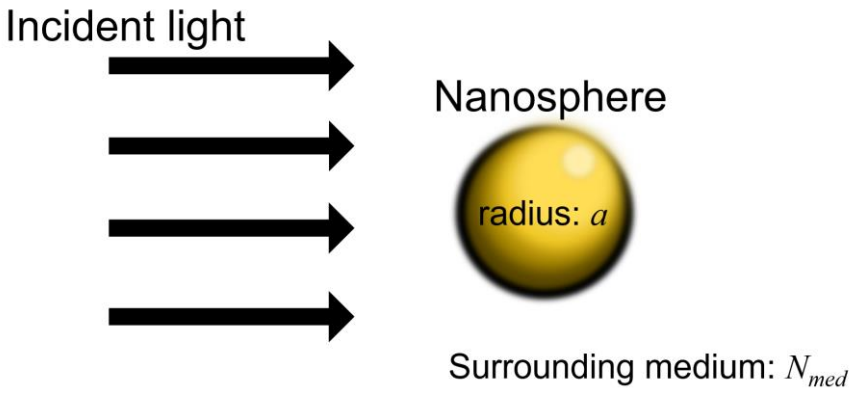

Scheme 2-1. A schematic representation of the optical interaction between an incident plane wave and a dielectric sphere immersed in a homogeneous surrounding medium.

The final formulations of Mie theory for the cross sections in the far field are described as follows:[14-16]

$$C_{ext} = \frac{2\pi}{|k|^2} \sum_{n=1}^{\infty} (2n+1) \operatorname{Re}\{a_n + b_n\} \qquad (2\text{-}1)$$

$$C_{scat} = \frac{2\pi}{|k|^2} \sum_{n=1}^{\infty} (2n+1)\left(|a_n|^2 + |b_n|^2\right) \qquad (2\text{-}2)$$

$$C_{abs} = C_{ext} - C_{scat} \qquad (2\text{-}3)$$

$|k|$ and n are the absolute value of the wave vector of the incident light and the order of oscillation modes: $n = 1$ for the dipole, and $n = 2$ for the quadrupole mode. a_n and b_n representing the scattering coefficients are given by,

$$a_n = \frac{m\psi_n(mx)\psi'_n(x) - \psi_n(x)\psi'_n(mx)}{m\psi_n(mx)\zeta'_n(x) - \zeta_n(x)\psi'_n(mx)} \qquad (2\text{–}4)$$

$$b_n = \frac{\psi_n(mx)\psi'_n(x) - m\psi_n(x)\psi'_n(mx)}{\psi_n(mx)\zeta'_n(x) - \zeta_n(x)\psi'_n(mx)} \qquad (2\text{–}5)$$

$$\psi_n(r) = r j_n(r) \qquad (2\text{-}6)$$

$$\zeta_n(r) = r\left[j_n(r) - i y_n(r)\right] \qquad (2\text{-}7)$$

where m the ratio of the complex refractive index of the sphere to the refractive index of the medium, x the size parameter defined by $(2\pi N_{med}\, a) / \lambda$, ψ_n, ζ_n and their derivatives the Riccati-Bessel functions.

To illustrate the fundamental aspects of optical responses of Au NPs, we show some computational results of Mie theory. Figure 2-1a shows the spectra of extinction cross sections (C_{ext} / m^2), absorption cross sections (C_{abs}), and scattering cross sections (C_{sca}) of a 60-nm-diameter Au NP immersed in water (n_{water}: 1.33). C_{abs} can be obtained by subtracting C_{sca} from C_{ext}, as represented by eq 2-3. LSPR bands can be distinctly observed around 530 nm for C_{ext} and C_{abs}. Figure 2-1b represents the NP size effect on LSPR spectral changes.

The peak position of LSPR bands shift to longer wavelength with an increase in NP diameter. In addition, the broadening in spectral width of LSPR is observed with increasing NP diameter. This significant dependence on the NP size stems from the size-dependent polarizabilities and the highly ordered oscillation modes.

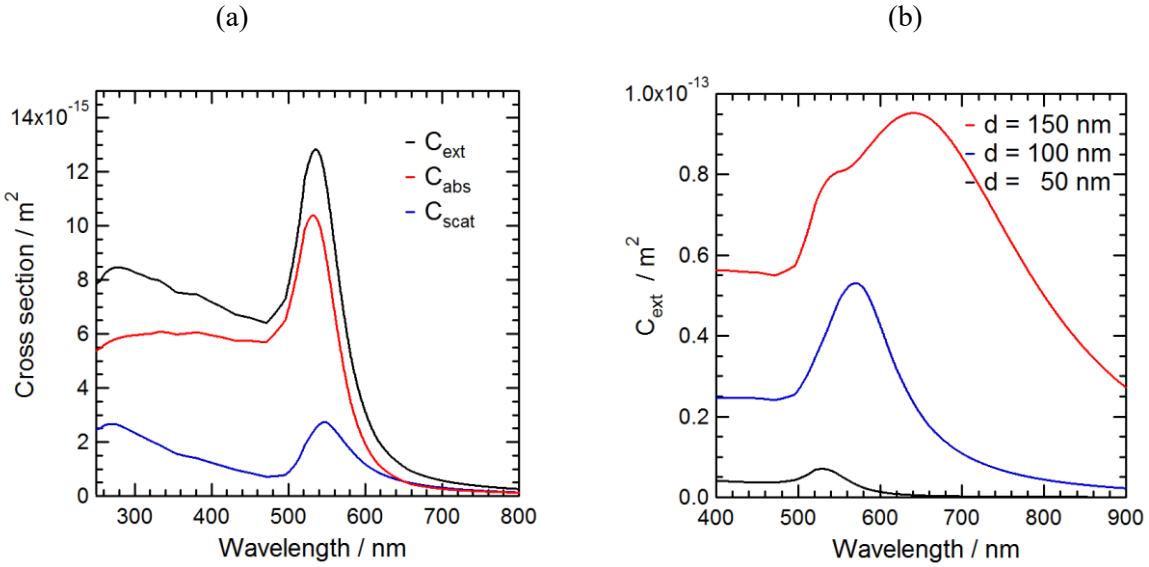

Figure 2-1. (a) Cross sections of C_{ext}, C_{abs} and C_{sca} in m^2 of a 60 nm Au NP in water calculated at room temperature as a function of the wavelength. (b) C_{ext} of a d=50, 100, and 150nm Au NP immersed in water as a function of wavelength.

At room temperature, it is known that the optical spectra calculated from Mie theory well reproduce actual extinction spectra of aqueous colloidal solutions of Au NPs.[13,16] To incorporate the effect of local heating into Mie theory, several factors such as temperature-dependent optical properties of the materials and the temperature distribution around an Au NP should be addressed.

2-3. The Effect of Local Heating: Multi-core-shell model

Dielectric Functions of Gold

Temperature-dependent absorption, scattering, and extinction (sum of absorption and scattering) spectra of an Au NP can be calculated as a function of angular frequency ω or wavelength $\lambda = 2\pi c/\omega$ by applying Mie theory,[11,17] provided that we know temperature-dependent dielectric functions $\varepsilon(\omega, T)$ of the particle, particle radius R, and the permittivity of the surrounding medium ε_m. The dielectric function of gold is defined as the sum of the interband term, $\varepsilon^{IB}(\omega, T)$, corresponding to the transition of 5d electrons to the 6sp conduction band, and the Drude term, $\varepsilon^{D}(\omega, T)$, due to the free conduction electrons (Drude model), as represented by eq 2-8.

$$\varepsilon(\omega,T) = \varepsilon^{IB}(\omega,T) + \varepsilon^{D}(\omega,T) \qquad (2\text{-}8)$$

Each term in eq 2-8 is divided into a real part $(\varepsilon_1(\omega, T) = n_2 - \kappa_2)$ and an imaginary part $(\varepsilon_2(\omega, T) = 2n\kappa)$, where n and κ are respectively the refractive index and the absorption coefficient of the metal.

By using eqs 2-9 and 2-10 [ref. 18,19], we can obtain $\varepsilon^{D}(\omega, T)$ as represented by eq 2-11.

$$\varepsilon^{D}(\omega,T) = \varepsilon_1^{D}(\omega,T) + i\varepsilon_2^{D}(\omega,T) \quad (2\text{-}9)$$

$$\varepsilon^{IB}(\omega,T) = \varepsilon_1^{IB}(\omega,T) + i\varepsilon_2^{IB}(\omega,T) \quad (2\text{-}10)$$

$$\varepsilon^{D}(\omega,T,R) = 1 - \frac{\omega_p^{\,2}}{\varpi(\omega - i\Gamma(T,R))} \qquad (2\text{-}11)$$

$$\Gamma(\omega,T) = \Gamma_{e-e-ph}(T) + A\frac{\upsilon_F}{R} \qquad (2\text{-}12)$$

Here, ω_p, Γ and $\Gamma_{e\text{-}e\text{-}ph}(T)$ respectively are the plasma frequency, the damping frequency, and the damping frequency due to electron−phonon and electron−electron scattering of conduction electrons. v_F is Fermi velocity, and A is a proportionality constant (A = 1 for isotropic electron scattering).

$$\varepsilon^{IB}(\omega,T) = K \cdot \int_{\varpi_g}^{\infty} \left[\frac{\sqrt{y-\varpi_g}}{y} \cdot (1 - f(y,T)) \cdot \frac{y^2 - \varpi^2 + \Gamma_{e-e}{}^2 - i2\varpi\Gamma_{e-e}}{(y^2 - \varpi^2 + \Gamma_{e-e}{}^2) + 4\varpi\Gamma_{e-e}{}^2} \right] \cdot dy \qquad (2\text{-}13)$$

$$f(y,T) = \frac{1}{1 + \exp\left(\frac{E_y - E_F}{k_b T} \right)} \qquad (2\text{-}14)$$

$$\varpi_g = \frac{E_g}{\hbar} \qquad (2\text{-}15)$$

$$y = \frac{E_y}{\hbar} \qquad (2\text{-}16)$$

Here E_g is the interband gap energy of 1.8 eV at the tail, E_y is the electron energy of state, $\Gamma_{e\text{-}e}(T)$ is the damping frequency due to electron−electron scattering of interband electrons, and K is a constant. The function $f(y,T)$ represents the distribution of quasiparticle (plasmon) states. The experimental temperature-dependent dielectric functions of bulk gold have been obtained by Otter at wavelengths from 440 to 640 nm at several temperatures for solid and also for liquid gold.[8] By fitting eqs 2-11 to 2-16 and the Otter's data points at four temperatures 283, 583, 843, and 1193 K, we obtained $\Gamma_{e\text{-}e\text{-}ph}(T)$ and $\Gamma_{e\text{-}e}(T)$ as a function of T. The best fit to reproduce Otter's data was obtained by using parameters: $\Gamma_{e\text{-}e\text{-}ph}(T) = 6.10 \times 10^{11} + 2.97 \times 10^{11} \cdot \mathrm{T}$, $\Gamma_{e\text{-}e}(T) = 2.75 \times 10^{14} + 5.35 \times 10^{10} \cdot \mathrm{T}$, $K = 2.65 \times 10^{24}\ \mathrm{s}^{-3/2}$, and $E_F = 2.55$ eV. Therefore, we were ready to calculate $\varepsilon(\omega, T)$ at any temperature. A satisfactory agreement of experimental and computational $\varepsilon(\omega, T)$ ensures the reliability of calculated optical spectra at given temperatures (Figure 2-2).

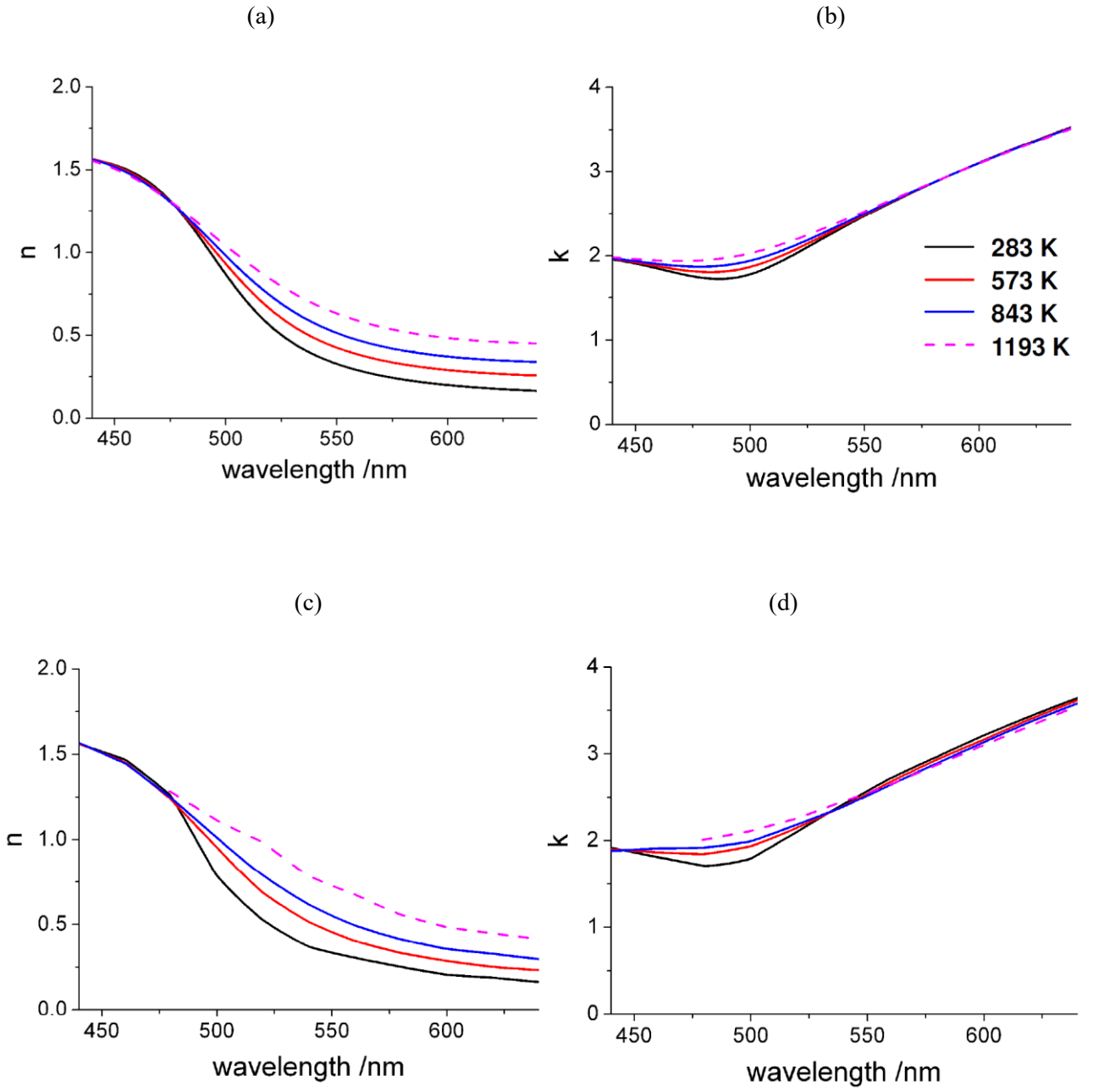

Figure 2-2. (a). Values of n (a) and κ (b) of bulk gold as a function of wavelength at various temperatures by calculated using the equations described in the text. Experimental n (c) and κ (d) values of bulk gold as a function of wavelength at different temperatures by Otter (reproduced from ref. 8).

Multi-Core-Shell Modeling

In general, the refractive index of the medium surrounding Au NP is temperature-dependent as the complex refractive index $\varepsilon(\omega, T)$ of the Au NP is. Therefore, the nonlinear optical properties of Au NP are highly sensitive to the change of the refractive index of the surrounding medium as a result of temperature increase in the close vicinity of an Au NP. Exposure of an Au nanosphere to a focused laser beam generates a temperature distribution in the surrounding medium due to heat-dissipation-induced medium heating (Scheme 2-2a).[20,21]

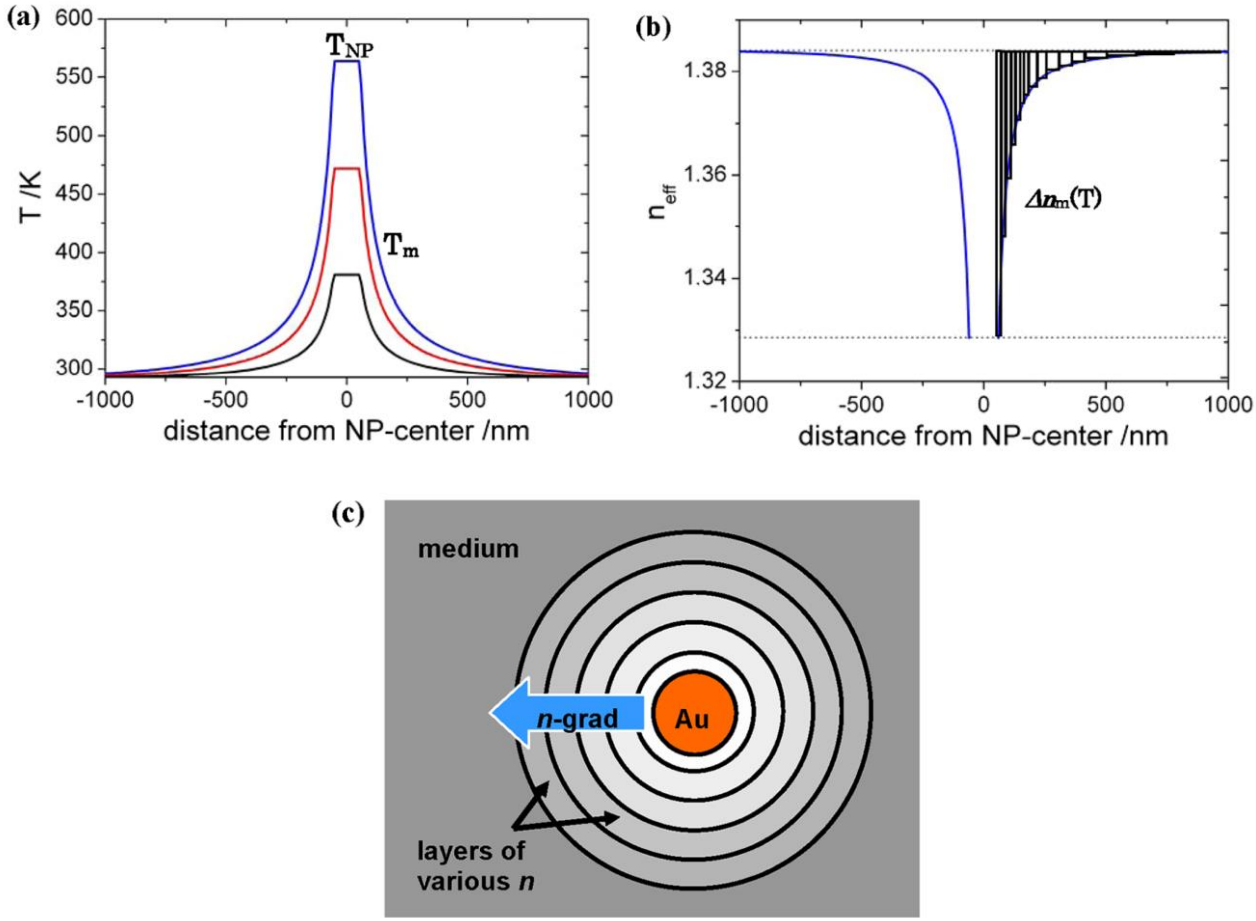

Scheme 2-2. Schematic illustration of the temperature-to- refractive index profile transformation used for numerical simulation: Temperature (a) and refractive index (b) profiles of a 100-nm diameter point heat source and a multi-layered core-shell model.

Note that a steady-state spatial temperature distribution is established under the CW laser excitation, within a few hundreds of nanoseconds.[20] The temperature distribution can be transformed into the spatial profile of the refractive index dependent both on Au NP temperature and the distance from the NP. This temperature dependent refractive index of the medium is treated as a NP-core multi-medium-shell system with each shell exhibiting different refractive index of increasing order from inside to outside (Scheme 2-2b). To calculate the optical properties of the multi core−shell system represented by Scheme 2-2c, we developed a computational program for multilayered spheres as an extension of the formulations of a coated sphere given by Bohren and Huffman.[17] The idea is to digitize the refractive index distribution around the Au NP surrounded by many layers, each of which has a constant refractive index of a few nanometers. By using this treatment, we obtained the extinction (C_{ext}), scattering (C_{sca}), and absorption (C_{abs}) cross sections as a function of wavelength. Quantitative calculations of the temperature-dependent nonlinear optical properties of Au NPs was performed by the combination of the temperature-dependent dielectric functions of an Au sphere with the dielectric constants of surrounding medium based on the model of the multilayered spherical shells.

2-4. Computational Results: Spectral Changes Induced by Laser Heating

Scattering Spectral Changes of a 150-nm-diameter Au NP supported on glass and exposed to air.

In this section, we apply the numerical model developed in the previous section to the elucidation of the temperature effect of the scattering spectrum of the Au NP. First, we treat the Au NP with a 150-nm diameter supported on glass and exposed to air (Scheme 2-3). The refractive index of the surrounding matrix can be assumed to be constant regardless of the temperature, because the temperature coefficients for the refractive indices of a glass substrate and air are quite small (in the order of 10^{-6} K^{-1}) and two magnitudes smaller than that of liquids. In other word, the change of the scattering spectrum is attributable to the temperature-dependent dielectric function of Au.

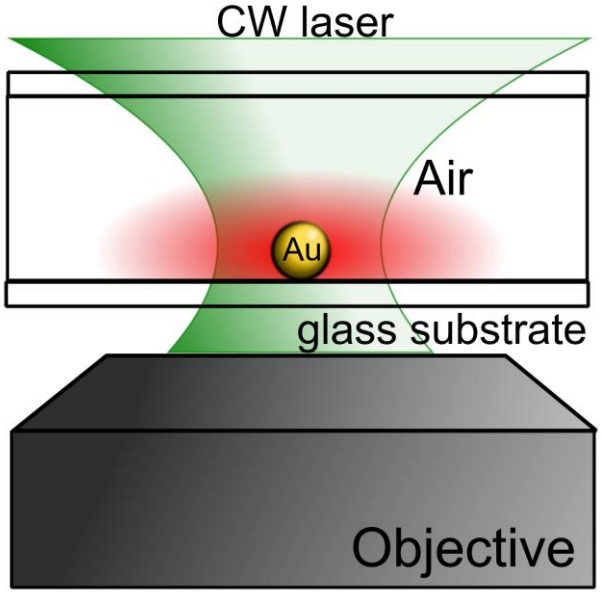

Scheme 2-3. A schematic illustration of heat dissipation for an Au NP supported on a substrate and exposed to air under CW laser illumination.

Figure 2-3a shows the scattering cross section spectra for a 150 nm Au NP calculated at various temperatures. For the calculation, the effective refractive index of the medium was set to be 1.12, whose value was determined by the method described in the literature.[22] Red shifts of the scattering spectra were observed with increasing temperature. These red shifts are ascribed to an intrinsic property of Au NP due to the temperature dependence of the conduction electron scattering frequency.[23,24] As noted just before, the temperature coefficient of the refractive index of air is negligibly small. The peak shift of the calculated spectra is a linear function of the temperature as given in Figure 2-3b. This linear relationship allows the direct evaluation of particle temperature under laser illumination by spectroscopic techniques, even in the surrounding environment which has optical properties insensitive to the temperature.

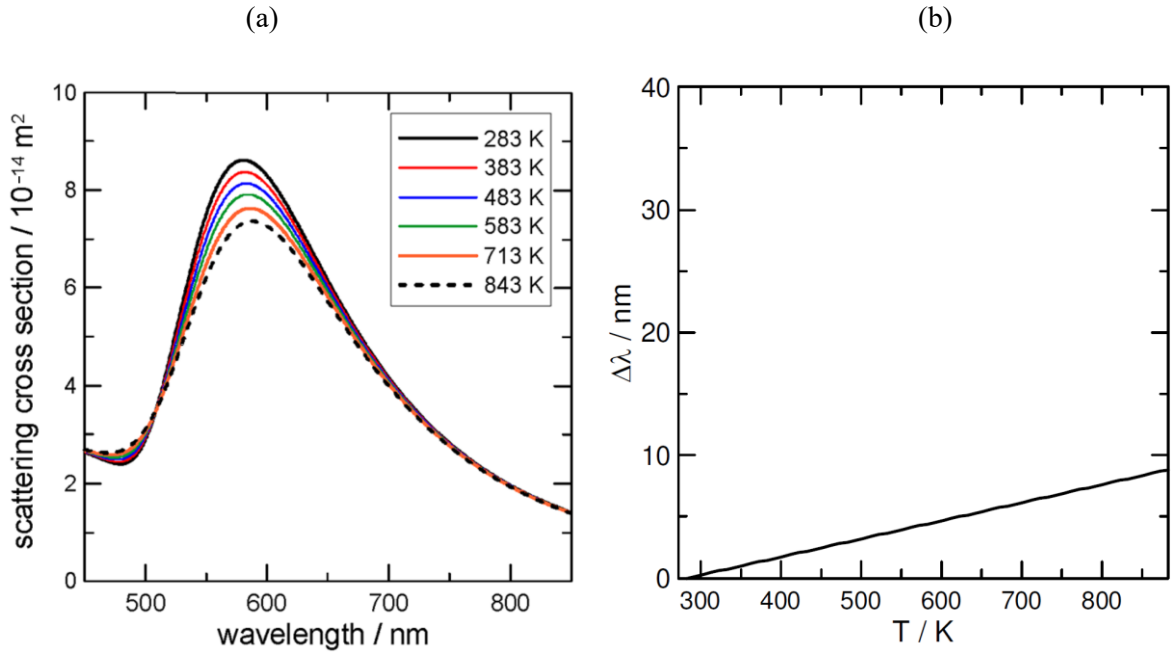

Figure 2-3. (a) Temperature dependence of scattering spectra of Au NP with a 150-nm diameter in the medium with an effective medium refractive index of 1.12, as calculated on the basis of the numerical model developed in section 2-3. (b) Temperature dependence of the peak of the scattering spectra, calculated for the Au NP with a 150-nm diameter.

Scattering Spectra of an Au NP with a 100-nm diameter supported on glass and immersed in liquid media.

In the preceding section, we showed that the scattering spectrum of the Au NP in Glass/Au/air environment exhibits redshifts with an increase in temperature. On the contrary, the calculation predicts temperature-dependent blue shifts both in Glass/Au/water (Figure 2-4a) and in Glass/Au/glycerol (Figure 2-4b) systems. These results suggest that temperature-dependent refractive index changes of the surrounding medium overwhelm the NP's own temperature-dependent optical response in the overall spectral peak position. That is, the blue shifts are due to the decreasing refractive index of the solvents with an increase in temperature. Spectral shifts as a function of NP temperature are summarized in Figure 2-4c and –d. In Figure 2-4c, a parabolic curve is drawn because the temperature dependence of the refractive index for water is parabolic.[25] For glycerol, the curve of $\Delta\lambda$ is linear because of the linearity of the refractive index with temperature.[26] Larger $\Delta\lambda$ values compared with that of water were observed in glycerol, a reflection of its higher *dn/dT* values. Thanks to larger $\Delta\lambda$ values compared with that in air, higher sensitivity to temperature changes can be expected in these liquid media.

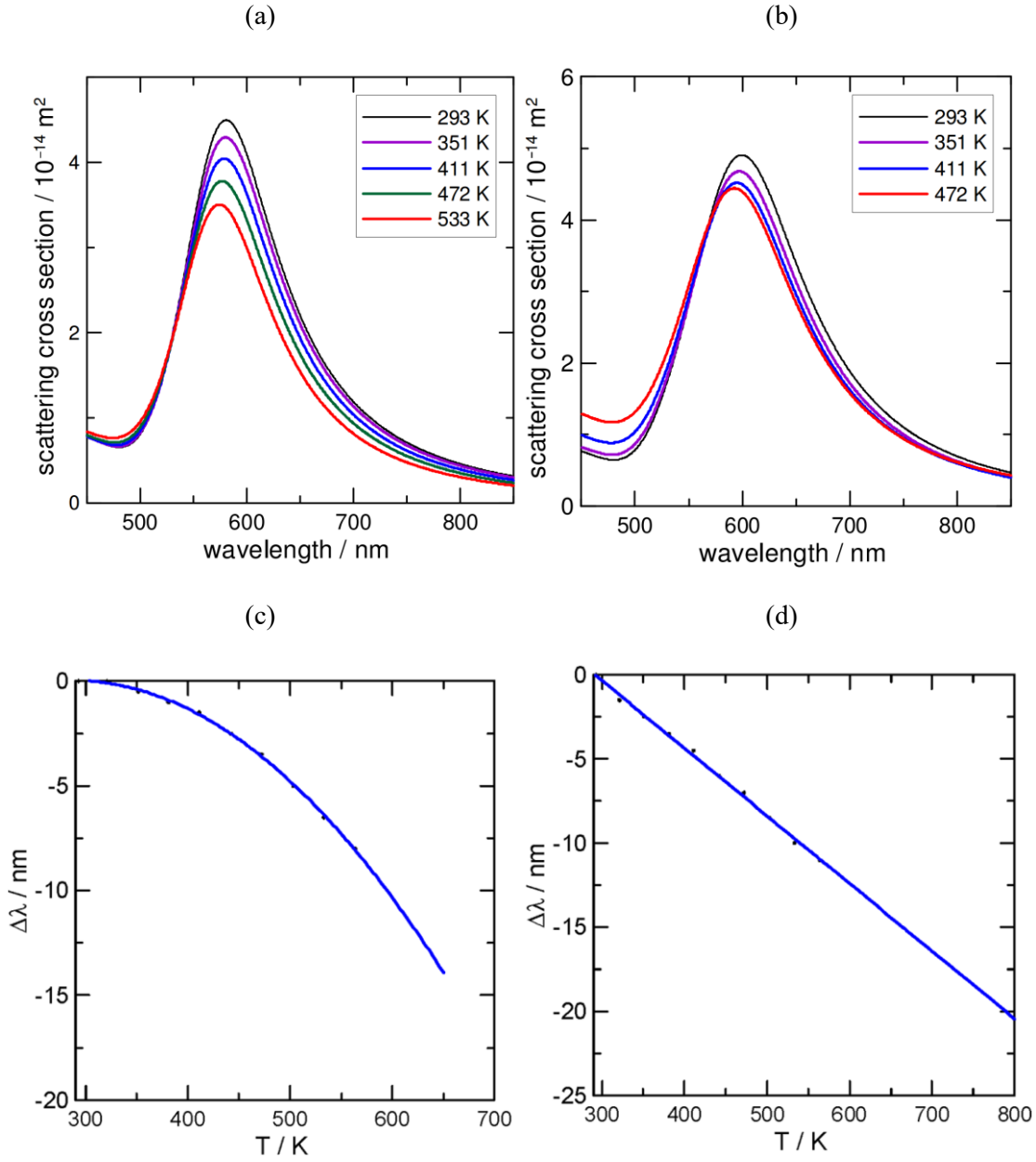

Figure 2-4. (a) Temperature-induced scattering spectral shifts calculated for a single 100-nm diameter Au NP supported on a glass substrate in water. (b) Temperature-induced scattering spectral shifts calculated for a single 100-nm diameter Au NP supported on a glass substrate in glycerol. (c, d) Temperature-dependent curves of $\Delta\lambda$ calculated for a 100-nm diameter Au NP on a glass substrate in water and glycerol.

2-5. Summary and Conclusion

In this chapter, we first reviewed Mie theory describing optical absorption and scattering of a dielectric nanosphere. Next, the effect of laser heating was incorporated into Mie theory by taking the temperature-dependent dielectric function of Au and the multi-core-shell modeling of refractive index of the surrounding medium into account. For single Au NPs supported on a glass substrate, progressive red shifts were observed in air, whereas blue shifts were observed in water and glycerol with increasing temperature. The red shifts in air arose from an intrinsic optical property of Au NP because of negligibly small temperature coefficients of the refractive indices of air and glass. Heating-induced development of medium refractive index gradient is the origin of observed blue shifts in water and glycerol because of large temperature coefficients of the refractive indices in both liquids. The spectral peak shifts enable the estimation of the particle temperature under continuous illumination by spectroscopic techniques. In principle, this method is applicable for pulsed laser heating of Au NPs because the transient changes in optical indices of Au NPs and the surrounding medium can be expected from the heat diffusion equations.

References

(1) Honda, M.; Saito, Y.; Smith, N. I.; Fujita, K.; Kawata, S. *Opt. Express* **2011**, 19, 12375−12383.

(2) Carlson, M.; Khan, A.; Richardson, H. H. *Nano Lett.* **2011**, 11, 1061−1069.

(3) Bendix, P. M.; Reihani, S. N. S.; Oddershede, L. B. *ACS Nano* **2010**, 4, 2256−2262.

(4) Link, S.; El-Sayed, M. A. *Int. Rev. Phys. Chem.* **2000**, 19, 409− 453.

(5) Hartland, G. V. *Annu. Rev. Phys. Chem*. **2006**, 57, 403−430.

(6) Liz-Marzan, L. M.; Mulvaney, P. *New J. Chem*. **1998**, 22, 1285− 1288.

(7) Link, S.; El-Sayed, M. A. *J. Phys. Chem. B* **1999**, 103, 4212− 4217.

(8) Otter, M. *Z. Phys.* **1961**, 161, 539−549.

(9) Palpant, B.; Rashidi-Huyeh, M.; Gallas, B.; Chenot, S.; Fisson, S. *Appl. Phys. Lett*. **2007**, 90, 223105

(10) Lukaianova-Hleb, E. Y.; Sassaroli, E.; Jones, A.; Lapotko, D. O. *Langmuir* **2012**, 28, 4858−4866

(11) Mie, G. *Ann. Phys.* **1908**, 25, 377−445.

(12) Moores, A.; Goettmann, F. *New J. Chem*. **2006**, 30, 1121-1132.

(13) Yamauchi, H.; Ito, S.; Yoshida, K.; Itoh, T.; Tsuboi, Y.; Kitamura, N.; Miyasaka, H. *J. Phys. Chem. C* **2013**, 117, 8388–8396

(14) Keiburg, U.; Vollmer, M. *Optical Properties of Metal Clusters*; Springer: Berlin, **1995**.

(15) Gaponenko, S. V. *Introduction to Nanophotonics*; Cambridge University Press: Cambridge, **2010**.

(16) Garcia, M. A. *J. Phys. D* **2011**, 44, 283001.

(17) Bohren, C. F.; Huffman, D. R. *Absorption and Scattering of Light by Small Particles*; Wiley: New York, **1983**.

(18) Bigot, J.-Y.; Merle, J.-C.; Cregut, O.; Daunois, A. *Phys. Rev. Lett*. **1995**, 75, 4702−4705.

(19) Grua, P.; Bercegol, H. *Proc. SPIE* **2001**, 4347, 579−587

(20) Qin, Z.; Bischof, J. C. *Chem. Soc. Rev*. **2012**, 41, 1191−1217.

(21) Govorov, A. O.; Richardson, H. H. *Nano Today* **2007**, 2,30−38.

(22) Curry, A.; Nusz, G.; Chilkoti, A.; Wax, A. *Opt. Express* **2005**, 13, 2668−2677.

(23) Zhang, Q.; Iwakuma, N.; Sharma, P.; Moudgil, B. M.; Wu, C.; McNeill, J.; Jiang, H.; Grobmyer, S. R. *Nanotechnology* **2009**, 20, 395102.

(24) Wang, Y.; Xie, X.; Wang, X.; Ku, G. K.; Gill, L.; O'Neal, D. P.; Stoica, G.; Wang, L. V. *Nano Lett*. **2004**, 4, 1689−1692

(25) Schiebener, P.; Straub, J.; Levelt Sengers, J. M. H.; Gallegher, J. S. *J. Phys. Chem. Ref. Data* **1990**, 19, 677−717.

(26) Yaltkaya, S.; Aydin, R. *Turk. J. Phy*s. **2002**, 26,41−47.

3. Picosecond-to-Nanosecond Dynamics of Nanobubbles around Aqueous Colloidal Gold Nanoparticles under Picosecond Pulsed Excitation.

ABSTRACT

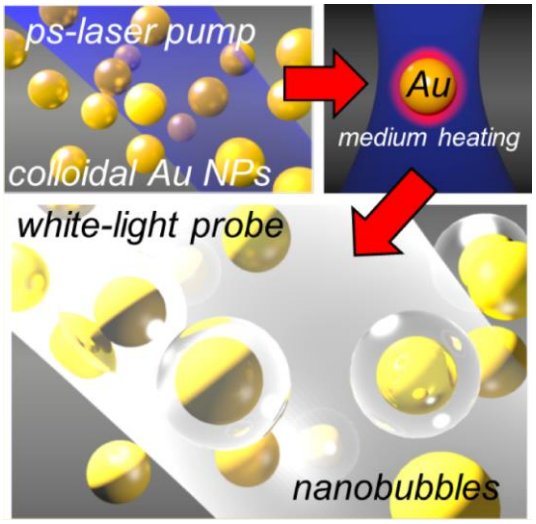

As already discussed in previous sections, temperature of nanoparticles increases by photoexcitation. In this section, we discuss the dynamics of the temperature increase of Au NPs in water induced by the picosecond pulsed excitation, resulting in the formation of nanobubbles around the Au NP.

Generation of nanoscale vapor bubbles around noble metal nanoparticles is of significant interest, not only from the viewpoint of the elucidation of the underlying mechanisms responsible for photothermal effects, but also from the application of photothermal effects such as photothermal cancer therapies. Here, we introduce the dynamics of the formation and evolution of nanobubbles around colloidal gold nanoparticles using picosecond optical pump-probe measurements.

Time-resolved transient spectroscopy clearly detected the temporal evolution of the nanobubble around the colloidal gold nanoparticles with 20 − 150-nm diameters after the 355-nm pulsed laser excitation. Time evolution was analyzed by comparing the experimentally obtained transient extinction spectra with those simulated on the basis of a concentric spherical core−shell model within the framework of Mie theory. From these analyses, the temporal evolution of the diameter of nanobubbles was obtained; *e.g.* the maximum diameter of the bubble was 260 ± 40 nm for the Au NP with a 60-nm diameter excited at the fluence of 5.2 mJ cm^{-2} and the lifetime of this bubble was ca. 10 ns. We also confirmed the suppression of bubble formation by applying the pressure of 60 MPa to the solution and the dynamics under the high pressure was used as a reference for the analysis.

3-1. Introduction

In the previous chapter, we introduced the temperature increase of Au NPs under the photoexcitation and its effect on the extinction spectra. In the present chapter, we discuss the dynamics of the temperature rise and formation of nanobubbles around NPs after the pulsed laser excitation.

As mentioned in previous sections, Au NPs exhibit various fascinating phenomena *via* their interactions with visible light, including the plasmonic enhancement of incident electromagnetic fields.[1,2] This is because visible light excites the localized surface plasmon resonance (LSPR) band, leading to extremely efficient extinctions, that is, the absorption and scattering of incident light. The absorption of light also increases temperatures of NPs as a result of the LSPR decay, in which excited electrons couple with phonons within these NPs. Their photothermal response has been attracting much attention from the viewpoints of the elucidation of the phase changes and the application into the nanoscale energy depositions to the surroundings. In actuality, dynamic behaviors of NPs after the pulsed excitation, such as particle expansion, melting, evaporation, and fragmentation, have been reported.[3–5] As for the effects on the surrounding medium, local heating, acoustic emission, and vapor-bubble generation have been observed.[3–5] In particular, UV and visible laser heating of Au NPs in aqueous solutions induces superheating of the water medium at the interface of the particle and medium, resulting in explosive vapor bubble generation around the particles.[6,7] The transient expansion and collapse of these bubbles attract much attention from the viewpoint of the application of lasers in surgery and medicine such as photothermal therapy of malignant tissues by killing cells nearby.[8,9]

Neumann and Brinkmann investigated the formation of bubbles around NPs using pulsed laser excitation.[10–12] They reported the dynamics of nucleation and initial expansion of the bubble around a single micrometer-sized absorber following microsecond and nanosecond laser irradiation. Transient microbubbles on the particle surface were directly imaged and simultaneously detected by measuring a transient decrease in the transmitted probe laser intensity. Using dark-field microscopy,[13–15] Lapotko and coworkers employed imaging methods and applied optical detection of nanobubbles around single and clustered Au NPs after the nanosecond pulsed excitation.[16–18] They measured the time dependence of optical extinction signals of a bubble around a single Au NP with a 90-nm diameter after exciting the LSPR band.[16] They reported that a

threshold fluence of the bubble formation was 360 mJ cm^{-2} for the excitation condition with a 532 nm laser pulse (0.5 ns fwhm). Using time-resolved X-ray scattering detection with the femtosecond pulsed laser excitation (400 nm, 100 fs), Plech group observed the dynamics of nanobubbles around Au NPs with a 9-nm diameter growing and shrinking within a period of less than a nanosecond.[6] They reported that the bubble generation threshold was 29 mJ cm^{-2} in their excitation condition and the maximum diameter of the bubble of20 nm was attained at 300 ps after the excitation.

In addition to the above studies, several methods have been applied to the detection of the dynamics of NPs after the pulsed irradiation. Among them, single-particle studies using microscopy can provide direct information on the microbubbles free from the ensemble average. NPs usually have distributions in shape, size and, in some case, chemical compositions. Detection of individual NPs can provide the information free from the ensemble averaging of these distributions. Owing to the optical diffraction limit, however, it is rather difficult to apply the imaging to the nanosized object under the optical microscope although a few reports were presented.[16–18]

Ensemble studies using colloidal solutions demonstrated superb detection sensitivity and high-quality nanobubble signals, revealing averaged bubble dynamics, although only indirect evidence of nanobubbles was obtained.[6,7,19,20] Time-resolved X-ray scattering was a powerful tool for the direct detection of the nanoscale dynamics of morphological evolution. Large-scale instrumentation and complicated data analysis are, however, needed to apply the time-resolved detection using X-ray. In contrast, optical spectroscopy uses instrumentation readily available, and the data analysis is simple and straightforward. Plech group applied a transient detection of extinction signals at four monitoring wavelength points (405, 488, 635, and 660 nm) for the measurement of the dynamics of Au NPs with a 80-nm diameter in colloidal solution after the excitation of ns laser pulse (at fluences of 30 and 45 mJ cm^{-2}).[19]

It should be noted that the most of the initial process of bubble formation takes place in the time region shorter than a few ns. Accordingly, pulsed excitation with a ns laser does not provide the detailed information in the initial processes of the dynamics. On the other hand, although the time resolution is sufficiently high, the irradiation of Au NPs with a femtosecond laser pulse easily induces the

photodegradation of Au NPs. This is because the pulse duration of the femtosecond laser pulse is shorter than the time scales of the deactivation of the excited state of the electron in Au NPs and the heat transfer to the surrounding medium. In the pulsed excitation condition, many electrons in one Au NPs could be excited. In the case where the pulse duration of the laser is longer than the time of the heat transfer from the NP to the medium, the rise of the temperature is suppressed. On the other hand, the irradiation by the laser pulse with duration much shorter than the heat transfer induces the drastic increase of the temperature of NPs leading to the morphological change of Au NPs through the melting. On the basis of these previous studies, we have employed picosecond laser pulses to peruse the dynamics of the bubble formation, because the pulse width of the picosecond laser, 15 ps, is sufficiently short to temporarily resolve the bubble formation and longer pulse duration than the femtosecond laser can suppress the degradation of Au NPs. In the following, we discuss the dynamics of the bubble formation and disappearance by showing the experimental results obtained by the picosecond pump and prove spectroscopy and numerical simulations.

3-2. Materials and Methods

Samples. Aqueous solutions of Au NPs with nominal diameters of 20 nm (cat. no. EMGC20, 19 ± 3 nm), 60 nm (cat. no. EMGC60, 58 ± 5nm measured using TEM), 100 nm (cat. no. EMGC100, 100 ± 8 nm), and 150 nm (cat. no. EMGC150, 155 ± 18 nm) were purchased from BBI Solutions (Cardiff, UK) and used without further purification. These particles were synthesized using a variation of the Frens citrate reduction method, and were stabilized with citrate.[21] Five milliliters of the sample solutions (particle concentrations of 7.0×10^{11} mL^{-1} (20 nm), 2.6×10^{10} mL^{-1} (60 nm), 5.6×10^{9} mL^{-1} (100 nm), and 1.7×10^{9} mL^{-1} (150 nm)) were contained in a quartz cuvette (1 cm × 1cm × 5 cm) with an optical path length of 1 cm. The extinction spectra of these particles are shown in Figure 3-1. The sample solution was stirred magnetically during the laser experiments and was replaced every 500 shots.

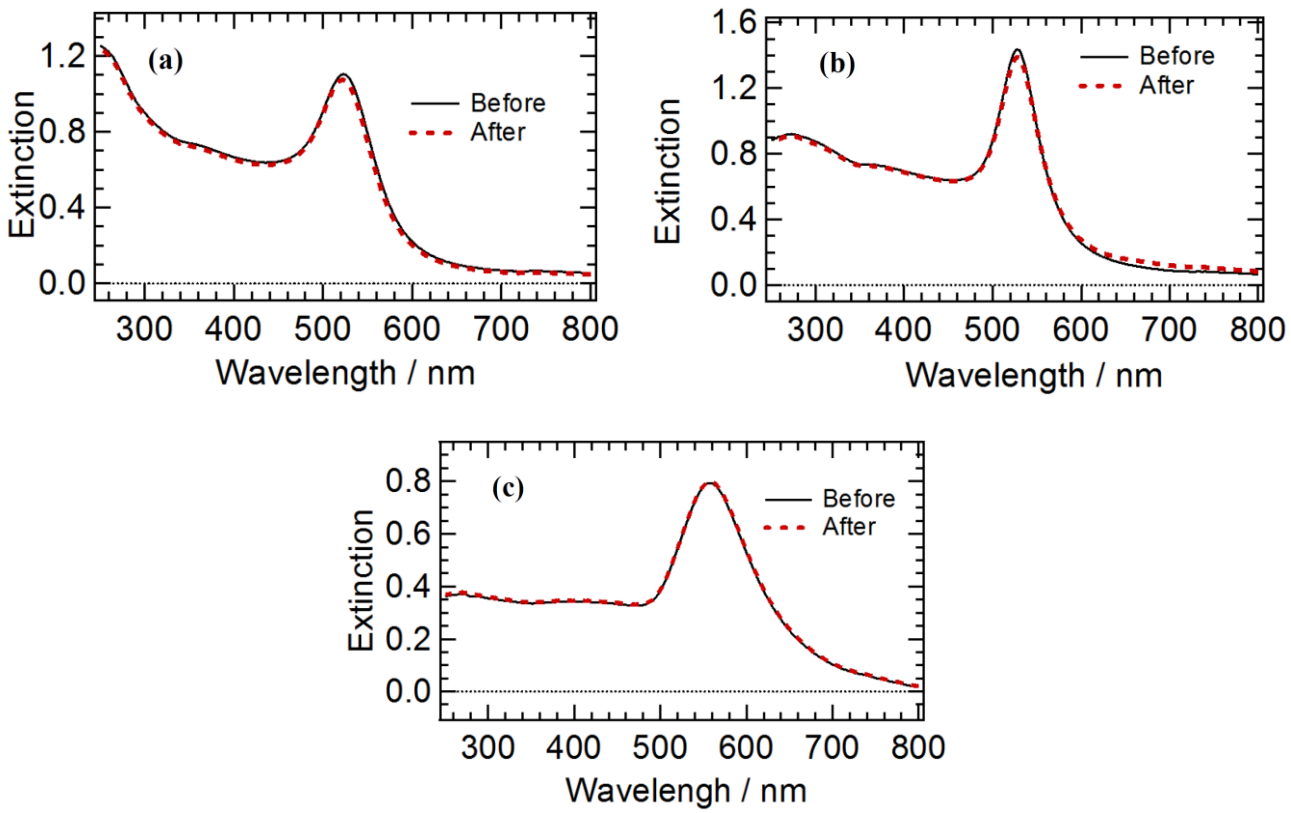

Figure 3-1. Extinction spectra of Au NPs in aqueous solution. 20-nm diameter for (a), 60-nm diameter for (b), and 100-nm diameter for (c), before and after 1000 shots (15 ps, 355 nm laser) at the threshold fluence of bubble formation.

Instrumentation. A picosecond pump−probe system with a custom-built mode-locked Nd^{3+}:YAG laser was used to measure the transient spectra at various time delays in the picosecond-to-nanosecond time regime.[22] Details of the experimental setup are shown in Scheme 3-1. Briefly, third-harmonic light (355 nm) with an fwhm of 15 ps was used as a pump pulse, and was focused using an f = 200 mm lens into a spot of diameter ca. 2 mm. Under these experimental conditions, the laser light formed an approximately parallel beam.

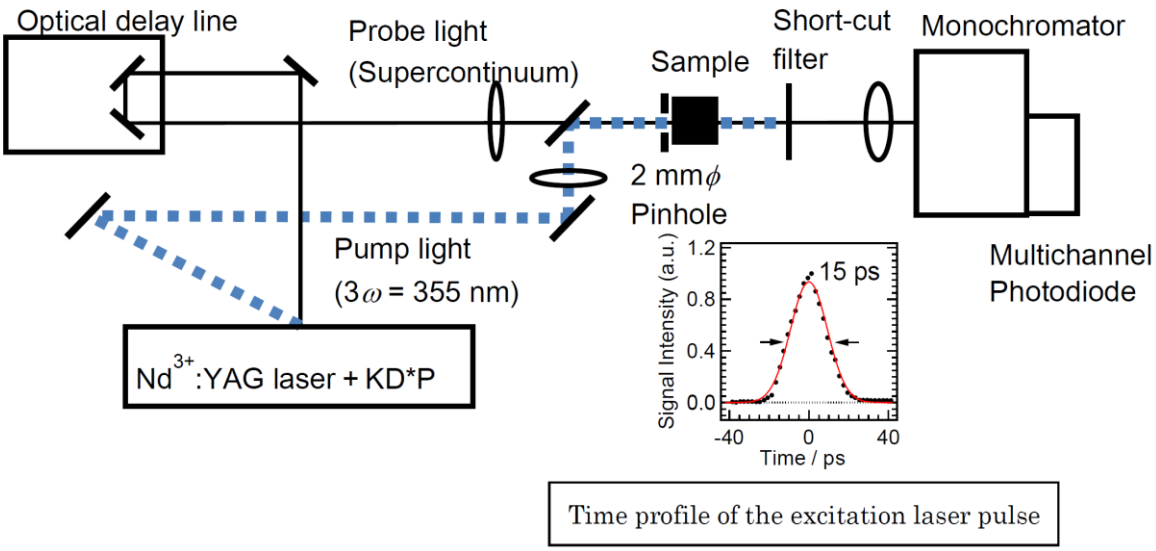

Scheme 3-1. Experimental configuration and the time profile of the excitation laser pulse.

The irradiation with a 355-nm laser pulse (power fluctuation <10%) excited the interband transition of the Au NPs. The interband transition was not sensitive to the particle temperature or refractive index of the medium, whereas the LSPR band in the visible region was strongly dependent on these factors as shown in Figure 3-2. Photoexcitation at the LSPR band induces the change of the absorption cross-section (C_{abs}) of the NPs during the nanosecond laser excitation.[17] However, under excitation at 355 nm with a 15 ps laser pulse, it could safely be assumed that the light absorption was free from any significant change in C_{abs} during the irradiation. Thus, the absorbed photon could be easily estimated.

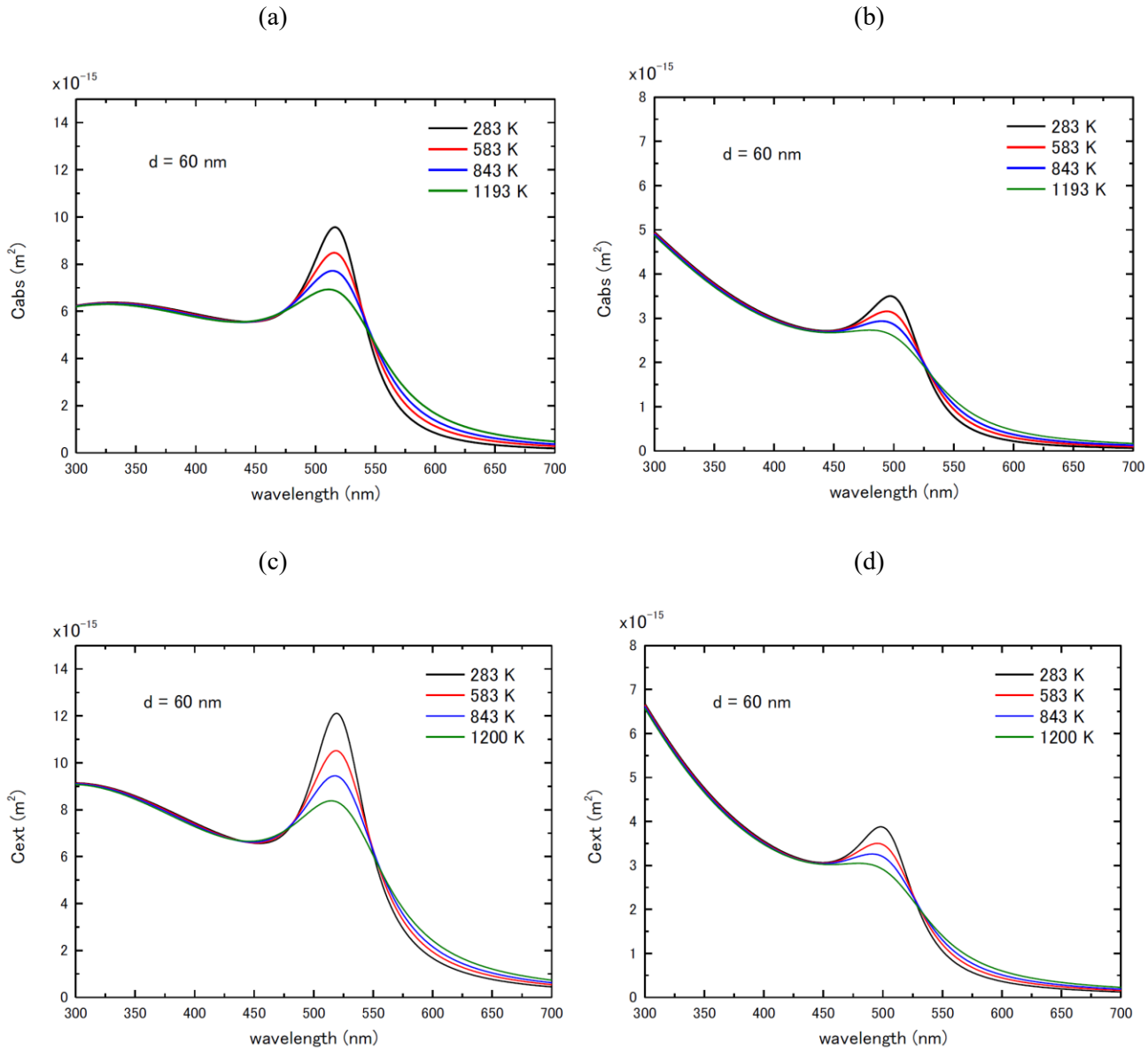

Figure 3-2. Temperature-dependent absorption cross section, C_{abs} as a function of wavelength calculated by applying Mie theory for the 60-nm diameter Au NP in water (n=1.33) (a) and in air (n=1.0) (b). The particle temperatures were shown in the figures. To calculate the temperature-dependent C_{ext}, the temperature–dependent dielectric functions of bulk gold experimentally determined by Otter (ref. 34) were employed. For comparison, extinction cross section (C_{ext}) spectra in water (c) and in air (d) were shown. Here, $C_{ext} = C_{abs} + C_{sca}$, with C_{sca}, scattering cross section.

The picosecond white light continuum generated by focusing a fundamental pulse into a 10 cm quartz cell containing a 3:1 D_2O and H_2O mixture was used as a probe light. Circularly polarized probe light was guided into the center of the 2-mm spot defining the pump area. Two multichannel photodetector sets (Hamamatsu, S4874) attached to the polychromator (Jarrell Ash, Monospec 27) were used to detect the probe light in the transient spectroscopy

The transient signals at a given time delay were obtained by calculating $\log_{10}\{I_0(\lambda)/I_p(\lambda)\}$. Here, $I_0(\lambda)$ represents the intensity of the probe light at wavelength λ without excitation, and $I_p(\lambda)$ is the probe light intensity with the excitation. In the transmittance-mode experiments on the Au NP colloidal solutions, contributions from both absorption and scattering influenced both the steady-state and the transient spectra (extinction = absorption + scattering). Hence, the transient signal obtained using the quantity $\log_{10}\{I_0(\lambda)/I_p(\lambda)\}$ corresponded to Δ-extinction. The amount of energy absorbed by a single Au NP can be expressed as $Q_{abs} = C_{abs}I$, where C_{abs} is the absorption cross-section of the Au NP at the laser wavelength, and I is the laser peak power density.[5]

The time origin was determined by measuring the rise curve of the transient absorbance for the reference sample, as a function of the relative time interval between the pump and probe pulses. The time origin of 0 ps was chosen by determining the time at which the transient absorbance of the $S_n \leftarrow S_1$ transition was one-half that obtained at a time delay that was sufficiently long to ensure that the transient absorbance had constant value. The repetition frequency of the laser light was approximately 0.5 Hz. The time resolution of the detection system was < 15 ps. The energy of the picosecond laser light was measured using a laser power meter (Gentec, ED-200). The precision of the measured fluence was ±0.1 mJ cm^{-2}. For measurements under a pressure of 60 MPa, the cuvette was placed in a hydrostatically pressurized container that enabled solution agitation.[23] Most of the data were accumulated over the course of four measurements. The errors for the transient extinction values were < ±10%, as estimated using the standard deviation of the signals before the time origin, and the spectral resolution was approximately 3 nm. The chirping of the probe white light continuum was corrected. All measurements were performed at 22 ± 1 °C

3-3. RESULTS AND DISCUSSION

Transient Extinction Spectra and Kinetics. Figure 3-3 shows the time-resolved transient extinction spectra for the aqueous 60-nm diameter Au NPs, excited with a picosecond 355-nm laser pulse. For the spectra measured at the low laser intensity of 1.1 mJ cm^{-2} (Figure 3-3a), a negative extinction signal around 525 nm and positive extinctions at 440−500 nm and 550−620 nm emerged almost within the response time of the detection system. Following electron excitation, hot electrons generated in the Au NPs are thermalized within 100 fs through electron-electron scattering, and the energy transfer from the electrons to the lattice occurs within approximately 2−5 ps.[24–27] Given that these processes occur with the pump pulse duration of 15 ps, temperature-induced damping or broadening of the LSPR band is most likely responsible for the temporal evolution of transient spectra in the early stages after the excitation. That is, the transient spectra with strong bleaching (negative signal) at the LSPR peak position are accompanied with the appearance of positive extinctions on both sides of the LSPR band.[24–26,28] With an increase in the time delay time after the excitation, the bleaching intensity and that of the positive bands gradually decreased in the subnanosecond to nanosecond time region. This time evolution was attributed to cooling of the lattice system.[24–26,29]

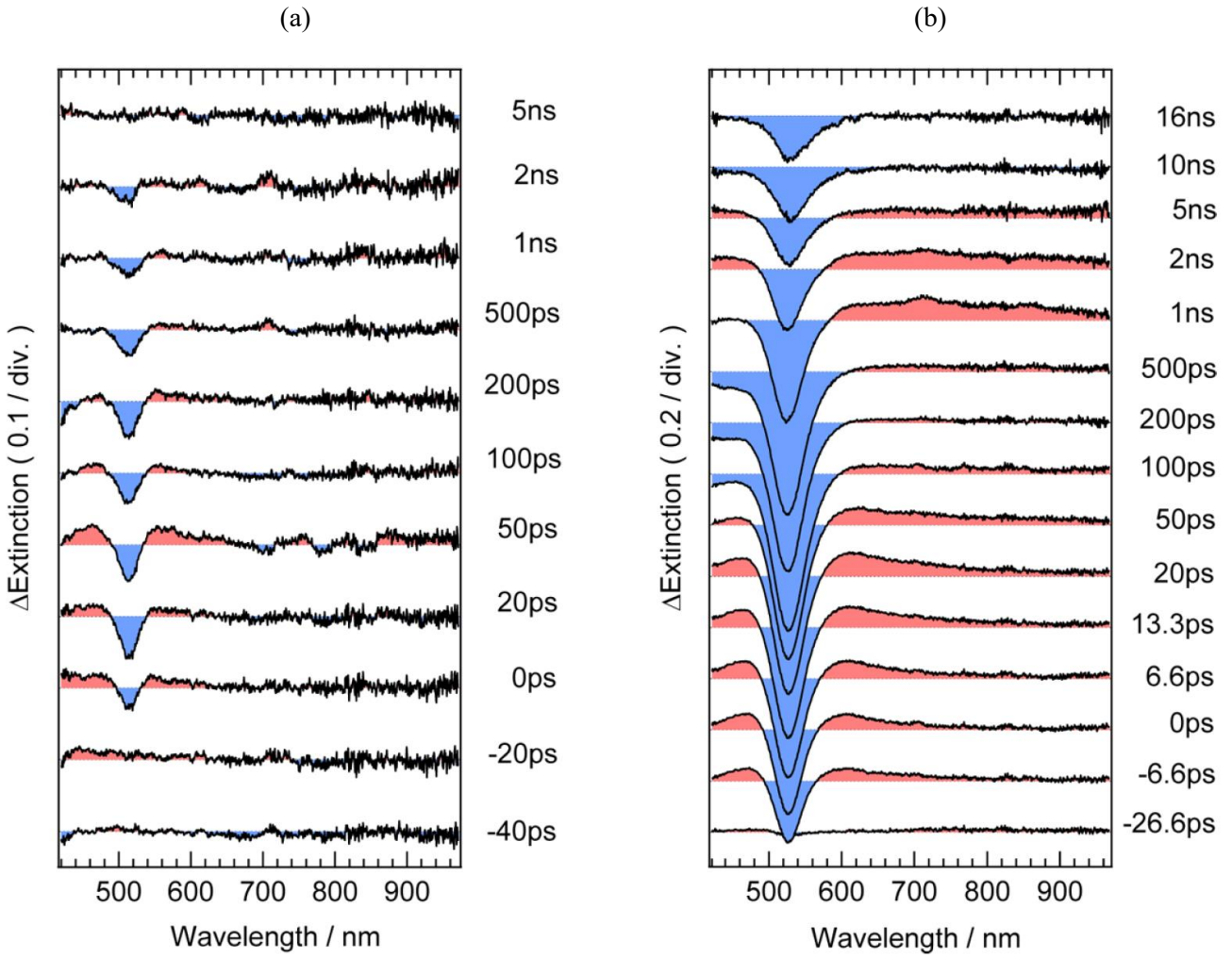

Figure 3-3. Transient extinction spectra of aqueous colloidal Au NPs with a 60-nm diameter at various delays from the bottom to the top at the fluence of 1.1 mJ cm^{-2}, from −40 ps to 5 ns (a), and 5.2 mJ cm^{-2}, from −26.6 ps to 16 ns (b). The excitation was provided by a 15 ps (fwhm) laser pulse at a wavelength of 355 nm for an Au NP solution. The blue-shaded areas represent bleaching (negative extinction), and the red-shaded areas represent positive extinction. Time delays are given on the right of each graph. The spectra were shifted with time delays from lower to upper by the extinction value of 0.1 in (a) and 0.2 in (b).

After several nanoseconds following the excitation, no signal was observed, indicating that NP photodegradation was negligible under the fluence of 1.1 mJ cm^{-2}. The observed transient spectral band shapes and their temporal evolution agreed well with previous observations.[24,26,28] When the excitation intensity was increased to 5.2 mJ cm^{-2}, transient spectral dynamics, distinct to those observed at 1.1 mJ cm^{-2}, were observed in the time delay range from 100 ps to 5 ns.

To obtain a detailed description of the time evolution, we plotted the time profiles of the transient extinction signals for Au NPs under radiant exposure of 5.2 mJ cm^{-2}. The time profile monitored at 450 nm (see Figure 3-4a) showed the rapid appearance of the positive transient extinction within the response time of the apparatus, followed by a decay to a negative value within a few 100 ps. For time delays at and after ca. 300 ps following the excitation, the increase in the transient extinction signal was observed, reaching a maximum value at about 2 ns, and then decreased until 16 ns; for times longer than this, a slightly negative constant value was observed. This complicated behavior could not be explained by simple particle heating−cooling dynamics observed at the low fluence of 1.1 mJ cm^{-2}.

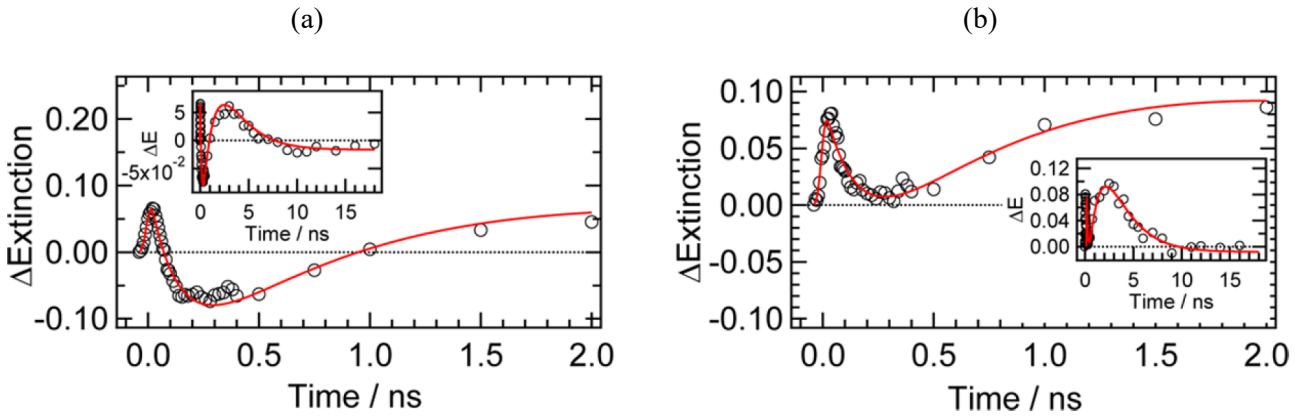

Figure 3-4. Time evolution of transient extinction of colloidal solution of Au NPs with a 60-nm diameter, excited with a picosecond 355-nm laser pulse at a fluence of 5.2 mJ cm^{-2}. Monitoring wavelengths for (a) was 450 nm and that foe (b) was 630 nm. The outer frames represent short time scales of up to 2 ns, whereas the insets represent longer time scales of up to 18 ns. The red lines were curves calculated with a triple-exponential function with time constants of 150 ± 12 ps, 1. 2 ± 0.26 ns, and 2.3 ± 0.58 ns.

We also plotted the time profile at 630 nm in Figure 3-4b. As was shown in Figure 3-1b, the Au Np with a 60-nm diameter has no strong extinction in the steady-state spectrum. A time profile of transient signal at 630 nm was similar to that observed at 430 nm (figure 3-4a). The positive transient extinction appearing immediately after the excitation was followed by a decay in sub-ns time region. At and after ca 300 ps following the excitation, the transient extinction signal again increases, reaching a maximum value at ca. 2 ns, followed by the decrease in longer time region. The solid lines in Figure 3-4a and b are curves analyzed using a triple exponential function; the time constants for the time profiles are given in the figure caption. Almost the same time constants were obtained for the two time profiles, indicating that the dynamics under the strong excitation condition is quite different from that observed under the low excitation conditions. Note that, at 630 nm, the transient extinction recovers to the baseline at and after 12 ns following the excitation.

To more precisely elucidate the origin of these additional dynamics, we measured the fluence dependence in detail. Figure 3-5 shows time profiles monitored at 450 nm. Under the excitation with the fluence of 1.1 mJ cm^{-2}, no strong signal was observed. At the fluence of 5.2 mJ cm^{-2}, the positive signal

appearing immediately after the excitation decreases in the time region < 150 ps and the constant negative signal remains in the time region > 200 ps. On the other hand, at the fluence of 55 mJ cm^{-2}, the increase of the transient signal was observed at and after ca. 150 ps following the excitation. Because the lattice temperature of the NPs increases with increasing fluence, this rise strongly suggests that the process is closely related to heating of the medium leading to vapor bubble formation. Indeed, bubble formation can rationally account for the spectral differences between Figure 3-3a and b. In Figure 3-3b, the positive transient extinction appearing in the early stages of the excitation decreases to a negative value within a few 100 ps. This decrease can be induced by the bubble formation because the refractive index of the medium surrounding the NPs is reduced by the bubble formation, leading to a decrease in the extinction. Furthermore, bubble growth can induce the increase in the positive signal as due to the increase in the scattering component and the disappearance of the bubble results in the decrease of the positive signal as observed in 10-20 ns time region (Figures 3-3b and 3-4).

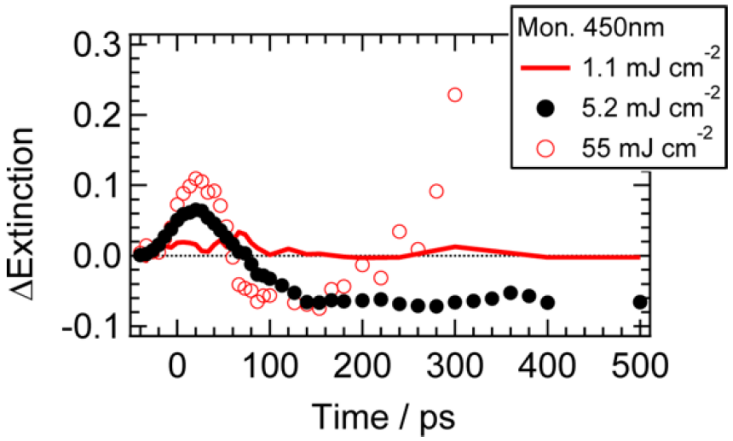

Figure 3-5. Fluence dependence of time profiles for transient extinction signals of colloidal solution of Au NPs with a 60-nm diameter in the initial 500 ps after the excitation with a picosecond 355-nm laser excitation and monitored at 450 nm.

To confirm the contribution of the bubble formation, we examined the transient dynamics under the high pressure of 60 MPa, which is much higher than the critical pressure of 22.1 MPa for water.[30,31] Figure 3-6a shows the transient extinction spectra of aqueous Au NPs with a diameter of 60 nm, excited with a 355-nm laser pulse with a fluence of 4.9 mJ cm^{-2}. Temporal evolution of the spectra at 60 MPa in sub-ns to several ns time region is almost the same with those observed at the normal pressure (0.1 MPa) in Figure 3-3a; a negative extinction signal around 525 nm, and positive signals at 440− 500 nm and 550−620 nm, appearing are followed by the gradual disappearance of bleaching and the positive bands. This time evolution was attributed to the cooling of the lattice system. However, it should be noted that the rise and decay signals observed at and after several hundreds of picoseconds in Figure 3-3b were not detected under the high pressure. The lack of these additional dynamics was also confirmed for the time evolution of the same system exposed to a fluence of 9.9 mJ cm^{-2} (Figure 3-6b).

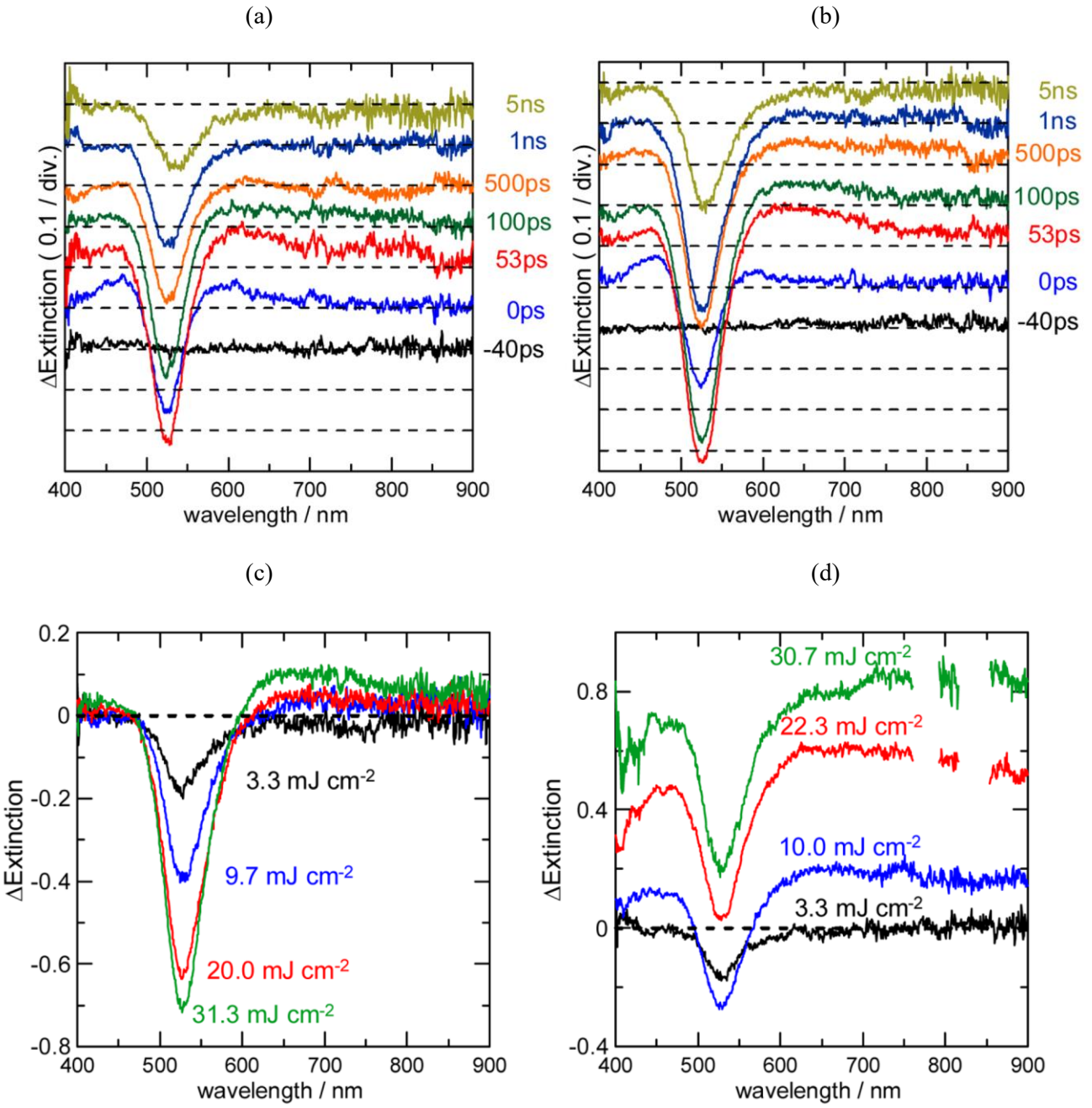

Figure 3-6. Transient extinction spectra of aqueous colloidal Au NPs with a 60-nm diameter under the pressure of 60 MPa. (a) time evolution at a fluence of 4.9 mJ cm^{-2}, (b) time evolution at a fluence of 9.9 mJ cm^{-2}, and (c) fluence-dependent spectra at 2 ns after the excitation. For comparison with (c), fluence-dependent spectra at a time delay of 2 ns are shown for atmospheric pressure (0.1 MPa) in (d). The time delays were given for (a) and (b); and fluences were given for (c) and (d). In (a) and (b), the spectra were shifted with time delays from lower to upper by the extinction value of 0.1.

To more precisely elucidate the effects of the external pressure, the fluence dependence of the transient extinction spectra was measured for 60 MPa (Figure 3-6c). Compared to the spectra at 0.1 MP in Figure 3-6d, one can find the spectral shape is less dependent on the fluence; the increase in the positive background in the entire wavelength window (400−900 nm) was significantly suppressed under the high pressure, although the positive signal in the wavelength region of >600 nm increased with a decrease in extinction (or increases in bleaching) at the LSPR peak position. These results support that the positive signal, which resembles a floating baseline, is due to the scattering signal due to the bubble formation. NPs.

It should be noted that, even at a fluence of 5.2 mJ cm^{-2}, the bleaching signal at the LSPR peak position did not recover to the baseline in the time window of the measurement (0-16 ns). To elucidate this long-living bleaching signal, we measured the time profile of the signal in longer time region using a CW laser beam as a probe light and a photodiode (rise time <1 ns) as a detector. As shown in Figure 3-7a, this negative signal decreases in the initial 10 ns after the excitation and is followed by the constant signal remaining in the time region of 80 ns, suggesting the permanent bleaching by the photodegradation of Au NPs. So as to obtain the detailed information, TEM images were measured. Figure 3-7b shows that a small number of spherical particles were observed after the laser irradiation among faceted Au NPs. These images indicate that the morphological change of Au NPs is the origin of the permanent bleaching. Interestingly, permanent bleaching was not observed in the case that the particles with spherical shape were irradiated with a picosecond laser at the similar fluence (Figure 3-7c).

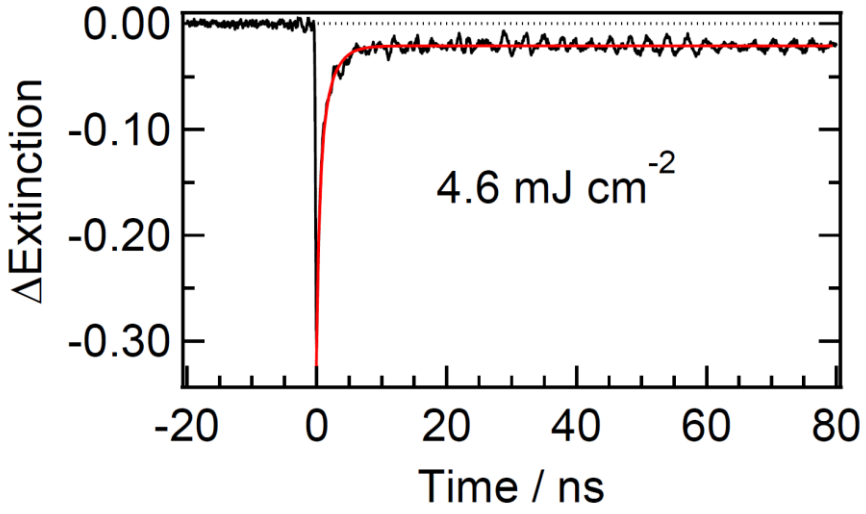

Figure 3-7. (a) Extinction change observed at 532 nm when excited by a 355 nm, 15 ps laser with a fluence of 4.6 mJ cm^{-2}, (probe light: CW laser (PHOTOP, DPGL-2050F), detector: photodiode (Thorlabs, DET10A/M, rise time < 1 ns)) at a time scale longer than that of the pump-probe measurement, showing the indication of permanent bleach. The extinction signals were 19-times accumulated. The permanent bleach was not observed at 4.0 mJ cm^{-2}.

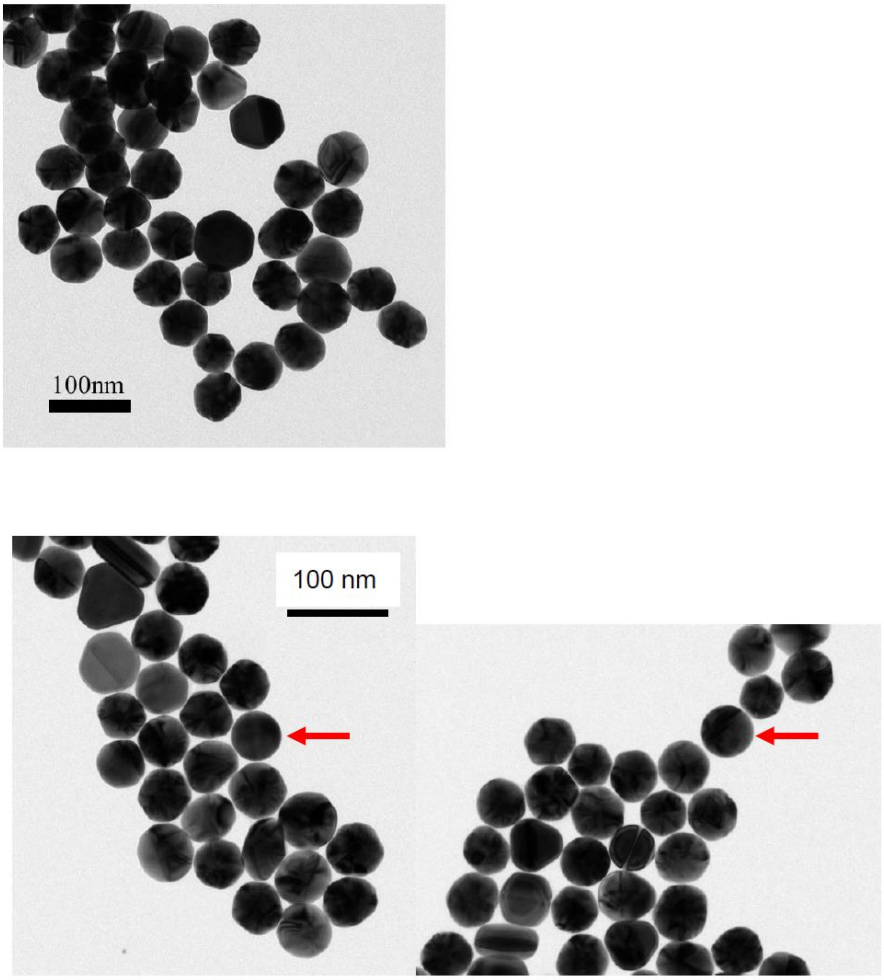

Figure 3-7. (b) TEM micrographs of 60-nm diameter Au NPs before (upper panel) and after (lower panel) irradiation at 4.6 mJ cm^{-2} for 500 shots by a 355 nm, 15 ps laser. The red arrow indicates a spherical particle generated by the laser irradiation among the original faceted particles.

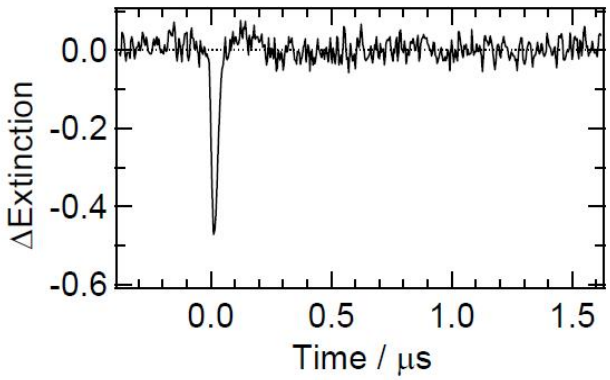

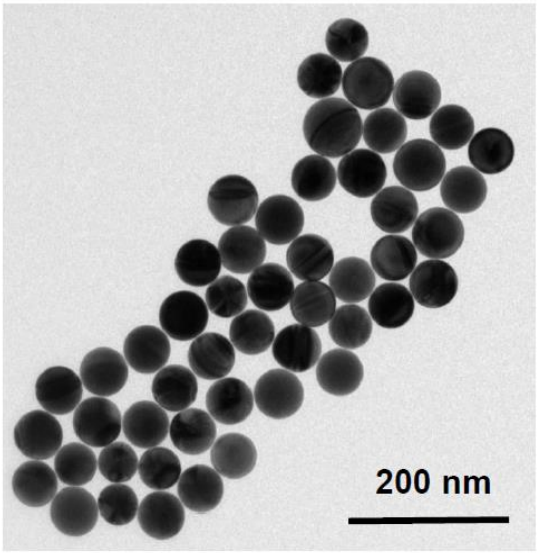

Figure 3-7. (c) Extinction time curve (upper panel) observed at 532 nm for 60 nm diameter reshaped Au NPs (lower panel: TEM image) when excited by a 355 nm, 15 ps laser with a fluence of 5.0 mJ cm^{-2}.

Threshold of the Bubble Formation. Figure 3-8a shows the fluence dependence of the Δ-extinction of aqueous Au NPs with various diameters, measured at 2 ns after the pulsed excitation shown in Figure 3-9. Fluence dependence of Δ-extinction in Figure 3-8a clearly shows nonlinear behaviors with a threshold. For example, for the NPs with a diameter of 100 nm, Δ-extinction was almost zero in the range 0−8 mJ cm^{-2}, whereas it suddenly increased above ca. 8.5 mJ cm^{-2}.We attributed the threshold fluence for bubble formation to this critical fluence, because the extinction signal above this fluence could be attributed to the scattering as shown in Figure 3-9 where the positive signal appears in the entire wavelength region. The threshold fluence for the bubble formation thus estimated is plotted as a function of Au NP diameter in Figure 3-8b. Because the Au NP commercially available has a distribution of diameters to some extent, we employed 4 systems with different averaged diameters. The diameter dependence shows that the threshold does not simply increase and the small dip exists around 60-nm diameter.

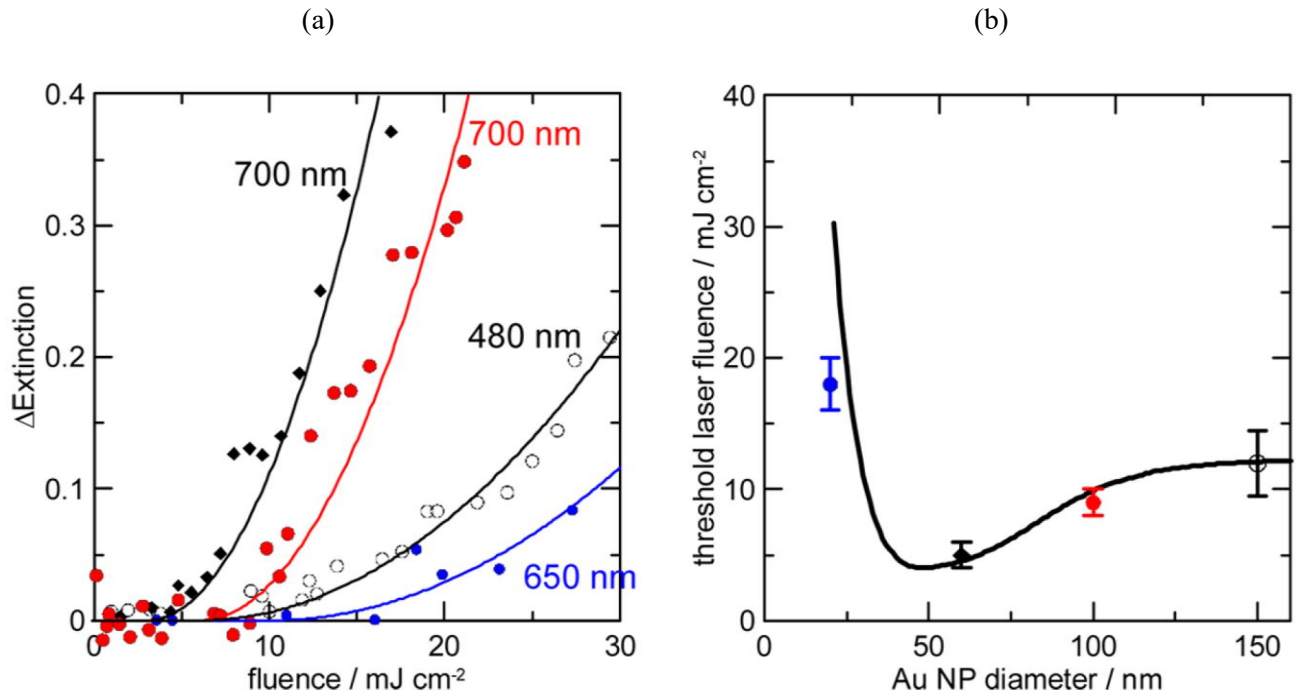

Figure 3-8. (a) Fluence dependence of the transient extinctions of Au NPs in aqueous solution measured at 2 ns following excitations with a 15-ps, 355-nm laser pulse: monitored for Au NPs with the 20-nm (blue ●), 60-nm (◆), 100-nm (red ●), and 150-nm (○) diameter NPs. Monitoring wavelength: 650 nm for 20 nm Au; 700 nm for 60 and 100 nm Au; 480 nm for 150 nm Au. Solid lines are eye guides. Errors for the extinction values: ±0.008 estimated by the standard deviation. (b) Experimental bubble formation threshold as a function of Au NP diameter in aqueous colloidal solution excited at 355 nm with a laser pulse of 15 ps and a simulated curve. The simulation was performed by calculating the medium temperature at the NP−water interface. The temperature profiles at the time delay of 400 ps were used for the calculation of the average temperature.

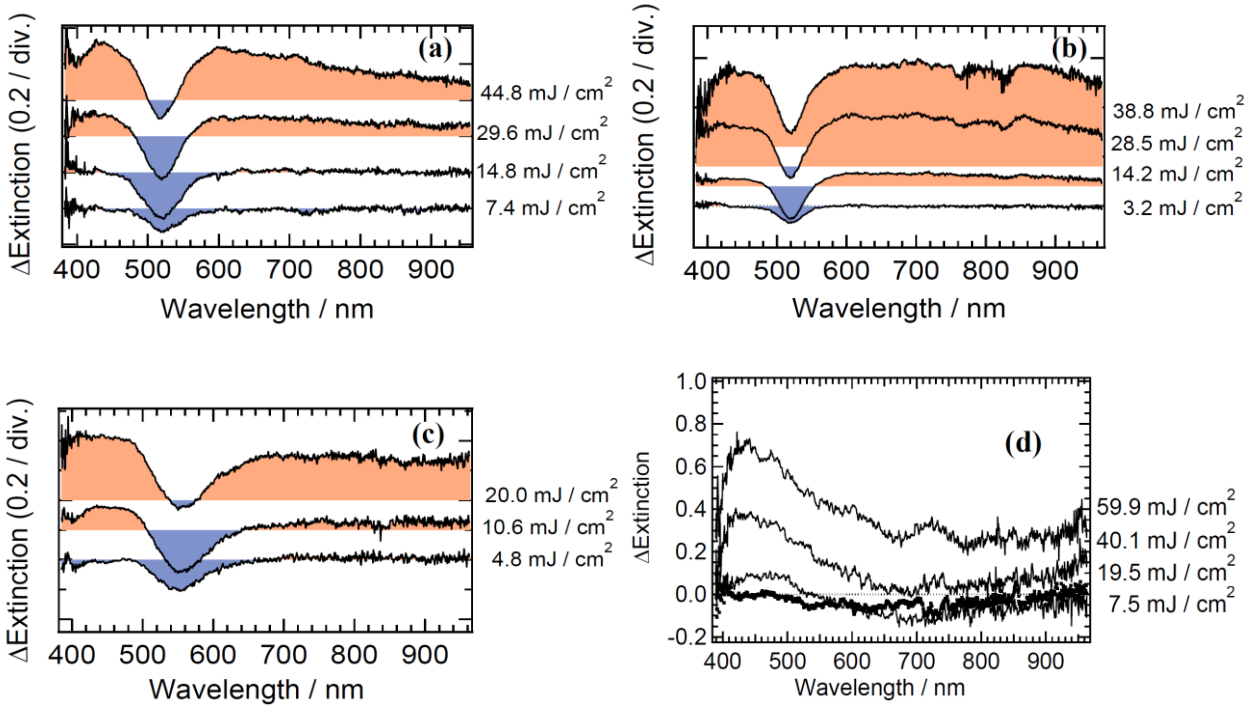

Figure 3-9. Transient extinction spectra of Au NPs with different sizes in aqueous solution monitored at 2 ns following the excitation; (a) for 20 nm, (b) for 60nm, (c) for 100 nm, and (d) for 150 nm in diameter. The fluence of the excitation laser pulse is shown in each of the figures.

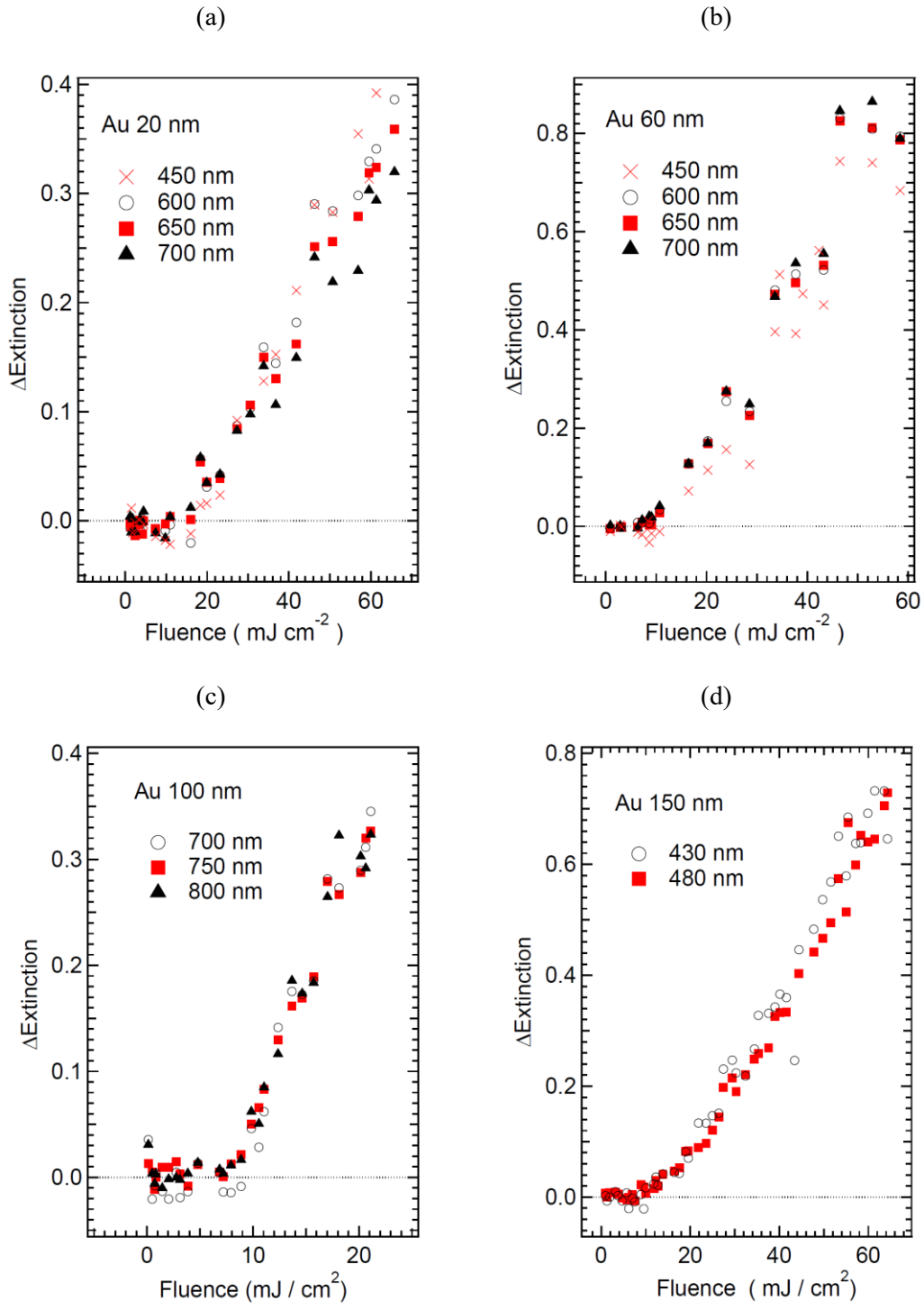

Figure 3-10. Fluence-dependent extinction changes at different wavelengths for aqueous colloidal Au NPs (20-, 60-, 100-, and 150-nm diameters) measured at the time delay of 2 ns following the excitation with a 15 ps, 355-nm laser pulse.

On the relation between the diameter and the threshold of the bubble formation, Plech and coworkers reported the experimental results for aqueous colloidal Au NPs with diameters of 15−100 nm by means of the pulsed excitation with a 100-fs laser pulse at 400 nm and the probe X-ray with ca. 100 ps pulse width. They demonstrated that bubble nucleation occurred at a lower fluence for larger particles. In addition, they pointed out the saturation of the threshold with an increase in the size of the particle. They interpreted these results in such a manner that, because of the difference in the surface-to-volume ratio, the water phase reached higher temperatures for larger particles even at the same fluence. Their experimental results on the relation between the threshold and the size if NPs were well reproduced by the curve calculated under the assumption of an interfacial water temperature slightly lower (85%) than that of the critical temperature of water, 647 K.[32]

Lapotko and coworkers also reported the relation between the threshold and the size of Au MPs. They measured the optical transmittance signal, which become small by the scattering of the bubble, for the single Au NP after the excitation with a 532-nm laser pulse (0.5 or 10 ns).[16−18] They experimentally determined the threshold of the bubble generation for Au NPs with 30, 100, and 250-nm diameters. They confirmed that the threshold fluence decreased with an increase in the size of Au NPs. Their method, measurement of the single MP, demonstrated that the threshold value was, at least, 1 order of magnitude higher than those determined using ensemble measurements.

As stated above, these previous results demonstrated that the threshold of the bubble generation decreases with an increase in the size of the Au NPs, although the excitation wavelength of these studies is different from the present one (355 nm). In the present result as was shown in Figure 3-8b, the minimum threshold was observed at the diameter of 60 nm. To elucidate the difference observed in the present irradiation condition, we undertook the numerical simulation for the relation between the diameter of Au NPs and the threshold. In this simulation, we assumed that boiling of the medium could start in the condition where a certain fixed volume of water surrounding the various sizes of Au NP, not only the thin layer of water, reaches an average temperature of 550 K. The curve thus calculated is shown in Figure 3-8b. Although the best fitting curve was obtained for the water volume of 6.4×10^{-24} m^3 (a volume corresponding to a shell with

an inner diameter of 15 nm and an outer diameter of 25 nm), we could not reproduce the experimental results (Figure 3-11). These results suggest that the average temperature of the interfacial water volume was a better measure of the bubble formation threshold, as compared to the temperature of the interfacial water layer. The non-monotonic diameter-dependent threshold curve (Figure 3-8b) is ascribed to the diameter-dependent medium heating efficiency, represented by $(C_{abs}/V)/G_c$ (G_c, critical thermal interface conductance; C_{abs}, absorption cross section; V, particle volume) that showed a maximum at 40−60 nm (Figure 3-12).[5] This quantity is negatively and nonlinearly correlated with the bubble formation threshold and qualitatively explains the curvature in Figure 3-8b.

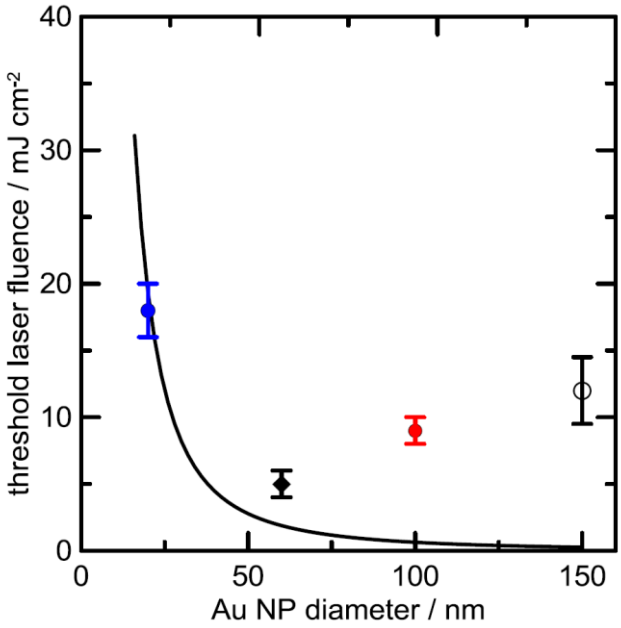

Figure 3-11. Simulated threshold laser fuence *vs*. Au NP diameter, calculated assuming the temperature of a water layer 2 nm from the NP interface reaches 550 K, after 400 ps of the laser excitation (355 nm, 15 ps).

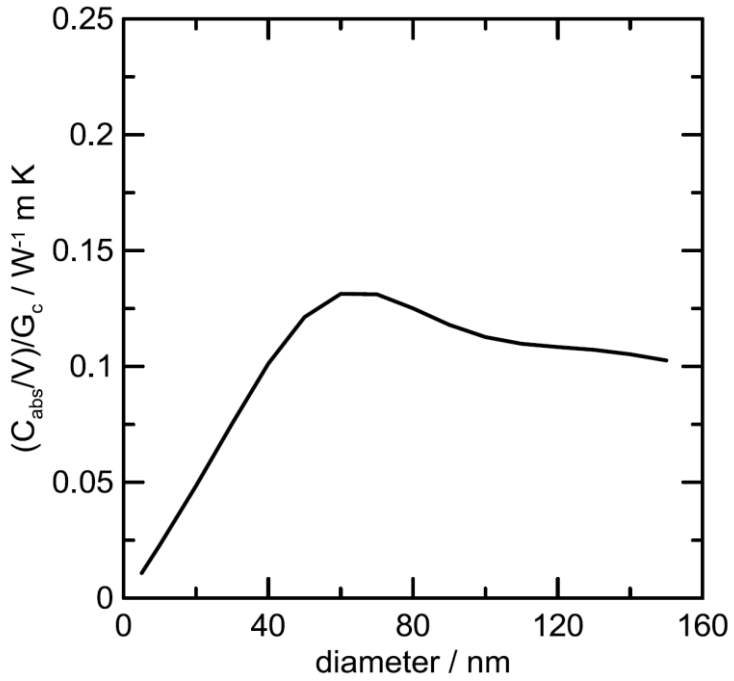

Figure 3-12. Diameter-dependence of a quantity, $(C_{abs}/V) / G_c$, representing the medium heating efficiency. G_c, C_{abs}, and V are respectively critical thermal interface conductance, absorption cross section, and particle volume.

Recently, Cavicchi and coworkers reported the morphological change of Au NPs on the nanosecond pulsed laser-induced photo thermal size reduction of 10−100 nm excited at 532 nm supported our result in Figure 3-8b.[33] As particle diameter increased from 10 to 60 nm, the threshold fluence decreased, whereas at 100 nm, the threshold for observed particle damage appeared to increase, resulting in a minimum at 60 nm. They assumed that nanobubble generation occurred at a fluence near the threshold for particle damage.

Our measurements revealed that the threshold for bubble generation (5 mJ cm^{-2}) was similar to the threshold for particle deformation after the excitation of 60-nm diameter Au NPs using the 355-nm laser pulse with 15-ps fwhm. Previously, Inasawa group reported that the threshold value for the ablative size reduction of Au NPs with an average diameter of 36 nm under the application of a 355-nm laser pulse with 15-ps fwhm was 17 mJ cm^{-2},[34] which is at least 3 times larger than the threshold for bubble formation obtained in the present work. Pre-melting or surface melting is the likely cause of the deformation.[5,34] Accordingly, we conclude that the particle temperature approached, but did not reach, the melting point (mp) of Au (1337 K) when bubble initiation took place.

Simulation for the extinction spectrum.

In the present section, we perform spectral simulation to evaluate the size of nanobubbles. Figure 3-13a shows the schematic representation of the simulation for the bubble formation. Here, two concentric spheres (Au core and bubble shell) were submerged in a water medium (refractive index of 1.33 at ambient temperature). As applied by Plech group,[19] this model was used to simulate the extinction spectra of Au NPs based on the Mie theory.[2,35] Figure 3-13b shows the simulated extinction cross-section spectra, C_{ext}, for a single Au NP (d = 60 nm) at four particle temperatures (T_{NP}) from 283 to 1193 K in aqueous solution. It should be noted that a NP at T_{NP} = 1193 K is surrounded by bubbles of various diameters. We selected these four temperatures because the experimental dielectric functions for bulk gold were reported.[36] Cross-section C_{ext} [m^2] represents the light extinction for a single particle, and its correlation with the extinction (abbreviated as "Ext") for a colloidal solution can be expressed as

$$\text{extinction} = \log_{10}\left(\frac{I_0}{I}\right) = \frac{C_{ext}Nl}{2.303} \quad (3\text{-}1)$$

where I_0 denotes the incident probe light intensity, I is the transmitted probe light intensity, N [m^{-3}] is the particle number concentration, and l [m] is the optical path length. Note that C_{ext} is a function of T_{NP}, and is also related to the temperature of the medium; specifically, it is related to the distance-dependent temperature profile. The Mie calculation was performed by taking into account both the particle temperature and the temperature-induced refractive index gradient of the medium (based on a temperature profile similar to those given in Figure 3-14).[35]

(a) (b)

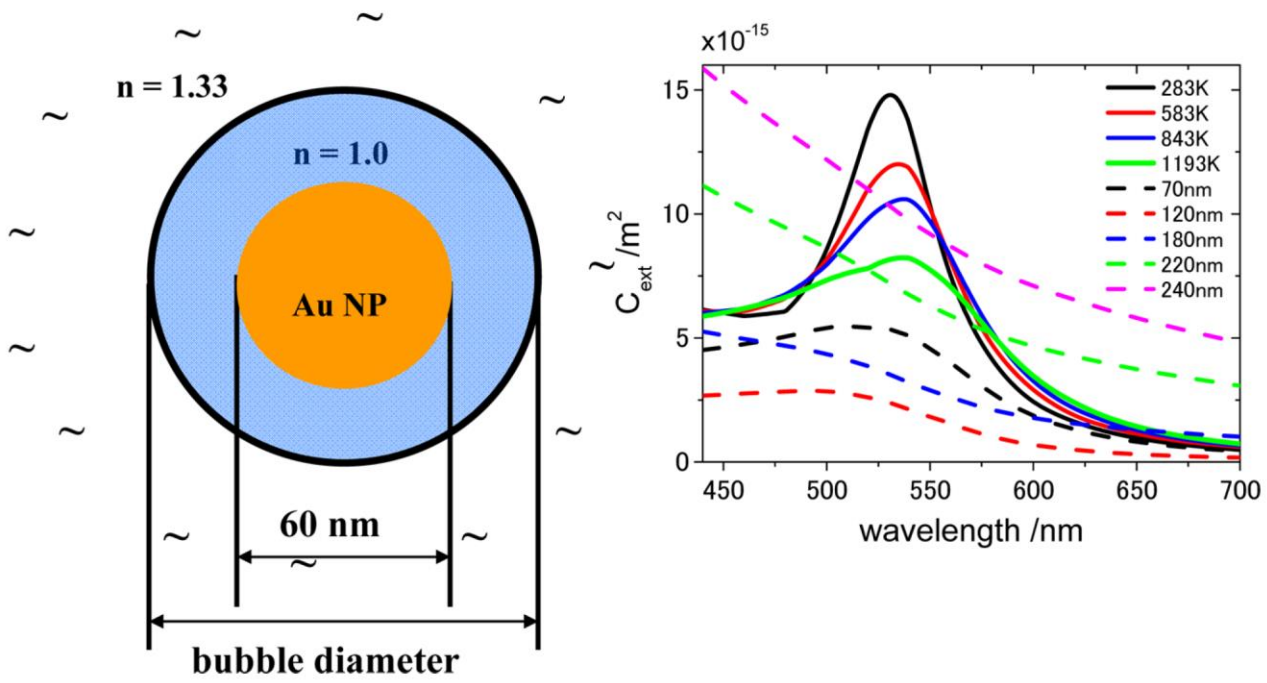

Figure 3-13. (a) A model of Au NP/bubble/water structure in which a spherical Au NP, surrounded by a concentric spherical bubble (refractive index: 1.0), is submerged in water (refractive index: 1.33). (b) Simulated extinction cross-section (C_{ext}) spectra for the Au NP/bubble/water structure. Solid lines: The extinction cross-section spectra of a 60 nm diameter Au NP at various particle temperatures (283, 583, 843, and 1193 K) in water (radial temperature distributions such as those given in Figure 3-14, were taken into consideration for the spectral calculations). Broken lines: The extinction cross-section spectra of a 60 nm diameter Au NP and vapor bubble of various diameters listed in the legend (T_{NP}, 1193 K and T_m, room temperature).

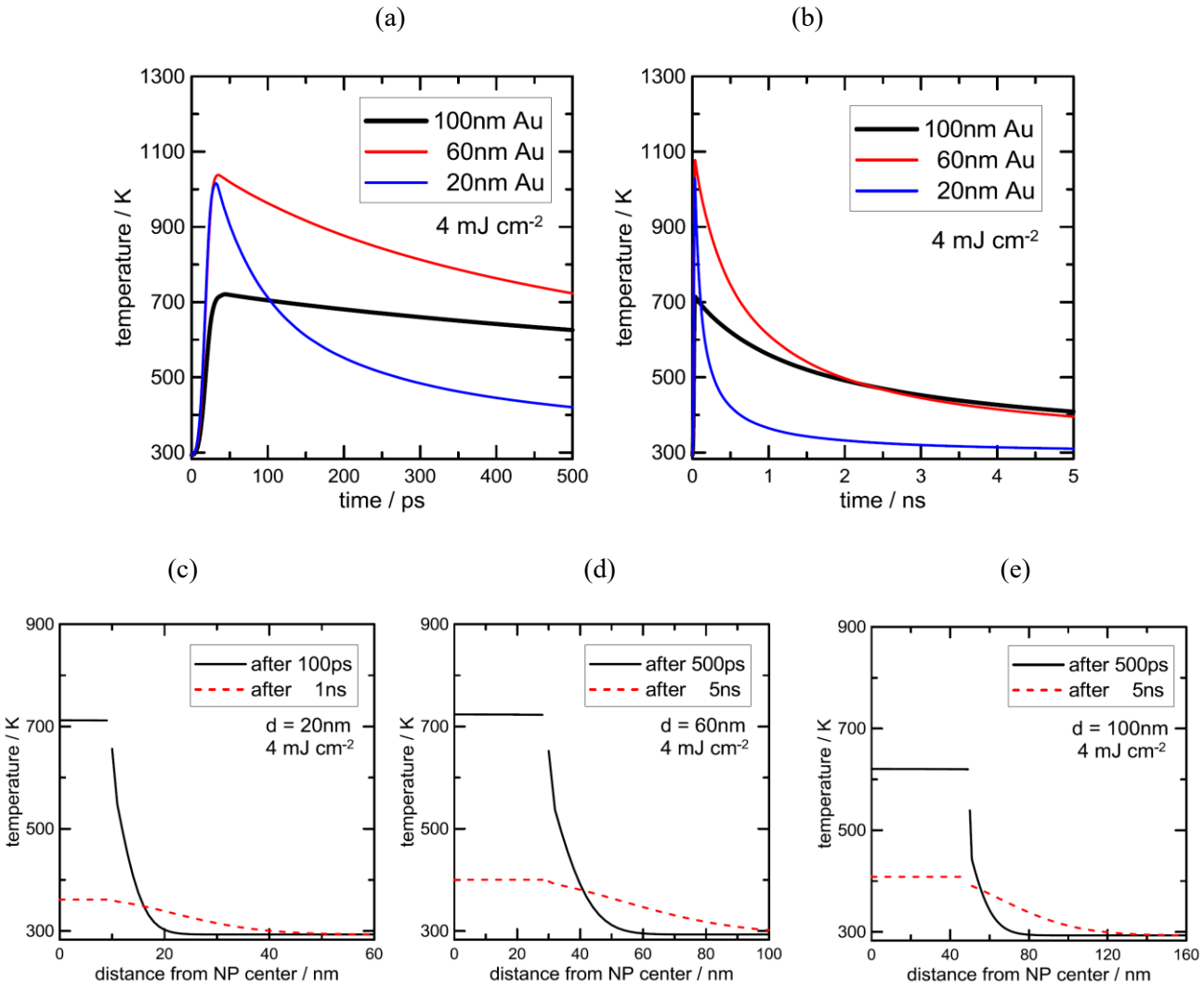

Figure 3-14. (a), (b) Time profiles of the temperature of Au NPs (20-nm, 60-nm, and 100-nm diameters) in water (n = 1.33) after the excitation with a 355-nm pulse (15-ps FWHM). Laser intensity is given in the figure. (c) - (e) Spatial profiles of the temperature of Au NPs (20-nm, 60-nm, and 100-nm diameters) in water (n = 1.33). The origin of the distance corresponds to the center of the Au NP. Time dependence of the temperature shows that the particle cooling is strongly dependent on the particle diameter: the cooling rate is much greater for smaller particle diameter. Temperature profiles suggest that medium cooling is remarkable for Au NP with 20-nm diameter. Calculation was performed using COMSOL Multiphysicsv.4.3a (http://www.comsol.com).

These results suggested that the extinction spectrum gradually broadened with increasing NP temperature. The damping of the LSPR band intensity with increasing temperature has been revealed experimentally.[37,38] With the formation of the vapor bubbles surrounding the particles, further spectral broadening and a much greater intensity reduction occurred for bubble diameters <120 nm. This is because the refractive index of the medium directly surrounding the particle is reduced appreciably. However, the contribution of the light scattering increases in the case where the bubbles grow to diameters larger than 120 nm. Accordingly, the extinction spectrum was dominated by the scattering from the bubble and the contribution of the Au NP was obscured, except in the valley at the LSPR peak position.

To more precisely elucidate the contributions to transient spectra experimentally obtained (Figure 3-3), we constructed the difference extinction cross-section spectra, ΔC_{ext}. Three conditions are illustrated schematically in Figure 3-15 (on the left). We first considered changes only in particle temperature:

$$\Delta \mathrm{C_{ext}} = \mathrm{C_{ext}}(T_{NP}) - \mathrm{C_{ext}}(\mathrm{RT}) \qquad (3\text{-}2)$$

We then included changes in temperature of the medium, in addition to increases in particle temperature in the absence of a bubble:

$$\Delta \mathrm{C_{ext}} = \mathrm{C_{ext}}(T_{NP}, T_m) - \mathrm{C_{ext}}(\mathrm{RT}) \qquad (3\text{-}3)$$

and, finally, in the presence of a bubble:

$$\Delta \mathrm{C_{ext}} = \mathrm{C_{ext}}(T_{NP}, \mathrm{bubble}) - \mathrm{C_{ext}}(\mathrm{RT}) \qquad (3\text{-}4)$$

where $C_{ext}(T_{NP})$ is C_{ext} at particle temperature T_{NP}, $C_{ext}(T_{NP}, T_m)$ is C_{ext} at particle temperature T_{NP} with T_m being the temperature of the medium (water) at the particle surface, $C_{ext}(T_{NP}, bubble)$ is C_{ext} at particle temperature T_{NP} in the water vapor bubble, and $C_{ext}(RT)$ is C_{ext} at room temperature in water in the absence of a bubble.

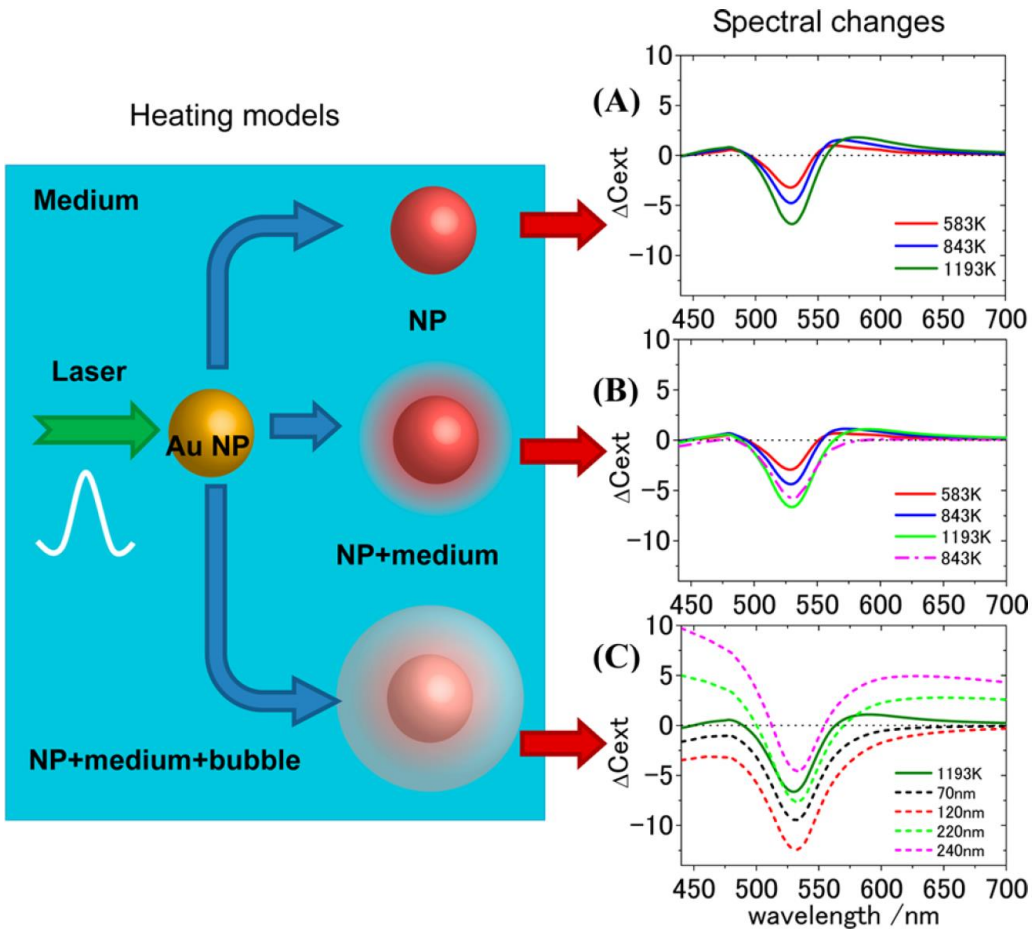

Figure 3-15. Schematic representation of processes induced by the temperature increase of the particle (left side) and the corresponding spectral changes of the extinction cross section of Au NPs with 60-nm diameter obtained by simulation (right side) in three cases: (A) only the particle heating (spectra based on eq 3-2) was take into account, (B) particle heating accompanied with the medium heating without bubble formation were taken into account (spectra based on eq 3-3), and (C) particle heating accompanied with the bubble formation was taken into account (spectra based on eq 3-4)Temperatures of the particle used for the simulation are given in each of figures. Broken lines represent the transient extinction spectra for various bubble diameters given in the figure. The unit of ΔC_{ext} is 10^{-16} m^2. For the calculation of spectra in panel B, the temperature distributions in the surrounding water at various delays of laser irradiation were considered (29.5 ps for 583 K, 35 ps for 843 K, 54 ps for 1193 K, 237 ps for 843 K). Typical medium temperature distributions are given in Figure 3-14.

Figure 3-15 (on the right) shows transient extinction spectra (ΔC_{ext} versus wavelength) of 60-nm diameter Au NP heated by laser irradiation in water, simulated by the three models described above. The upper-right panel A shows the results when only particle temperature changes were considered (eq 3-2); the middle panel B shows results when temperature changes in the surrounding water were also considered (eq 3-3); and the third panel C shows the spectral changes assuming the bubble formation (eq 3-4) with T_{NP} = 1193 K and T_m = 574 K. As mentioned in the section on the bubble formation threshold, the value of T_{NP} at the threshold fluence for the bubble formation was expected to be close to the melting point of gold (1337 K). Our temperature calculation yielded a value of T_{NP} = 1200 K at the bubble formation threshold of 5 mJ cm^{-2}. Thus, we used T_{NP} = 1193 K for the calculation of C_{ext} (T_{NP}, bubble). Note that temperatures estimated by our computational method showed good agreement with those obtained experimentally for steady-state heating of a single Au NP.[39]

Spectra calculated for the Au NP surrounded by vapor bubbles with various diameters (refractive index: 1.0) in water are shown in Fig.3-15c. In the absence of bubble formation, the spectrum was affected mainly by the heating as the LSPR bleaching (Fig. 3-15a and b). In contrast, once a bubble was formed, calculated spectra show strong modification in the shape and amplitude in the spectra. For example, when the bubble diameters were 70−120 nm, strong bleaching was observed. Bleaching signals in the 450−490-nm region at 100−500 ps (Figure 3-3b) could be attributed to an embryonic bubble, rather than simply medium heating. Simulations also predicted an increase in the extinction with further increase in the bubble diameter and the appearance of positive wings on both sides of the LSPR band in the case that bubble diameters is >200 nm. According to the simulated results, the maximum diameter was estimated to be ~240 nm (a detailed analysis is given below). The calculation based on the Mie theory suggested that further increase in the bubble diameter might produce much bigger, positive extinctions due to the Rayleigh scattering.[2] The maximum bubble size is dependent on the excitation laser intensity.[16,17] Bubbles can expand until their internal pressure is balanced with the ambient pressure (~1 atm).[40] The experimental extinction signal could be well interpreted by the above mechanism. Consequently, through the bubble generation and growth mechanism, our spectral

simulations qualitatively reproduced strong bleaching in the 450−490 nm region as well as the subsequent appearance of positive extinctions on both sides of the LSPR band.

Temporal Evolution of Bubbles. Nanobubble formation is a transient event induced by a single shot of the laser and is not a stationary phenomenon by bulk heating or the accumulation of heat. We observed that the nanobubbles collapsed within 20 ns after the laser excitation. In the present section, we will quantitatively discuss the temporal evolution of the diameter of the bubble.

To estimate the diameter of the bubble from the experimentally obtained transient spectra, we used the relationship between C_{ext} and the bubble diameter from the simulated spectra, based on eq 3-4. Figure 3-16a shows C_{ext}(450 nm)/C_{ext}(535 nm) as a function of the bubble diameter. Experimental values of C_{ext}(450 nm)/C_{ext}(535 nm) were compared with the computational C_{ext}. According to eq 3-1, C_{ext}(450 nm)/ C_{ext}(535 nm) is equal to *Ext*(450 nm)/*Ext*(535 nm). The extinction was proportional to the particle concentration N and C_{ext}; the latter is a function of both particle temperature and bubble diameter. Under atmospheric pressure (0.1 MPa), the extinction signal appears immediately after the excitation due to the particle heating, followed by the evolution of the signal associated with the bubble. In this estimation, we need to extract the bubble-related extinction signal emitted during particle heating−cooling dynamics. These dynamics of Au NPs could be observed separately under the irradiation below the bubble formation. By applying the laser pulse of fluence 5 mJ cm^{-2}, which initiates bubbles at 0.1 MPa on the Au NPs. Thus, we obtained *ΔΔExt*(450 nm)/*ΔΔExt*(535 nm) as a function of time (Figure 3-16b). Finally, we can obtain the temporal evolution of the bubble diameter (Figure 3-16c) by converting the *ΔΔExt*(450 nm)/*ΔΔExt*(535 nm) value into the bubble diameter using Figure 3-16a as a calibration curve while assuming *ΔΔExt*(450 nm)/*ΔΔExt*(535 nm) = C_{ext}(450 nm)/ C_{ext}(535 nm). The curve gives the time-dependence for bubble generation, growth, and decay of a 60 nm-diameter Au NPs. The lifetime was estimated by the fwhm width to be roughly 10 ns, giving a maximum diameter of 260 ± 40 nm.

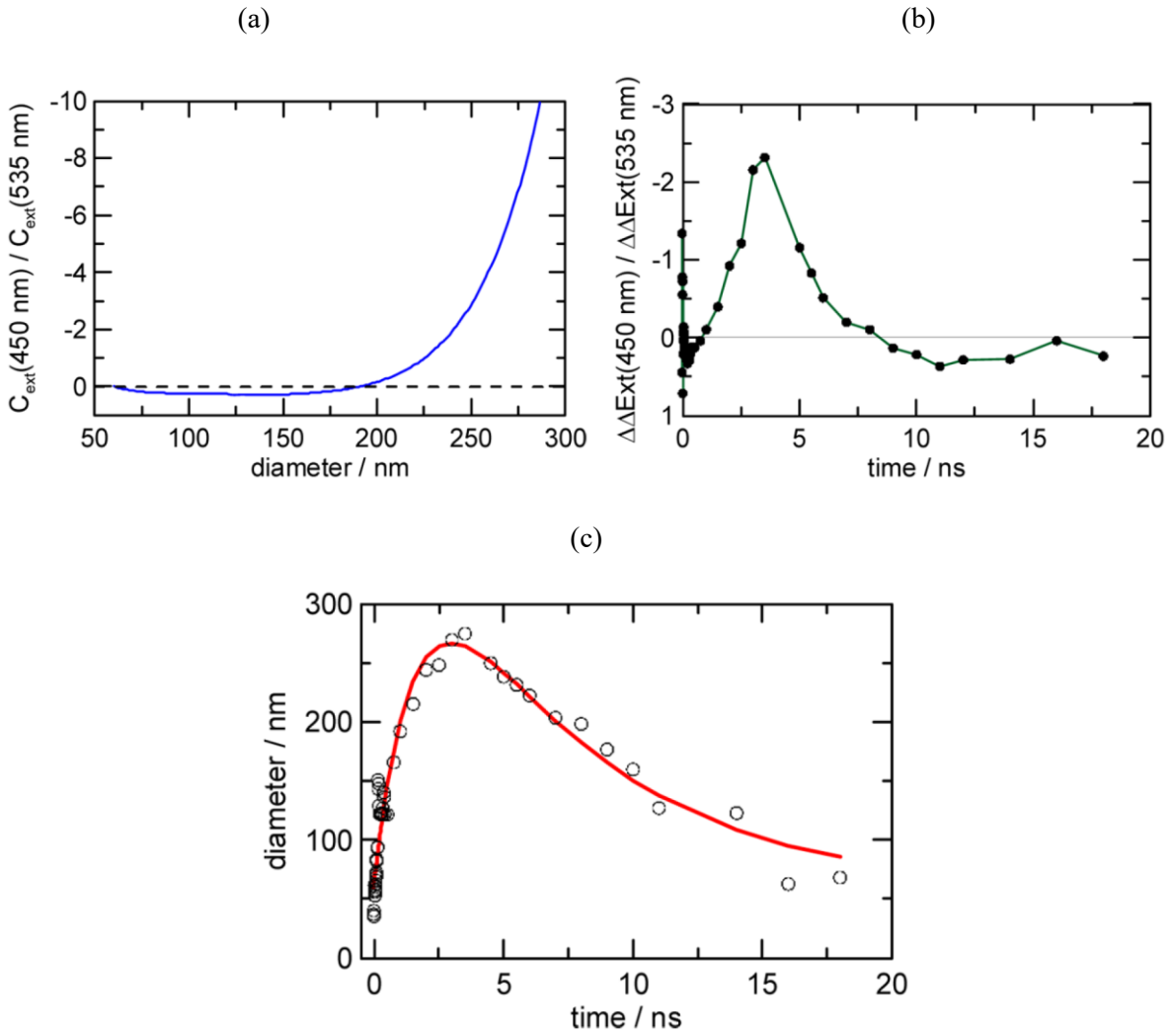

Figure 3-16. Temporal evolution of the bubble. (a) C_{ext} (450 nm)/C_{ext} (535 nm) versus bubble diameter obtained from the spectral simulation described in the text. (b) *ΔΔExt*(450 nm)/*ΔΔExt*(535 nm) versus time curve obtained from the experimental *ΔExt* versus time curves (errors: <±10%, estimated by the standard deviation) with *ΔΔExt*(450 nm) = *ΔExt*(450 nm, 0.1 MPa) − *ΔExt*(450 nm, 60 MPa), and *ΔΔExt*(535 nm) = *ΔExt*(535 nm, 0.1 MPa) − *ΔExt*(535 nm, 60 MPa) at various time delays. (c) Time profile of the bubble diameter. The red line is a calculated curve with the double exponential function, D(*t*) = -(447±113) exp{-*t* / (1.7±0.4) ns}+(454 ±115) exp{-*t* / (6.2±1.2)} +60. Errors in estimating diameters are ±20% obtained from the standard deviation of the fitting analysis.

Previous femtosecond ensemble studies of bubble dynamics using time-resolved X-ray measurements revealed that the lifetime of a bubble surrounding a Au NP with 9-nm diameter was 400 ps (max bubble diameter: 20 nm) at 40 mJ cm^{-2}, whereas that for a Au NP with 36-nm diameter was 1.7 ns (max bubble diameter: 75 nm) at 13.8 mJ cm^{-2} (threshold fluence).[6,20] The bubble dynamics were well modeled using the Rayleigh−Plesset equation.[40] Lapotko group measured bubble lifetimes by observing the optical scattering response of a single Au NP and reported 18 ± 3.5 ns for a Au NP with 30-nm diameter at a threshold fluence of 720 mJ cm^{-2}, and 9 ± 1 ns for single Au NPs with 90- and 250-nm diametera at a minimal fluence of 100 mJ cm^{-2} (for 0.5 ns, 532 nm laser excitation).[16–18] They found that the lifetime of bubbles around NPs increased with increasing fluence and that the lifetime was proportional to the maximum bubble diameter. These findings could be adequately described in the context of the Rayleigh−Plesset equation.[40]

We only measured the bubble dynamics at fluences near the threshold, because our pump−probe method required the accumulation of signals, which could cause severe particle deformation and possible destruction, leading to significant reduction in the extinctions at much higher fluences. A direct comparison between our results and literature values was not possible, because of the different particle heating rates that were produced by the various laser pulse durations. For instance, Lapotko group observed an appreciably long lifetime of approximately 60 ns for plasmonic nanobubbles after the off-resonant excitation of the LSPR band, for the excitation of Au nanospheres at specific wavelength such as 780 nm.[41,42] It should be noted, however, the lifetime in the present experiment was almost in the similar time scales obtained by the similar excitation condition. That is, the transient extinction spectroscopy, which is exactly the same set-up of transient absorption spectroscopy and much easier method to apply than the time-resolved X-ray measurement, can provide the dynamics of the bubble formation with the diameter of the bubble through the analysis of the extinction spectra.

The mechanism underlying the bubble formation is still being investigated. In addition, in studies related to bubble dynamics using optical imaging at a fixed time delay, Lapotko group observed, on the one hand, decreased scattering intensity at low fluence, and on the other increased scattering intensity at high fluence;[16,18] they observed bleaching ascribable to medium heating at low fluence and optical amplification

resulting from bubble formation at high fluence. These trends manifest themselves depending on the extent of medium heating and also on time delays, the latter of which comes from the mechanism similar to that responsible for the time-dependent decrease and increase in the extinctions observed here.

3-4. Conclusion

Conventional optical measurements of dynamics on plasmonic nano- and microbubbles were limited to the detection of light scattering and extinctions in the time region longer than sub-microseconds. In the present study, we extended the temporal resolution into the picosecond region by applying the transient extinction spectroscopy. Time evolution of transient spectra in the wavelength range of 400 – 900 nm revealed dynamics characteristic of formation and collapse of nanobubbles. For Au NPs under the picosecond pulsed irradiation, the nanobubble formation was characterized by the kinetic behavior on time scales shorter than 20 ns. The analysis based on the relation between the bubble size and the spectral shape provided detailed information on the temperature of Au NPs and the surrounding water. Once a bubble was formed, the overall extinction signal was dominated by the scattering component, with a minimal contribution from the Au NPs. The present study provides important and fundamental information for the investigation of various processes relating to the photothermal effects with colloidal nanoparticles induced by the ultrafast laser pulse, such as the application of plasmonic nanobubbles to the theranostics (diagnostics and therapy) of living malignant cells. The present method allowed the sensitive detection of plasmonic nanobubbles in the wide range of the fluence.

References

(1) Kreibig, U.; Vollmer, M. *Optical Properties of Metal Clusters*; Springer: Berlin, **1995**.

(2) Bohren, C. F.; Huffman, D. R. *Absorption and Scattering of Light by Small Particles*; Wiley: New York, **1983**.

(3) Baffou, G.; Quidant, R. *Laser Photonics Rev*. **2013**, 7, 171−187.

(4) Qin, Z.; Bischof, J. C. *Chem. Soc. Rev.* **2012**, 41, 1191−1217.

(5) Hashimoto, S.; Werner, D.; Uwada, T. *J. Photochem. Photobiol. C* **2012**, 13, 28−54.

(6) Kotaidis, V.; Plech, A. *Appl. Phys. Lett.* **2005**, 87, 213102.

(7) Kotaidis, V.; Dahmen, C.; Von Plessen, G.; Springer, F.; Plech, A. *J. Chem. Phys*. **2006**, 124, 184702.

(8) Lapotko, D.; Lukianova, E.; Shnip, A.; Zheltov, G.; Potapnev, M.; Savitsky, V.; Klimovich, O.; Oraevsky, A. *Proc. SPIE* **2005**, 5697, 82−89.

(9) Lapotko, D. O.; Lukianova, E.; Oraevsky, A. A. *Lasers Surg. Med.* **2006**, 38, 631−642.

(10) Neumann, J.; Brinkmann, R. *J. Biomed. Opt.* **2005**, 10, 024001.

(11) Neumann, J.; Brinkmann, R. *J. Appl. Phys.* **2007**, 101, 114701.

(12) Neumann, J.; Brinkmann, R. *Appl. Phys. Lett.* **2008**, 93, 033901.

(13) Mock, J. J.; Barbic, M.; Smith, D. R.; Schultz, D. A.; Schultz, S. *J. Chem. Phys.* **2002**, 116, 6755−6759.

(14) Sönnichsen, C.; Franzl, T.; Wilk, T.; von Plessen, G.; Feldmann, J.; Wilson, O.; Mulvaney, P. *Phys. Rev. Lett.* **2002**, 88, 077402.

(15) Zijlstra, P.; Orrit, M. *Rep. Prog. Phys.* **2011**, 74, 106401.

(16) Lukianova-Hleb, E. Y.; Lapotko, D. O. *Nano Lett.* **2009**, 9, 2160−2166.

(17) Lapotko, D. O. *Opt. Express* **2009**, 17, 2538−2556.

(18) Lukianova-Hleb, E. Y.; Latterini, L.; Tarpani, L.; Lee, S.; Drezek, R.; Hafner, J.; Lapotko, D. O. *ACS Nano* **2010**, 4, 2109−2123.

(19) Siems, A.; Weber, S. A. L.; Boneberg, J.; Plech, A. *New J. Phys.* **2011**, 13, 043018.

(20) Plech, A.; Kotaidis, V.; Grésillon, S.; Dahmen, C.; Von Plessen, G. *Phys. Rev. B* **2004**, 70, 195423.

(21) Frens, G. *Nat. Phys. Sci.* **1973**, 241, 20−22.

(22) Miyasaka, H.; Moriyama, T.; Itaya, A. *J. Phys. Chem.* **1996**, 100, 12609−12615.

(23) Werner, D.; Hashimoto, S. *Langmuir* **2013**, 29, 1295−1302.

(24) Inouye, H.; Tanaka, K.; Tanahashi, I.; Hirao, K. *Phys. Rev. B* **1998**, 57, 11334.

(25) Link, S.; El-Sayed, M. A. *Annu. Rev. Phys. Chem*. **2003**, 54, 331−366.

(26) Burda, C.; Chen, X.; Narayanan, R.; El-Sayed, M. A. *Chem. Rev.* **2005**, 105, 1025−1102.

(27) Hartland, G. V. *Chem. Rev*. **2011**, 111, 3858−3887.

(28) Logunov, S. L.; Ahmadi, T. S.; El-Sayed, M. A.; Khoury, J. T.; Whetten, R. L. *J. Phys. Chem. B* **1997**, 101, 3713−3719.

(29) Hu, M.; Hartland, G. V. *J. Phys. Chem. B* **2002**, 106, 7029−7033.

(30) Weingärtner, H.; Franck, E. U. *Angew. Chem., Int. Ed.* **2005**, 44, 2672−2692.

(31) Werner, D.; Ueki, T.; Hashimoto, S. *J. Phys. Chem. C* **2012**, 116, 5482−5491.

(32) Caupin, F.; Herbert, E. *C. R. Phys.* **2006**, 7, 1000−1017.

(33) Cavicchi, R. E.; Meier, D. C.; Prabhu, V. M.; Guha, S. *J. Phys. Chem. C* **2013**, 117, 10866−10875.

(34) Inasawa, S.; Sugiyama, M.; Noda, S.; Yamaguchi, Y. *J. Phys. Chem. B* **200**6, 110, 3114−3119.

(35) Setoura, K.; Werner, D.; Hashimoto, S. *J. Phys. Chem. C* **2012**, 116, 15458−15466.

(36) Otter, M. *Z. Phys.* **1961**, 161, 539−549.

(37) Liz-Marzan, L. M.; Mulvaney, P. *New J. Chem.* **1998**, 22, 1285−1288.

(38) Link, S.; El-Sayed, M. A. *J. Phys. Chem. B* **1999**, 103, 4212−4217.

(39) Setoura, K.; Okada, Y.; Werner, D.; Hashimoto, S. *ACS Nano* **2013**, 7, 7874−7885.

(40) Plesset, M. S.; Prosperetti, M. *Annu. Rev. Fluid Mech.* **1977**, 9, 145−185.

(41) Lukianova-Hleb, E. Y.; Sassaroli, E.; Jones, A.; Lapotko, D. O. *Langmuir* **2012**, 28, 4858−4866.

(42) Lukianova-Hleb, E. Y.; Volkov, A. N.; Wu, X.; Lapotko, D. O. *Adv. Mater.* **2013**, 25, 772−776.

4. Thermometry using Optical Scattering Spectra for a Single Gold Nanoparticle under CW Laser Irradiation: Nanoscale Cooling of Substrates and the Surrounding Media

ABSTRACT

Although elucidation of local thermal responses induced by the nanoscale heating is crucially important, it is usually difficult to directly obtain the information on temperatures in such small space. This chapter describes the laser-induced heating and thermal equilibration of metal nanoparticles supported on different substrates and immersed in several media, leading to the estimation of the temperature in the tiny space. We used single-particle spectroscopy to monitor the temperature rise of nanoparticles and surrounding media under the laser excitation. Change in the refractive index of the surrounding medium affects the scattering spectrum of the gold nanoparticles in its maximum and band shapes. In addition, the supporting substrate also influences the temperature change. We furthermore modeled the nanoparticle temperature using a simplified 1-D heat conduction with an effective thermal conductivity by taking both substrate and environment into account. The results analyzed by this model are also compared with a more detailed 2-D heat transfer analysis. The results presented here are quite new and important to many applications of plasmonic nanoparticle where the strong absorption cross section of the nanoparticles leads to a significant temperature rise. In this chapter, we also introduced in detail the analysis method that can be easily implemented to model the temperature of a nanoparticle supported on a substrate, as is the case in many single-particle measurements.

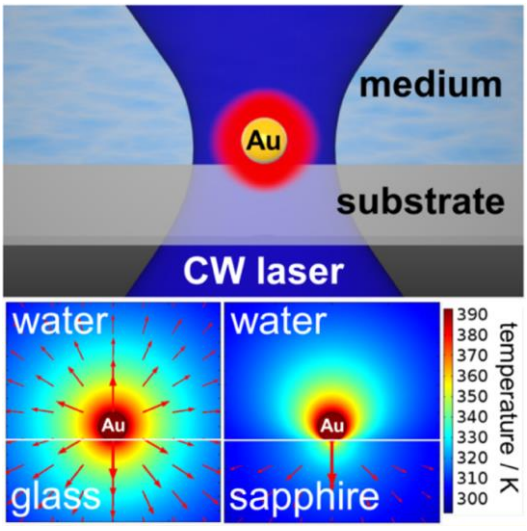

4-1. Introduction

As presented in previous chapters, plasmonic nanoparticles (NPs) have emerged as nanoscale heat sources, the heating power of which can be controlled remotely through optical excitation.[1-3] Simultaneously, heat transfer from the NPs enables the surrounding medium to be heated. Within the limited time scales imposed by irradiation periods, medium heating is confined to a nanospace accompanied by a temperature gradient. This unique attribute of plasmonic heating has potential applications to photothermal cancer therapy and nanofabrication.[4-7]

To gain deeper insight into the photothermal response of plasmonic NPs, investigation of thermal processes and properties of a single particle is crucially important. Single-particle spectroscopy has a big advantage in tracking the properties and reactions of individual NPs, including the effects of the ambient environment, by monitoring continuous spectral peak shifts and their changes in spectral shapes. Such observations are not possible with ensemble measurements that are subject to distributions in particle size and shapes with inhomogeneous spectral broadening.[8] The single-particle approach has another advantage in tracking and manipulating single NPs with high temporal and spatial resolutions. Single-particle studies using plasmonic heating by continuous wave (CW) laser illumination have been reported so far. For instance, bubble-induced damaging of polyelectrolyte films that mimic cell membranes or biological tissues has been demonstrated.[9] Thermal imaging of nanostructures has also been conducted using quantitative optical phase analysis.[10] Moreover, nanochannel milling in polyvinyl alcohol films driven by a laser-manipulated Au NP, as well as laser embedding of an Au NP in polymeric films, has been developed.[11,12] However, in situ measurements of temperature of these Au NPs are limited to only a few cases.[13-15]

We have recently devised a method to measure the temperature of a single Au NP under CW-laser illumination, as introduced in Chapter 2.[16] Based on spectral calculations with Mie theory, experimental data on the peak shifts of the scattering spectrum of localized surface plasmon resonance (LSPR) bands were exploited to estimate the temperatures of nanoparticles in the range 300 - 600 K with an accuracy of $\pm$20 K. The method has the advantage of acquiring particle temperatures without a calibration coefficient such as a temperature transfer coefficient or relying on thermophysical calculations containing unknown parameters.[13] Accordingly,

temperature of particles could be determined without the influence of the spatial resolution of the optical setup. We also observed that the surrounding media such as water and glycerol affect the spectral shifts through the temperature dependent refractive index. This result prompted us to investigate medium and substrate effects on the particle temperature. Essentially, both the surrounding medium and substrate can be regarded as a heat sink, the capability of which is determined by their thermal conductivities

To estimate the temperature of plasmonic nanostructures under the steady-state heating, the most convenient way is to apply the one-dimensional (1-D) heat conduction equation.[17] The equation can be applied to a spherical NP immersed in a homogeneous medium (Scheme 4-1a). However, unless particles are suspended by a laser-trapping technique, NPs are usually supported on a substrate. Heat transfer for this system is complicated because of the presence of the substrate (Scheme 4-1b).

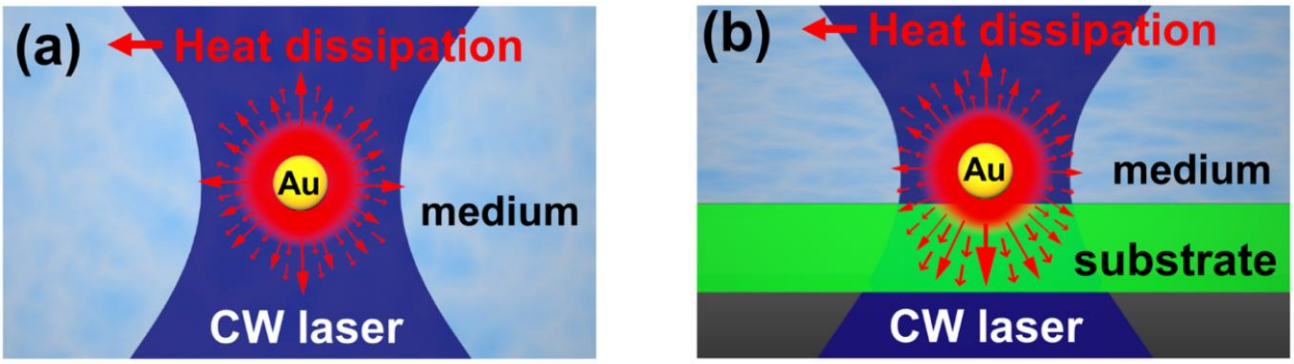

Scheme 4-1. Schematic illustrations of heat dissipation for an Au NP under steady-state laser illumination, in a homogeneous medium (a) and supported on a substrate and immersed in a medium (b).

In the application of the 1-D heat conduction equation to such a complex system, the averaged thermal conductivity of the medium and substrate has been used as the thermal conductivity of the medium.[9,13] This averaging may be applicable for the system with small disparity of thermal conductivity, such as the water/glass system. However, it is not clear whether the concept of averaged thermal conductivity is applicable to cases with a large thermal conductivity disparity between medium and substrate.

In this chapter, we show, for a single Au NP, observation of a substrate/medium-dependent temperature increase that is proportional to the intensity of the illuminating laser. Substrate and medium were found to contribute significantly to particle cooling that governs the efficiency of laser heating. As a result, we made a reasonable estimation of the effective thermal conductivities k_{eff} for several medium-substrate systems by applying the 1-D heat transfer model. This method can properly estimate the temperature of a particle under laser illumination. Herein, we evaluated the adequacy of the experimental k_{eff} based upon the numerical calculations of particle temperatures.

4-2. METHODS

Sample Preparation. Aqueous solutions of Au NPs with nominal diameters of 100 nm (cat. no. EMGC100, 100 ± 8 nm) were purchased from British Biocell International. Although NPs are initially faceted, these were smoothed into spheres by irradiating with weak-intensity nanosecond laser pulses at 532nm (~10 mJ cm^{-2}). The Au NPs were spin-coated onto a substrate both of which sides were cleaned in a plasma reactor (Sakigake, YHS-R (70 W, 20 kHz)) for 30 s. The Au NPs were washed three times with doubly distilled water by placing in 0.5 mL of water and spin-coated. Three types of substrate were employed: borosilicate glass (Schott D263T, 24 mm × 32 mm × 0.17 mm coverslip), sapphire (Furuuchi Chemical, 10 mm × 10 mm × 0.5 mm, optically polished on both sides), and CaF_2 (OKEN, 10 mm × 10 mm × 0.5 mm, optically polished on both sides). The substrate coated with Au NPs was mounted on the scanning stage (Sigma, BIOS-105T, 100-nm resolution) of an optical microscope. In addition to this sample preparation, the Au NPs on a substrate were immersed in either water (doubly distilled) or glycerol (Merck, microscopy grade) in a 90 μL chamber consisting of two substrates separated by a 0.3-mm-thick silicone rubber spacer.

Optical Measurements. Forward light scattering spectra of single Au NPs were measured using a dark-field light microscopy-spectroscopy setup (Figure 4-1).[16] The spectra were obtained by subtracting the background signals including Raman scattering of the surrounding media and photoluminescence of the NP, then dividing it by the spectral profile of the white-light excitation source. Laser irradiation was carried out through a microscope objective (60X, NA = 0.70) in an inverted microscope (Olympus IX 71 with a U-DCD dark-field condenser (NA = 0.8-0.92)) equipped with two output ports. The output from one port was relayed to a spectrograph consisting of an Acton SP300i polychromator (grating: 150 grooves/mm, blazed at 500 nm) and an Andor CCD camera (type: DU401-BR-DD operated at 60 °C) through a 300-μm diameter pinhole, whereas the output from the other port was used for imaging with a digital camera (Nikon, DS-5M). The dark-field microscopy-spectroscopy was used to select a single particle that was subjected to laser irradiation (Figure 4-1). Particles were brought to the laser spot by scanning a sample in the chamber on the motorized stage. The excitation of a single Au NP was performed using a focused 488 nm CW laser (NEOARK, TC20- 4860-4.5)

beam. The laser power was measured using a photo- diode power meter (OPHIR, Orion). Spatial laser profile was determined by measuring scattering signal intensity of the 100-nm diameter Au NP while scanning the stage at 100 nm intervals. The laser beam diameter thus determined was 1.2 μm, although a calculated $1/e^2$ diameter was 0.5 μm assuming a Gaussian beam profile and using experimental optical parameters (NA = 0.70, λ = 488 nm, n = 1.33). The laser peak power density I_p (mW μm^{-2}) was represent by,[13]

$$I_p = \frac{P(2.3546)^2}{2\pi(\mathrm{FWHM})^2}$$

where P is the laser power density (measured laser power divided by beam area).

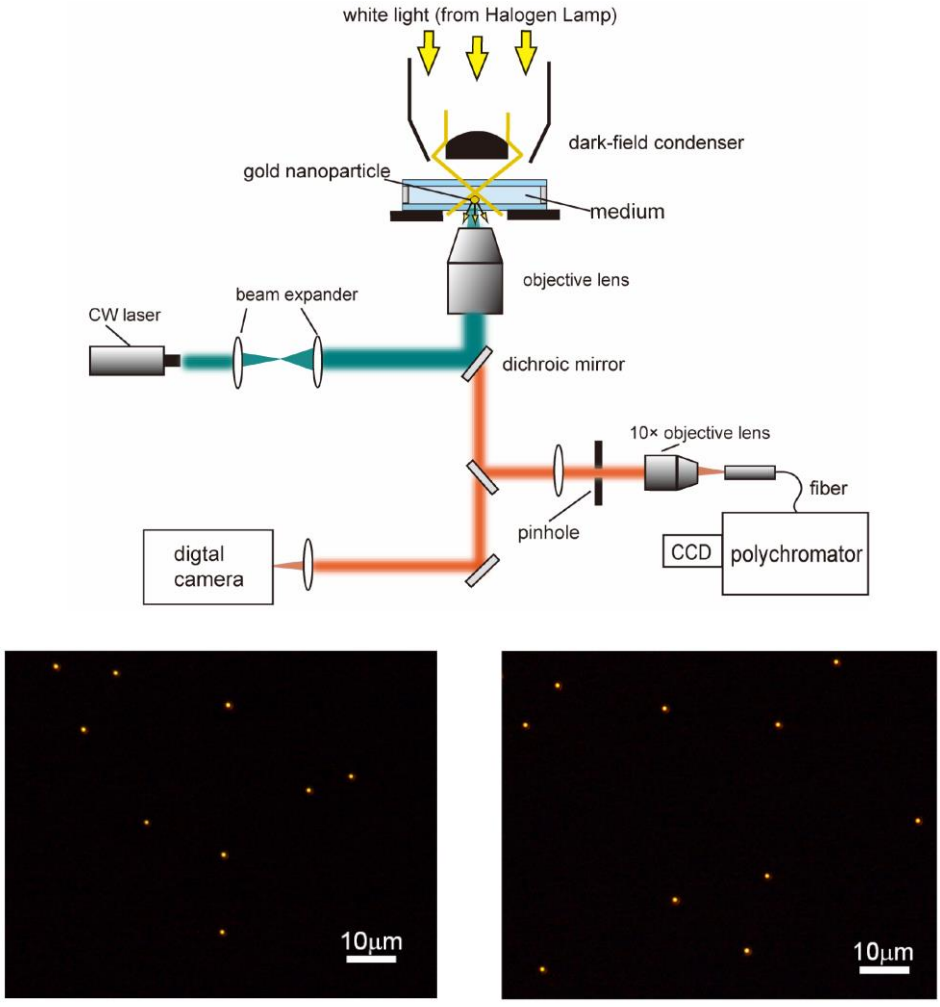

Figure 4-1. Experimental setup and dark field images of d=100nm Au NPs supported on a glass substrate and immersed in water (60X, NA=0.70 objective lens).

4-3. RESULTS and DISCUSSION

Estimation of Temperatures of a Single Au NP under CW-Laser irradiation. Laser irradiation induces the temperature elevation of Au NPs reaching a steady-state temperature under the CW laser irradiation, resulting from plasmonic heating followed by heat dissipation to the surrounding medium. This temperature increase causes the LSPR spectral damping.[18,19] This damping is accompanied with spectral peak shifts from which temperature information could be estimated.[16] For Au NPs on a substrate immersed in a medium, heat transfer is a complicated process because of the presence of three interfaces, such as the NP-medium, the NP-substrate, and the medium-substrate. Thus, to track heat transfer processes in such a system, temperature information for the particle is crucially important. The advantage of the measurement of scattering spectra over the fluorescence sensor approach is that the former method is possible to access particle temperature directly without being obscured by the diffraction-limited volume of the focal spot.[16] Here, we describe our attempt to observe substrate-dependent particle temperatures for substrates with different thermal conductivities

Figure 4-2 shows the scattering spectra from a single 100-nm diameter Au NP supported on three substrates, glass, CaF_2, and sapphire, which were immersed in water; the spectra were obtained under 488 nm CW-laser irradiation. Upon excitation, substrate-dependent peak shifts were clearly observed. For instance, at the excitation laser intensity of 4.7 mW μm^{-2}, an appreciable blue shift (Figure 4-2a) and the distinctive damping was observed in water/glass.

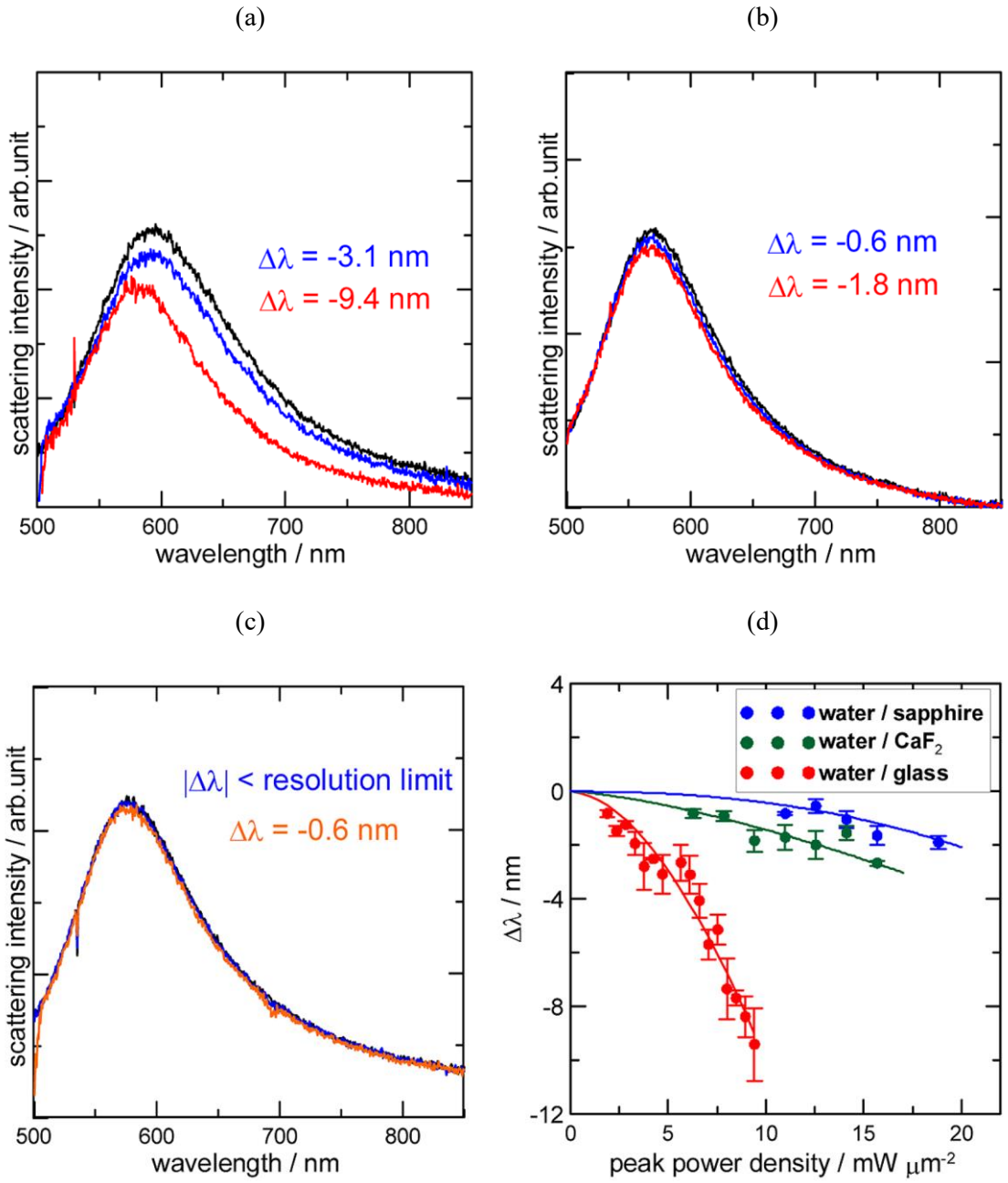

Figure 4-2. Experimentally obtained spectral changes of a single Au NP with a 100-nm diameter, supported on glass, CaF_2, and sapphire in water: (a) water/glass, (b) water/CaF_2, and (c) water/sapphire. Black curves indicate spectra without CW-laser irradiation; blue, red, and orange curves indicate spectra from excitation at 4.7, 9.4, and 11.0 mW μm^{-2}. (d) the relation between the peak shift $\Delta\lambda$ and the laser peak power density for the above three systems.

In contrast, the spectral changes at the same excitation intensity in water/CaF_2 and water/sapphire were not so remarkable (see Figure 4-2b and c). The origin of the blue shift is ascribed to temperature effect of the refractive index of the surrounding water. The substrate dependence could be attributed to the thermal conductivities of the substrates. That is, the blue shifts in water/CaF_2 and water/sapphire were noticeably suppressed because these substrates have thermal conductivities much higher than glass, and the temperature increase of a supported Au NP is lower than in the water/glass system. The peak shifts and $\Delta\lambda$ vs laser peak power density curves in the above three systems are summarized in Figure 4-2d; parabolic curves are drawn because the temperature dependence of the refractive index for water is parabolic. When the substrates were immersed in glycerol instead of water, we again observed blue shifts, the magnitude of which increased with increasing laser intensity (Figure 4-3). Note here that the curves are linear because of the linearity of the refractive index with temperature. Larger $\Delta\lambda$ values were observed in glycerol, as a reflection of its lower thermal conductivity and dn/dT values than those of water.

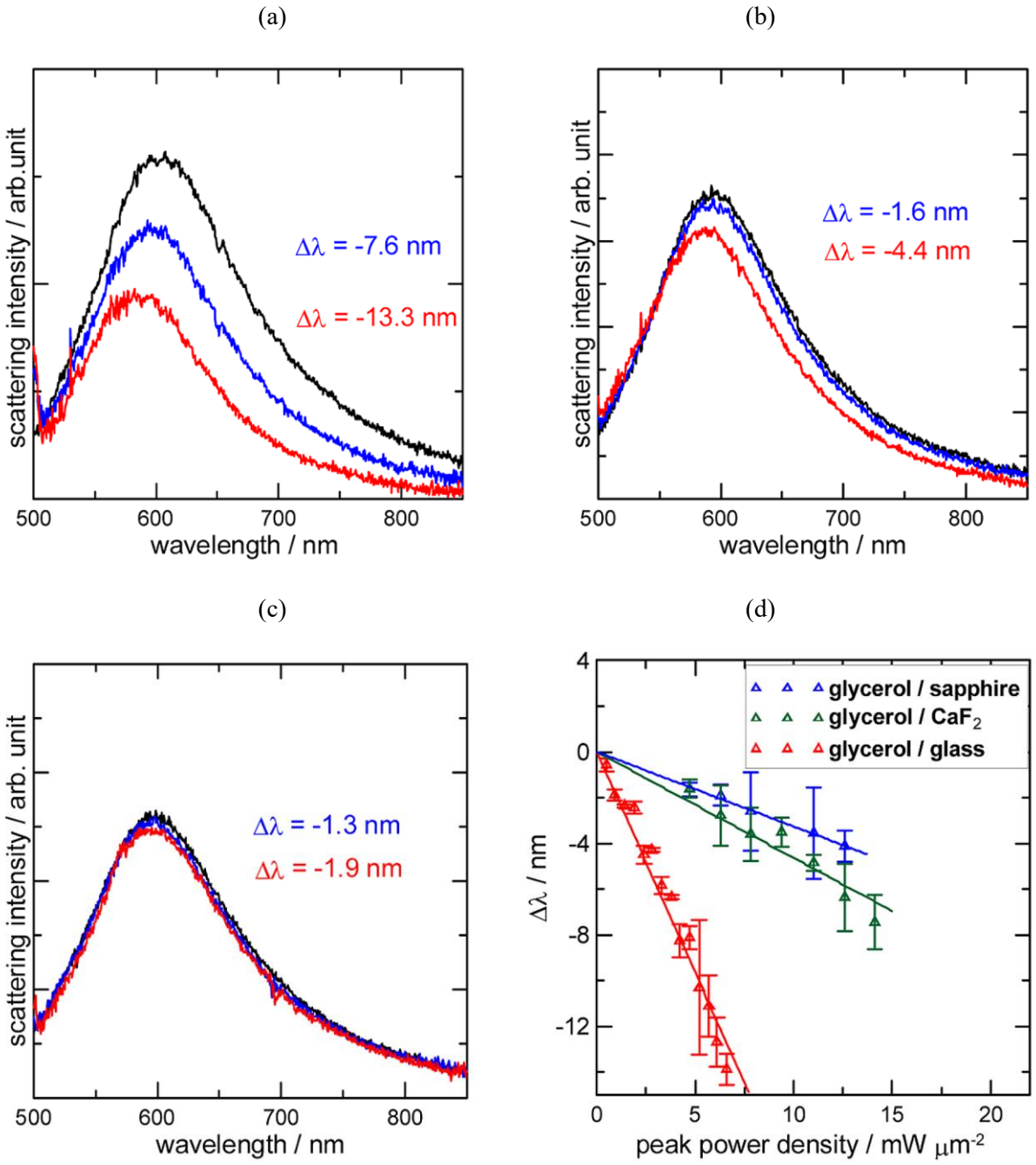

Figure 4-3. Experimentally observed scattering spectra of a single Au NP with a 100-nm diameter under the irradiation, supported on glass, CaF_2, and sapphire substrates submerged in glycerol: (a) glycerol/glass, (b) glycerol/CaF_2, and (c) glycerol/sapphire. Blue shifts were observed. Black lines are the spectra without laser illumination. Blue and red lines are the spectra under the irradiation with intensities of 4.7 and 6.6 mW μm^{-2}. (d) Peak shifts, $\Delta\lambda$, as a function of laser peak power density for the three systems.

In contrast, smaller red shifts of the scattering spectra were observed in the air with increasing peak power density (Figure 4-4). For the NP surrounded by air, red shifts can be mainly ascribed to the temperature dependence of an intrinsic property of Au NPs, arising from changes in the conduction electron scattering frequency.[18,19] (Note that the temperature coefficient of the refractive index of air is negligibly small.) A possible cause for the scattering spectral shifts is that an adsorbed water layer with a thickness of a few nanometers forms on the substrate surface in an ambient atmosphere.[20,21] Supposing that the substrate heating causes the vaporization of adsorbed water, blue shifts can result if the refractive index around an Au NP is decreased. However, this was not observed in air; thus, the effect of coadsorbed water on the substrates is negligibly small. Among the three substrates, sapphire exhibits the strongest cooling effect, followed by CaF_2 and then glass. That is, the results clearly showed the quantitative difference in the cooling effects of the substrate and medium during plasmonic heating of an Au NP in terms of the scattering spectral peak shifts, $\Delta\lambda$.

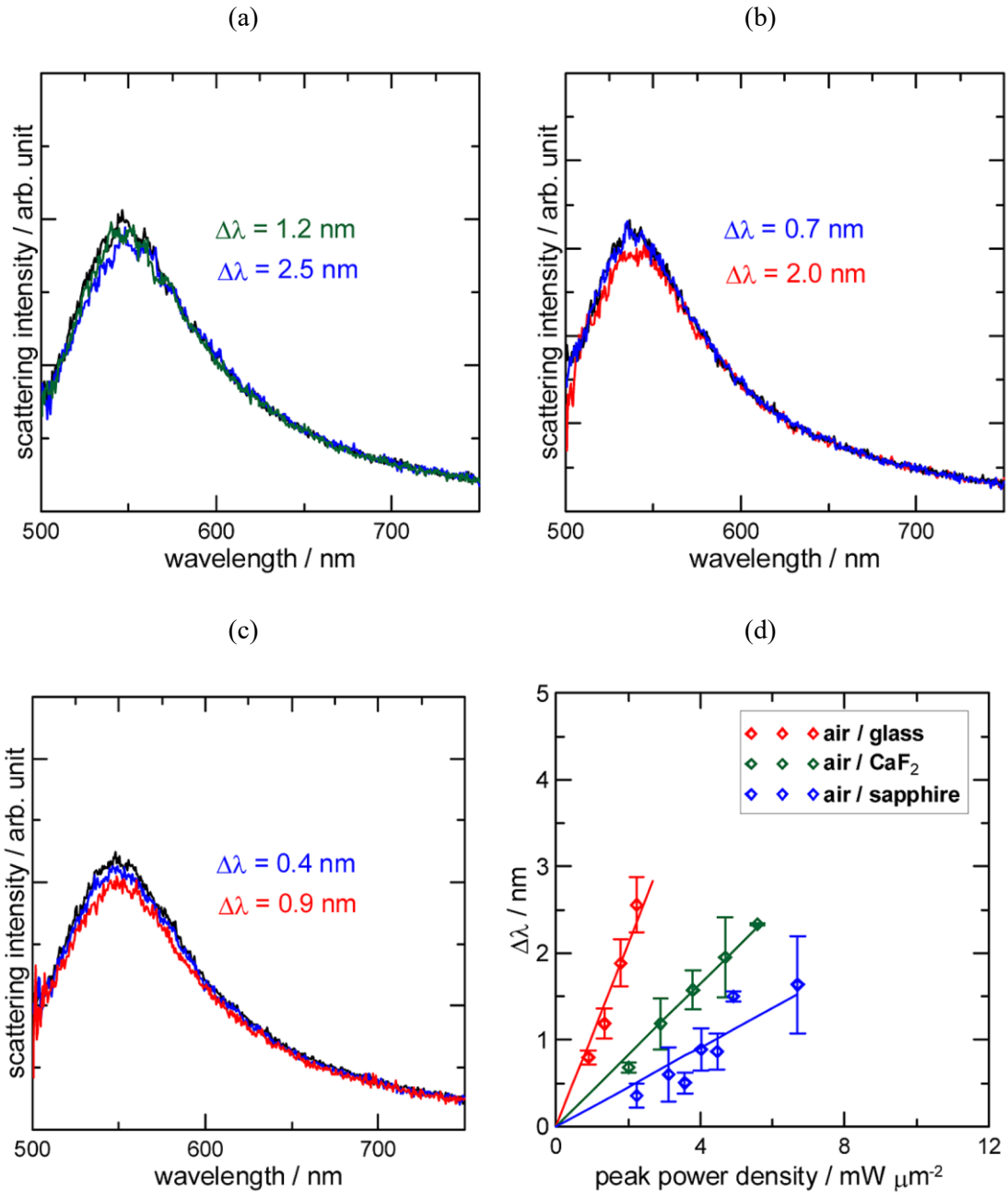

Figure 4-4. Experimentally observed scattering spectra of a single Au NP with a 100-nm diameter under the laser irradiation, supported on glass, CaF_2, and sapphire substrates in air: (a) air/glass, (b) air/CaF_2, and (c) air/sapphire. Here, red shifts were observed. Black lines are spectra without laser illumination. Green, blue, and red solid lines are the spectra under the laser irradiation at 1.3, 2.2, and 4.5 mW μm^{-2}. (d) Peak shifts, $\Delta\lambda$, as a function of laser peak power density in the above three systems.

Estimation of Effective Thermal Conductivities for Various Medium/Substrate Pairs.

The peak shifts of scattering spectra, $\Delta\lambda$, were measured at various laser intensities (peak power densities) for the three selected substrates in air, water, and glycerol, thus enabling estimation of the temperature of particles, T_p. We previously reported a method for estimating the temperature of Au NPs under CW laser illumination.[16] In this treatment, temperature of particles were determined by comparing the peak positions of experimentally measured scattering spectra with those of the temperature dependence calculated using Mie theory.[22,23] In this calculation, the temperature-dependent dielectric functions were obtained by fitting to the experimental values reported by Otter et al. for the range of 450 - 700 nm at four temperatures: 283, 583, 843, and 1193 K.[24] In addition, the gradient of refractive indices of the media, water, and glycerol was taken into consideration in T_p calculations. Temperature coefficients for the refractive indices of substrates are one order of magnitude smaller than those of water and glycerol. Therefore, we considered that the refractive index of substrates contributes negligibly to the spectral shifts. The method gives a direct measure of the temperature increase by laser heating, irrespective of the spatial resolution of the optical setup. The particle temperatures thus obtained can be used to identify cooling effects as differences in T_p for various substrates and media.

An analytical formula for a simple 1-D heat conduction equation has been established to estimate the local heating by a NP in a homogeneous medium (Scheme1a). The temperature profile, *T(r)* [K], is given by[1-3,13,15,17,25]

$$T(r) = T(\infty) + \frac{C_{abs}I}{4\pi kr} \quad (r \geq a: \text{NP radius}) \qquad (4\text{-}1)$$

where *r* [m] is the radial coordinate, *T(r)* [K] ambient temperature, C_{abs} [m^2] absorption cross section of Au NP at the excitation wavelength, and *I* [W m^{-2}] peak power density of the excitation laser. To apply the 1-D heat conduction equation to a complex system consisting of NP, medium, and substrate, the thermal conductivity of the surroundings (medium and substrate) was represented by an effective (averaged) thermal conductivity $\bar{k}$ [W m^{-1} K^{-1}],[9,13] as represented by eq 4-2.

$$\bar{k} = \frac{k_{med}+k_{sub}}{2} \qquad (4\text{-}2)$$

Here, k_{med} and k_{sub} are respectively the thermal conductivities of the medium and that of the substrate. In addition, the finite interface resistivity is defined in such a way that the finite temperature discontinuity occurs at the interface between the NP surface and the surrounding medium. This parameter plays a main role in describing the observed temperature drop at this interface during femtosecond/nanosecond pulsed-laser excitation.[26-30] This parameter, however, can be negligible in steady-state heating of Au NPs, as temperature drops are slight at the NP/medium interface. In the derivation of eq 4-1, the particle temperature was assumed constant because of the sufficiently high thermal conductivity of gold (314 W m^{-1} K^{-1}). Thus, for particle radius a, $T(a) = T(r < a) = T_p$ is implicitly assumed.

Here, we look at our experimental T_p, and its dependency on the substrates, and their intrinsic thermal conductivities. Figure 4-5 shows the peak power density vs T_p, for three substrates in water, which was estimated from the laser power-dependence of $\Delta\lambda$ (a) and the comparison with the same relationship obtained by the calculation with eq 4-2 (b). Figure 4-5 clearly shows the T_p values being proportional to the laser intensities. Linear relationships between the experimental T_p and the laser intensity were observed also in glycerol and air (Figure 4-6). The laser intensities were adjusted subject to T_p < 600 K to avoid softening or melting of the substrates.[16] Figure 4-6b was drawn by applying eq 4-1 using parameters described in the caption. C_{abs} values at 488 nm were obtained using Mie theory with the effective medium refractive indices, ε_{eff}. Both experimental values and the conventionally calculated ones of T_p exhibit a linear relationship with laser intensity (Figure 4-5a and b). This suggests that the experimental T_p is adequately described by eq 4-1 and the experimental slope can be used to calculate k_{eff} for each medium/substrate pair, leading to the determination of k_{eff} values for various medium/substrate systems. The results are listed in Table 4-1. The experimental k_{eff} values in water/glass and glycerol/glass are in good agreement with conventional $\bar{k}$ values. In contrast, for other systems, a noticeable disagreement was observed. The difference between k_{eff} and $\bar{k}$ is large, especially for air as well as the sapphire substrate. The largest difference was observed for air/sapphire where $\bar{k}$ assumes 20 times the experimental k_{eff} value.

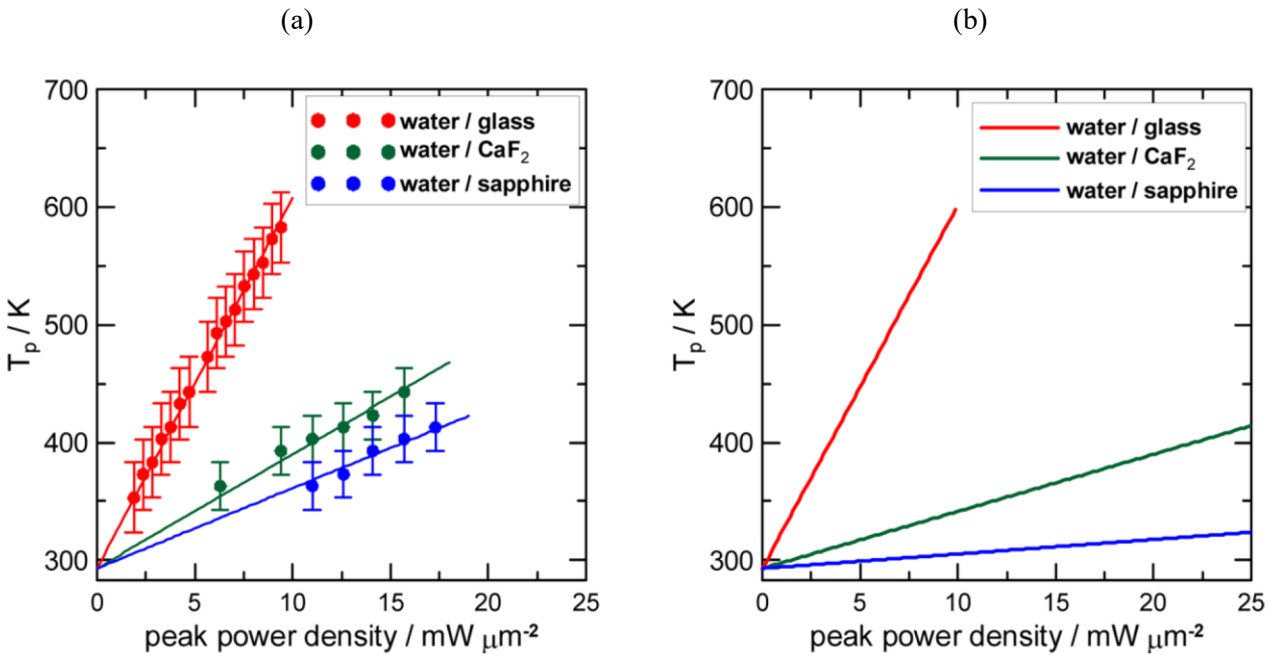

Figure 4-5. Laser peak power density vs T_p relationship estimated from experimental results on the laser power dependence of $\Delta\lambda$ (a) and computational curves applying eq 4-1 with $\bar{k}$ instead of k (b) for a 100-nm diameter Au NP supported on the three substrates in water. Errors in experimental temperature estimation were 20 K. For the calculation using eq 4-1, the $\bar{k}$ values listed in Table 4-1 were used.

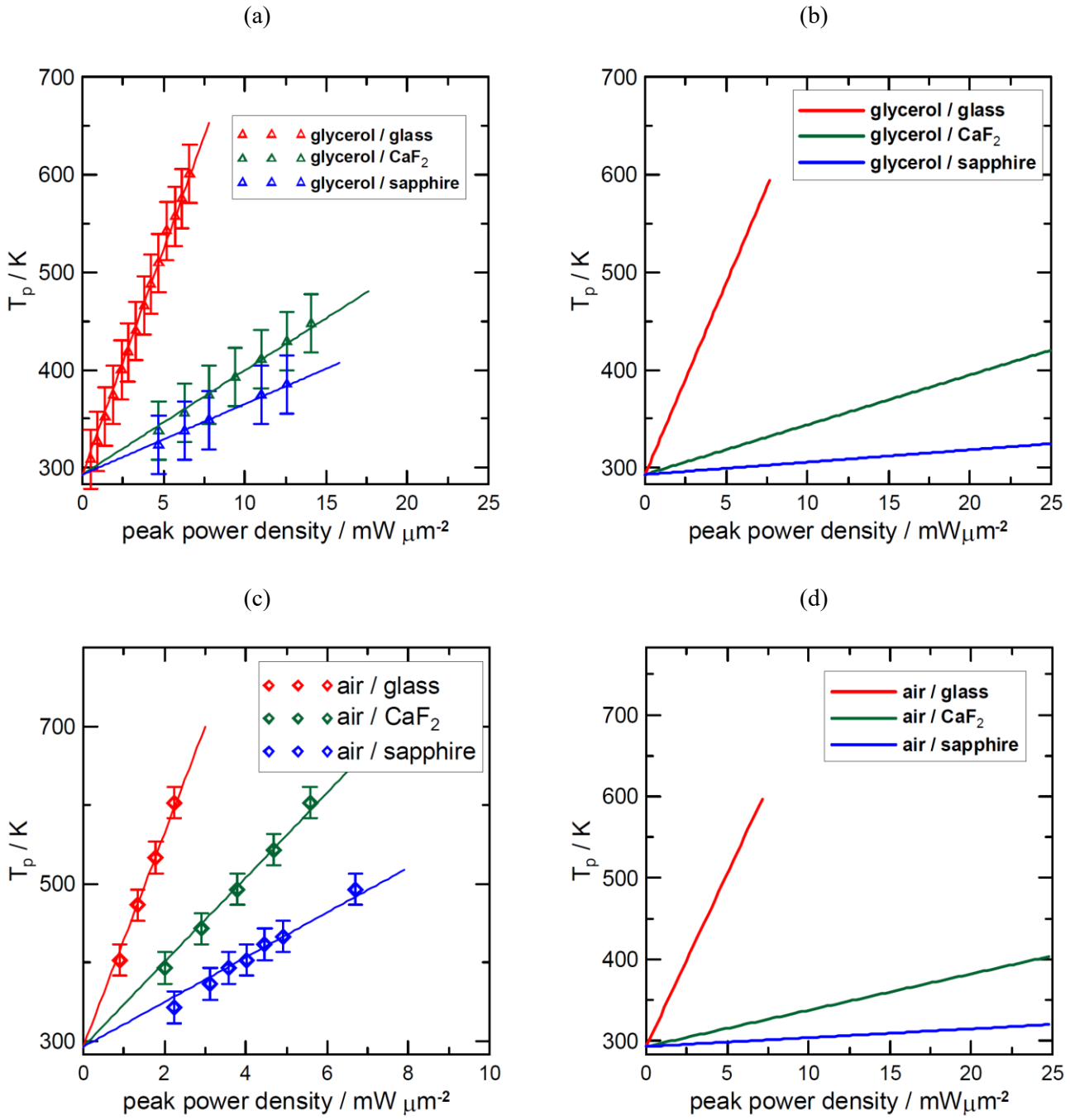

Figure 4-6. The peak power density *vs*. T_p estimated from experimentally observed laser power-dependence of $\Delta\lambda$: (a) and (c), in comparison with the same relationship obtained by calculation in terms of equation 4-3. (a) and (b) for three substrates in glycerol; (c) and (d) in air.

Table 4-1. Comparison of experimental k_{eff}, conventional $\bar{k}$, and computational k_{eff} (unit: W m^{-1} K^{-1})

medium/substrate	k_{eff} (exp t)	$\bar{k} = (k_{med}+k_{sub})/2$	k_{eff} (COMSOL)
air/glass	0.2 ± 0.1	0.51	0.23
air/CaF_2	0.6 ± 0.2	4.87	0.54
air/sapphire	1.1 ± 0.2	20.01	0.60
water/glass	0.8 ± 0.2	0.8	0.80
water/CaF_2	2.7 ± 0.5	5.16	3.25
water/sapphire	3.9 ± 1.0	20.3	5.43
glycerol/glass	0.6 ± 0.1	0.65	0.55
glycerol/CaF_2	2.5 ± 0.5	5.01	2.44
glycerol/sapphire	3.7 ± 1.4	20.15	3.85

2-D Heat Conduction Analysis and Particle Temperature Calculation.

The disagreement between k_{eff} and $\bar{k}$ indicates inadequacy in obtaining the effective medium thermal conductivity by averaging k_{sub} and k_{med} in the 1-D heat transfer analysis. This may be due to the non-uniform heat transfer from the particles. Therefore, we applied 2-D heat conduction equations to visualize the heat transfer around an Au NP as a heat source while supported on a substrate and immersed in a medium. We considered a steady-state solution for a CW-laser heating to calculate the 2-D (x-z plane) temperature distributions. The Poisson and Laplace forms of the heat conduction equations are represented by eqs 4-3, -4, and -5.

$$k_{NP}\nabla^2 T(x,z) = Q(x,z) \qquad (4\text{-}3)$$

$$k_{med}\nabla^2 T(x,z) = 0 \qquad (4\text{-}4)$$

$$k_{sub}\nabla^2 T(x,z) = 0 \qquad (4\text{-}5)$$

Here, k is the thermal conductivity, Q is the heat source. The subscripts NP, med, and sub refer to the Au NP, the medium, and the substrate. The origin of the coordinates x (horizontal) and z (vertical) axes is set on the surface of the substrate, at the contact point of NP and the surface. Thus z^+ represents the medium side and z^- represents the substrate side. Equations 4-3 to 4-5 describe the heat conduction in the NP, the medium, and the substrate, respectively; the boundary condition at $(x^2 + (z - a)^2)^{1/2} = a$ (NP/medium interface) is

$$k_{NP}\partial_{x,z}T(a^+) = k_{med}\partial_{x,z}T(a^-),\ T(a^+) = T(a^-) \qquad (4\text{-}6)$$

where a^+ and a^- distinguish the inner and outer surfaces of the particle. The boundary condition at z-0(medium/substrate interface) is

$$k_{med}\partial_{x,z}T(z^+) = k_{sub}\partial_{x,z}T(z^-),\ T(z^+) = T(z^-) \qquad (4\text{-}7)$$

These parameters were basically the same as those used in the analysis of the behaviors induced by the femtosecond laser excitation.[29]

Under steady-state heating, heat loss at each interface was assumed negligible because of a smaller contribution to the resistivity from the finite interface. For nanoscale laser heating of a substrate-single plasmonic nanostructure in a liquid medium, the free convective heat transfer has been demonstrated to be negligible.[31] In contrast, for micrometer-scale objects, convection should be taken into consideration. To numerically solve the 2-D temperature distribution by eqs 4-3 to 4-5, we employed COMSOL Multiphysics based on the finite element method. The temperature coefficient of the thermal conductivity of borosilicate glass substrate is negligible. However, the temperature coefficient is appreciable for CaF_2 and sapphire. Hence, we considered the temperature-dependent thermal conductivity of these substrates for the calculation.

We found that the results obtained by the numerical calculation depend on contact area, which in turn is a function of the separation between the particle and the substrate surfaces. The particles we employed in this study are regarded as spheres because the laser surface treatment was performed before the measurement. In

addition, an average surface roughness of the substrate, R_a, was 0.1 - 0.2 nm and a peak to valley roughness R_t was 1.0 nm, as determined by AFM measurements. The surface roughness of the substrates is responsible for the particle-substrate separation. Although we obtained the information on the roughness, it is still difficult to uniquely treat the boundary in the calculation. Accordingly, we calculated the heat conduction assuming three typical cases, as given pictorially in Scheme 4-2. Scheme 4-2a represents the point contact between the sphere and the smooth surface. Ideally, this model should give the best computational result. In Scheme 4-2b, the size of the contact area was assumed to be larger than that in the point contact. That is, a particle was assumed to be trapped in a pocket on the substrate surface. In this case, we moved an Au NP sphere from the point contact position to the substrate side. Scheme 4-2c represents a model for separated particle-substrate, in such a manner that a spherical Au NP sits on a spiky surface. In Scheme 4-2c, a lower thermal effect from the substrate can be predicted. We assumed that the contact area has a thermal conductivity of the medium in these calculations. The particle-substrate separation was set to 0.3 nm, which corresponds to a monolayer thickness of a solvent such as water to fill the space.[32] We used a separation smaller than 1 nm because Au NPs tend to stay at stable positions on substrates with smaller roughness. We used the same value of 0.3 nm for embedding the particle. In the following, we show first the computational result for water as a medium, which has been most commonly used.

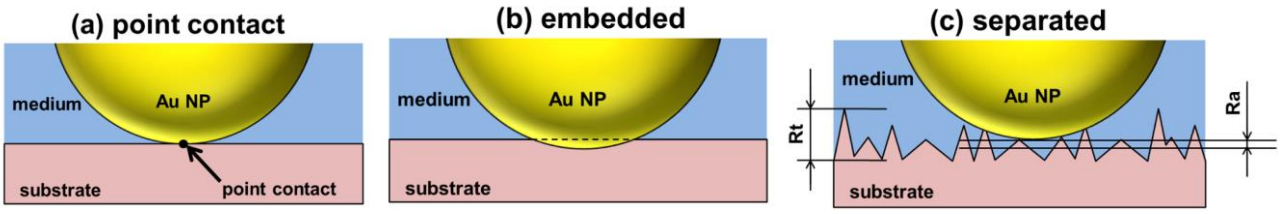

Scheme 4-2. Schematic illustrations for three types of particle surface-substrate separations: point contact, or 0 nm separation (a), partially embedded in the substrate (b), and separated (c). The Au NPs were assumed as a sphere. The surface roughness of the three substrates was determined by AFM measurements. The surface roughness of the substrates (the spiked surface filled with the medium) was assumed to be responsible for the origin of particle-substrate separations.

Figure 4-7a and b compare the 2-D temperature distributions calculated for water/glass and water/sapphire. Here, the calculation was performed under the condition where Au NP is irradiated with the laser intensity of I = 3.1 mW μm^{-2} for the water/glass case and I = 21.6 mW μm^{-2} for the water/sapphire case. We used the following parameters: thermal conductivities of medium/substrate pairs, input amount of heat: Q[W] = I [W m^2] × C_{abs} [m^2] for a particle-substrate surface separation of +0.3 nm (Scheme 4-2c). By inspecting Figure 4-7a, it has been revealed that an axisymmetric temperature distribution with a distant-dependent decrease from the particle surface was obtained in water/glass. This axisymmetric temperature distribution could be attributed to the modest disparity in the thermal conductivities of water and glass substrate. In marked contrast, in water/sapphire, the medium temperature exhibits a strong dependence on the direction from the particle center, as shown in Figure 4-7b. The medium at the lower side of a NP has appreciably lower temperatures than other areas presumably because of a considerable cooling exerted by the sapphire substrate with an appreciably higher thermal conductivity than water.

The particle temperatures calculated as a function of laser peak power densities were plotted for water/glass (Figure 4-7c) and water/sapphire (Figure 4-7d) systems. In both media, a good linear relationship was obtained for the calculated laser intensity vs particle temperature. However, a remarkable difference in the slope between water/glass and water/sapphire suggests that sapphire exhibits a great capability to cool the particle.

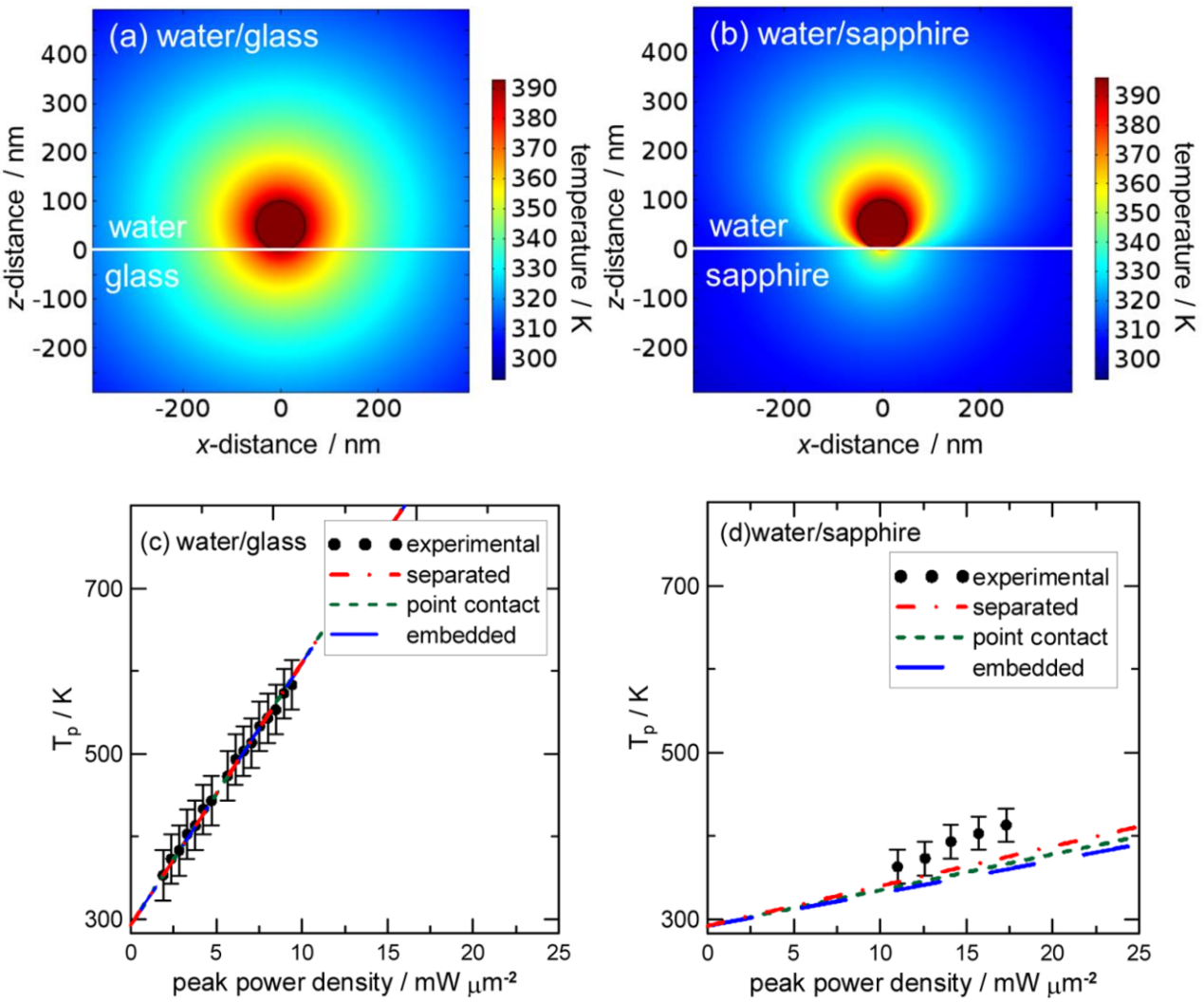

Figure 4-7. Computational 2-D temperature distributions for interfaces of water/glass, (a), and water/sapphire, (b), and the calculated T_p as a function of laser intensity, I, for interfaces of water/glass, (c), and water/sapphire, (d). In (a) and (b), an Au NP with a 100-nm diameter was assumed to be separated from the substrate surface (the separation based on AFM measurement of the substrate surface and a monolayer thickness of the medium). The temperature distribution was obtained for a particle illuminated by the laser intensity I = 3.1 mW μm^{-2} for the water/glass interface and I = 21.6 mW μm^{-2} for the water/sapphire interface. The particle temperatures are obtained to be T_p = 395 K for (a) and T_p = 395 K for (b). In (c) and (d), three separation models given in Scheme 4-2 were applied (0.3 nm for all substrates). Experimental T_p is given in (c) and (d) for comparison.

The computational slopes well reproduce the experimental ones, especially in water/glass; even for water/sapphire, the deviation in the slope is small. The three separation modes between the particle-substrate surfaces, point contact, embedded, and separated, were examined, and practically no differences were obtained by the calculation in water medium including the water/CaF_2 system (for water/CaF_2, Figure 4-8). This can be explained by the high thermal conductivity of water, allowing the heat transport to the substrate regardless of separation. The good agreement of the temperature of NPs obtained experimentally and computationally vs in water indicates the reliability of the present estimation method for substrates with various thermal conductivities. Similar result was confirmed also glycerol as shown in Figure 4-9.

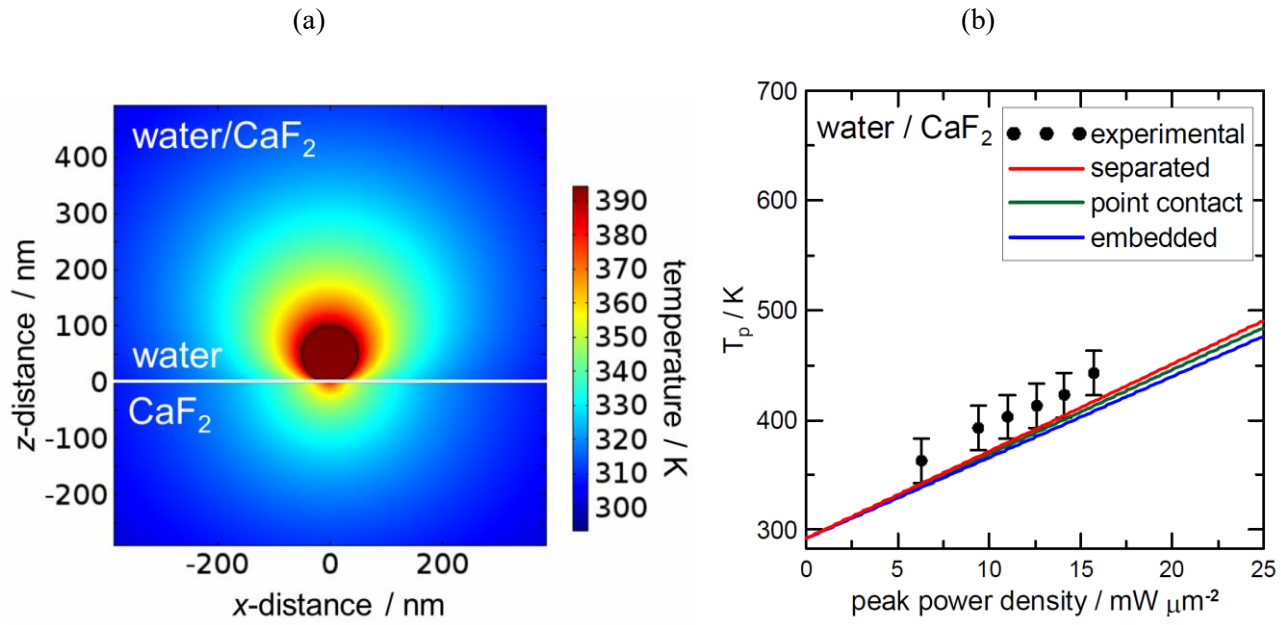

Figure 4-8. (a) 2-D temperature distribution for Au NPs with a 100-nm diameter in water/CaF_2 for the particle-substrate separation of +0.3 nm (laser power density: $I = 12.9$ mW μm^{-2}, $T_p = 395$ K). (b) Computational particle temperature as a function of laser peak power density in water/CaF_2 for three particle-substrate separation: separated (+0.3 nm), point contact (0 nm), partially embedded (-0.3 nm). For comparison, experimental data points were also shown.

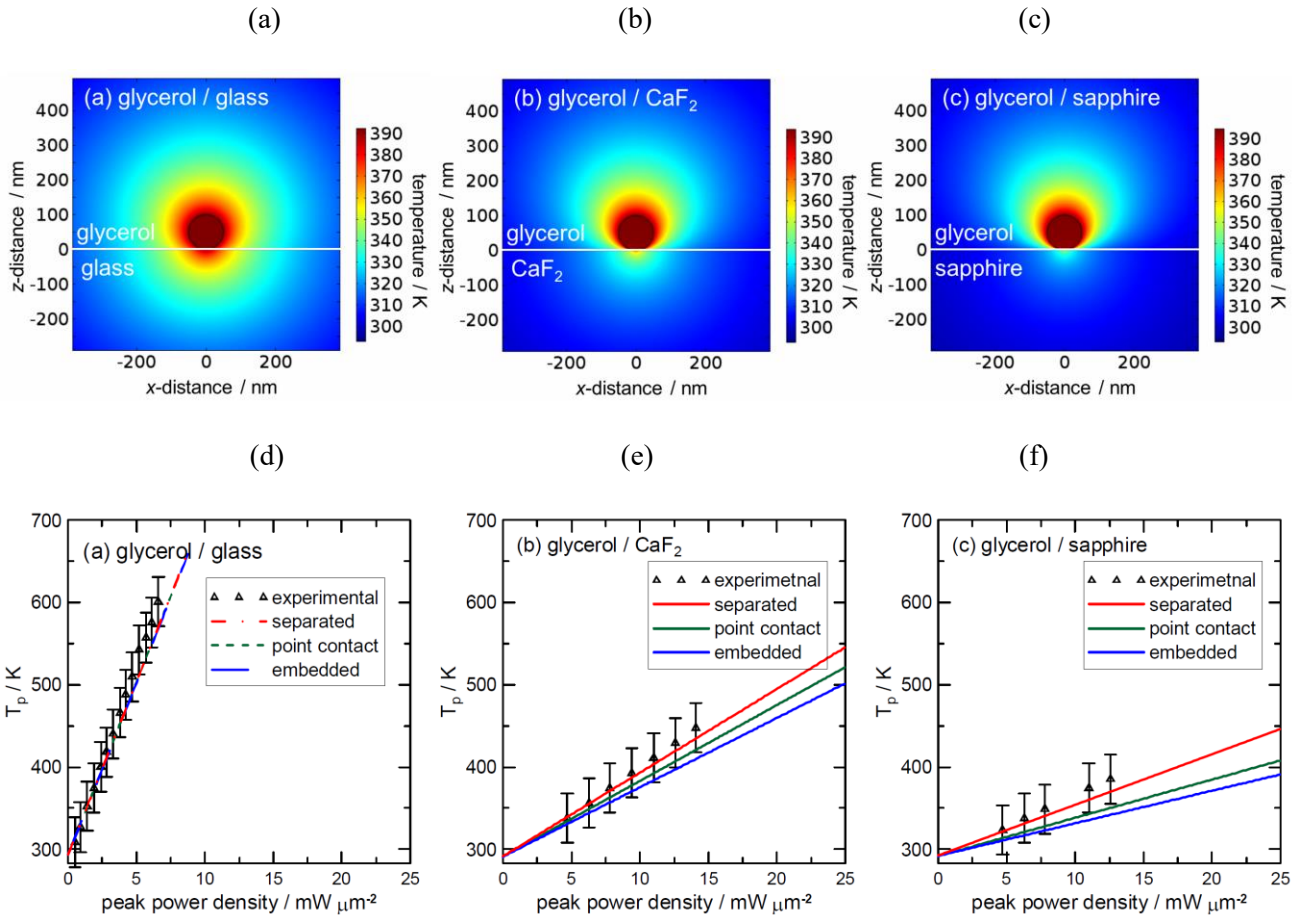

Figure 4-9. 2-D temperature distributions for systems with 0.3-nm separated Au NP (d =100 nm)-substrate surfaces: (a) glycerol/glass, I = 2.4 mW μm^{-2} (T_p = 392 K), (b) glycerol/CaF_2, I = 10.2 mW μm^{-2} (T_p = 395 K), (c) glycerol/sapphire, I = 16.6 mW μm^{-2} (T_p = 395 K). Calculated relation between the temperature of the particle and laser peak power densities in glycerol for 0.3-nm particle-substrate separations on three substrates: (a) glycerol/glass, (b) glycerol/CaF_2, (c) glycerol/sapphire.

As shown in Table 4-1, the most striking difference between k_{eff} and $\bar{k}$ (averaged values) was observed for the sapphire substrate exposed in air. To figure out this difference, we carried out the 2-D heat conduction analysis and the calculation on the relation between the laser power density and T_p, which could lead to the rational estimation of k_{eff} values. Figure 4-10 shows the 2-D temperature distributions in air/sapphire at three particle-substrate separations: point contact (0 nm separation), embedded (-0.3 nm embedded), and separated (+0.3 nm separated). For comparison, experimentally obtained relation between the laser power density and T_p is also shown. Figure 4-10a -c shows that the 2-D temperature distributions exhibit a remarkable anisotropy; the medium sides are well-heated, whereas the sides areas of the substrate are less heated because of the high thermal conductivity of sapphire. Such a non-uniform 2-D temperature distribution has been previously pointed out and attributed to the disparity in the thermal conductivities of medium/substrate systems.[33] It is worth noting that the distance between the particle and substrate strongly affect the temperature of the substrate at the interface. For instance, a small hot spot is formed in the case of contact (a, b). On the other hand, (c), the temperature of the substrate remains cool in (c) where the particle and the substrate are contact. Furthermore, the temperature increase in air is larger in the case that the particle and the substrate are separated. Thus, such a large difference was not observed in the case of water and glycerol.

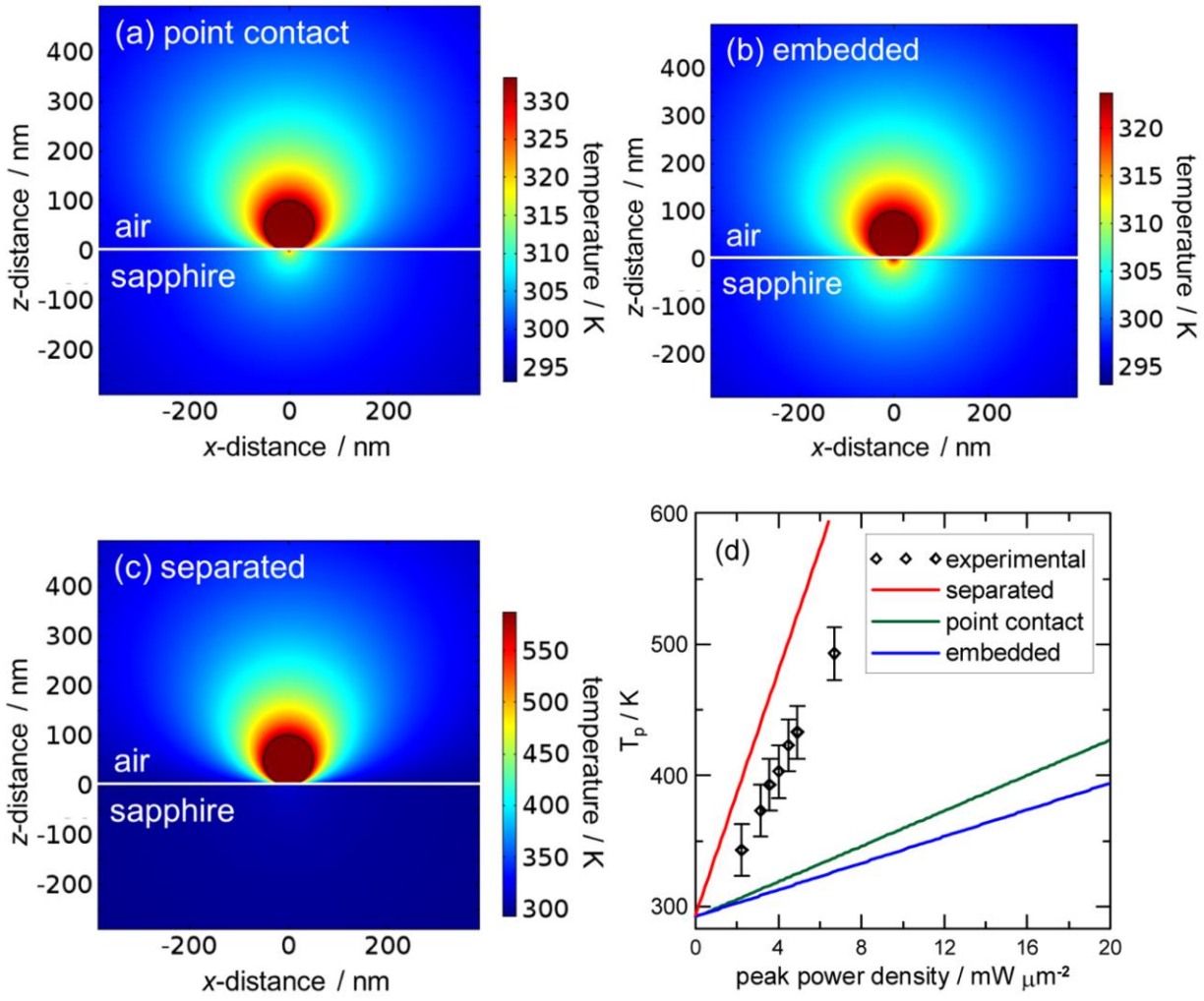

Figure 4-10. Computational 2-D temperature distributions for 100-nm diameter Au NP in air/sapphire for three particle/ substrate separations: point contact (a), 0.3 nm embedded (b), and 0.3 nm separated (c). The peak power density of 6.3 mW μm^{-2} was applied for the calculation of T_p in (a)-(c). The particle temperatures reached are 333 K (a), 324 K (b), and 587 K (c). Laser peak power density vs T_p relationship that shows the effect of particle-substrate separation on the temperature increase is given in (d).

To show more clearly the effect of the particle-substrate separation, we show the computational particle temperature as a function of laser intensity in Figure 4-10d. Whereas the temperature increases with smaller gradients for systems where particle and substrate are in contact, a remarkably greater gradient was attained with increasing distance of the particle from the substrate. This difference arises from the low thermal conductivity of the air, preventing heat conduction to the substrate. The separated model gave a better agreement with the experimental laser intensity-particle temperature relationship.

We also carried out calculations of the temperature for the air/glass and air/CaF_2 systems. Figure 4-11a and b show the laser intensity vs T_p relationships in both systems. In the case that the air is used as a surrounding medium, the particle temperatures are notably affected by the particle-substrate distance as for sapphire. Most importantly, the separated model gave a better agreement with the experimental results, although not exactly the same. All the calculated results presented above suggest that the Au NPs locates on the surface indented in the subnanometer scale, inhibiting the close contact of Au NPs to the surface of the substrate and, as a result, interfering with the heat conduction through the substrate in the air environment. However, when we use water and glycerol as medium, this interface effect is minimal.

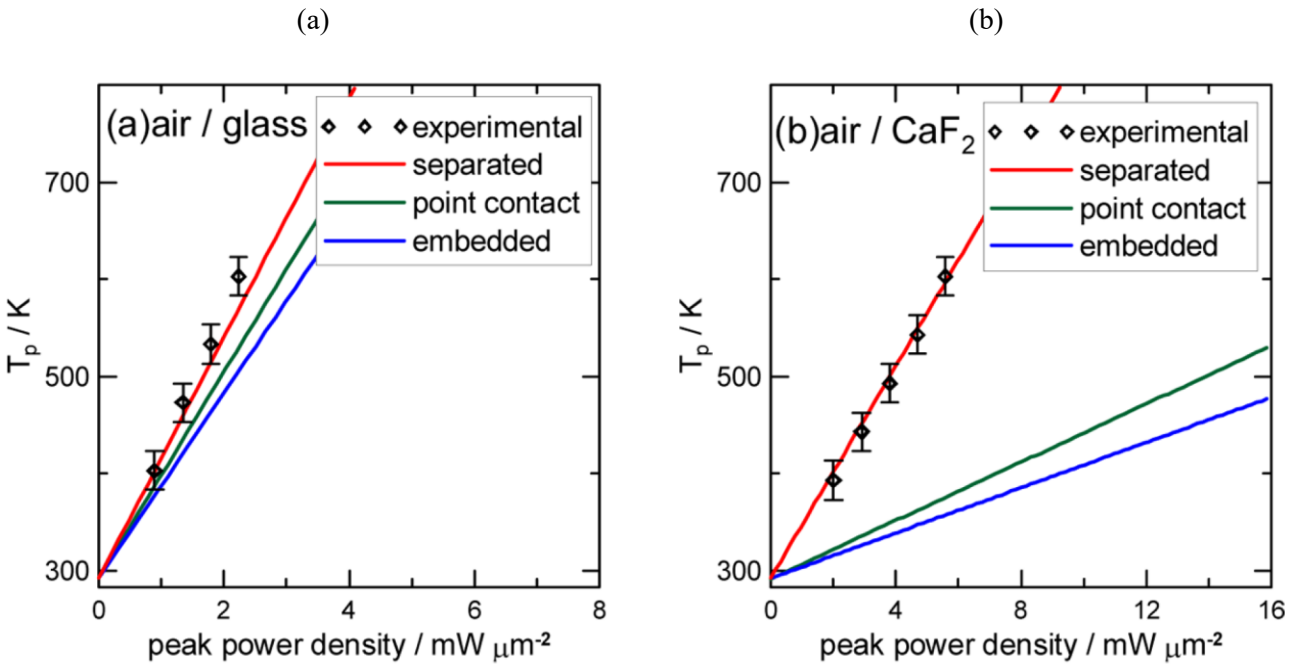

Figure 4-11. The temperature of particles calculated as a function of laser peak power density for Au NP with a 100-nm diameter in air/glass with various particle-substrate separations: point contact, 0.3 nm embedded, and 0.3nmseparated (a), and air/CaF_2 at different particle-substrate separations: point contact, 0.3 nm embedded, and 0.3 nm separated (b). For comparison, experimental laser intensity vs T_p relationships are given.

Experimental and Computational k_{eff} Values. In the previous section, we obtained k_{eff} from the gradients of the computed relation between the laser intensity and T_p. The In Table 4-1, we listed the calculated results and plotted graphically in Figure 4-12, as a function of the thermal conductivity of the substrate, k_{sub}. Note that the k_{eff} values were obtained for the model where Au NPs are supported on rough surfaces (they are separated from the surface by 0.3 nm).

As mentioned in the introductory part of this chapter, a proper treatment of the effective thermal conductivity has not been reported for the supported systems.[9,13,34] Although the averaged thermal conductivity, $\bar{k}$, for the two-component system can be a good approximation for the system with the small disparity of thermal conductivities between the medium and substrate, such as for water and glass,[9,13] this averaged one as eq 4-2 is inadequate for the system with large disparity. To find systems properly treated by $\bar{k}$, we calculated the 2-D temperature distributions and the relation between the laser peak power density and T_p for Au NPs with a100-nm diameter embedded in the substrate of glass, CaF_2, and sapphire in the three kinds of the surrounding medium (Figure 4-13). Despite the large disparity between k_{sub} and k_{med} in the air/sapphire system, we obtained axisymmetric temperature distributions similar to a homogeneous medium. More importantly, the calculated k_{eff} vs k_{sub} curves are linear and the slope is more or less similar to that of $\bar{k}$ vs k_{sub} curves regardless of k_{med} (Figure 4-14). This result suggests that $\bar{k}$ should be used for the system in which a particle is half-embedded, not for a particle that is supported on a substrate.

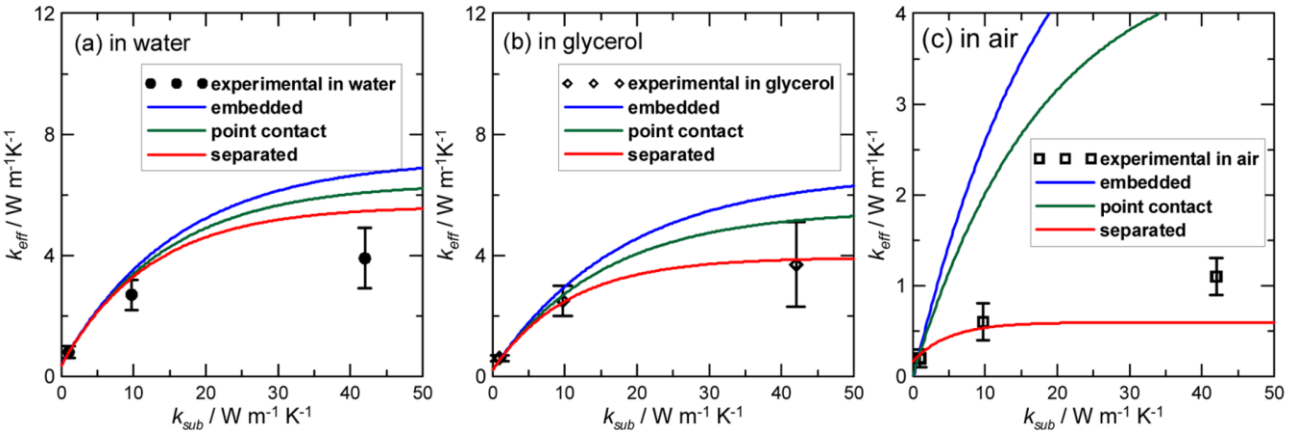

Figure 4-12. Experimental and computational k_{eff} vs k_{sub} curves for various substrates in three media: water (a), glycerol (b), and air (c).

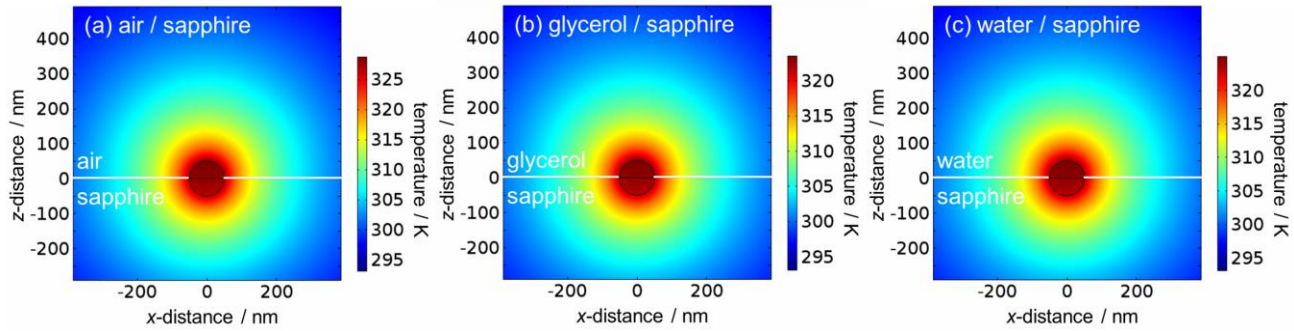

Figure 4-13. Calculated 2-D temperature distributions for Au NPs with a 100-nm diameter, half-embedded in sapphire substrate and exposed to air, glycerol and water, at the irradiation laser intensity of I = 28.2 mW μm^{-2}; (a) air/sapphire, (b) glycerol/sapphire, and (c) water/sapphire. Particle temperatures are (a) 361 K, (b) 350 K and (c) 353 K. Remarkably, concentric temperature distributions were obtained in all cases regardless of a large disparity in the thermal conductivities of the substrate and the medium. In the calculation, temperature-dependent thermal conductivities of substrates were not considered.

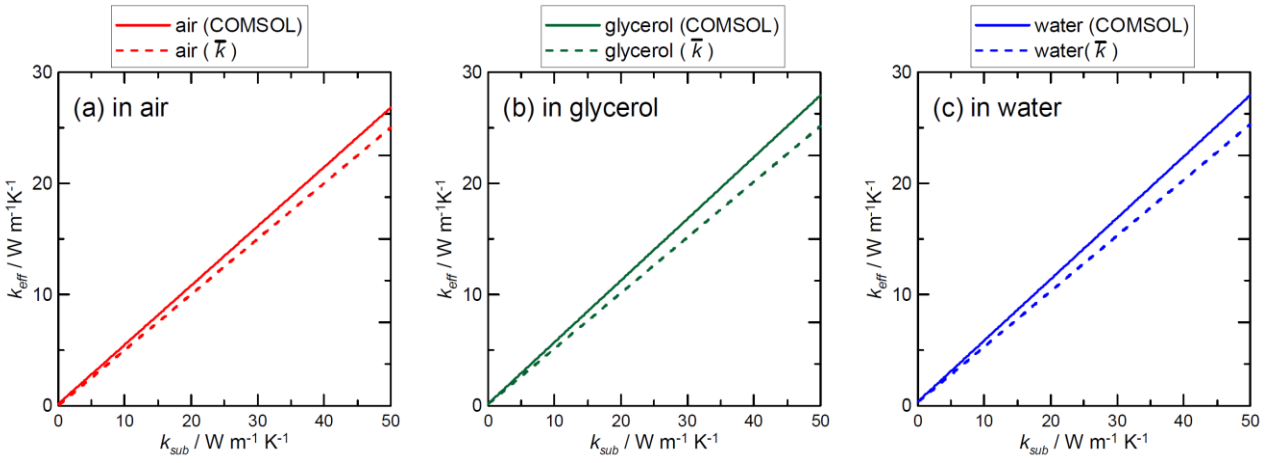

Figure 4-14. Calculated k_{eff} as a function of k_{sub} for Au NPs with a 100-nm diameter, half-embedded in sapphire substrate exposed to air (a), glycerol (b) and water (c). Calculated k using eq 4-1 and 4-2 as a function of k_{sub} is also shown for comparison. A fairly good agreement between k_{eff} and $\overline{k}$ are obtained in all the cases. In the calculation, temperature-dependent thermal conductivities of substrates were not considered.

The concept of k_{eff} obtained in the present study is best represented as a thermal conductivity experienced by the Au NP itself, even though it is supported on a substrate in a medium (a complex environment). This is because the particle temperature is always uniform throughout the entire particle. The experimentally determined k_{eff} is meaningful for the particle, although this does not represent the actual inhomogeneous temperature distributions of the substrate/medium system outside the particle. Using this k_{eff} for a given laser intensity, we can determine the steady-state particle temperature that is useful in various experiments including surface-enhanced Raman spectroscopy and photothermal therapy.

4-4. CONCLUSION

We measured the temperature of single gold NPs with a 100-nm diameter under the laser irradiation supported on three substrates in three different media. It was revealed that the temperature of the particle increases linearly with increasing laser intensity strongly depending on both medium and substrate. The relation experimentally obtained for the temperature and laser intensity was analyzed by the 1-D heat transfer model and effective thermal conductivities (k_{eff}) for the nine substrate-medium pairs were deduced. The numerical calculations solving the 2-D heat conduction equations well reproduced the k_{eff} values observed experimentally. The computational study also revealed that a conventional $\bar{k}$, which was obtained as the average of thermal conductivities of the two component values, could serve as a good approximation for the particle half-embedded in the substrate and half-exposed to the medium. In other word, $\bar{k}$ is not appropriate for a particle supported on a substrate. For precise representation of nanoscale heat transfer, we applied the 2-D heat transfer analysis, which revealed anisotropic temperature distributions. Nevertheless, the usefulness of the experimentally obtained k_{eff} values should not be underestimated, because k_{eff} can provide particle temperatures for a given excitation laser power regardless of the complexity of the system. The present investigation revealed that not only the substrate but also the medium play crucial roles in the nanoscale steady-state heating involving heat dissipation. A substrate in conjunction with the surrounding media can control particle temperature. This information could provide rational principles for the application of photothermal processes with precise control of particle temperature under remote laser heating.

REFERENCES

(1). Qin, Z.; Bischof, J. C. *Chem. Soc. Rev.* **2012**, 41, 1191–1217.

(2). Govorov, A. O.; Richardson, H. H. *Nano Today* **2007**, 2,30–38.

(3). Baffou, G.; Quidant, R. *Laser Photonics Rev.* **2013**, 7, 171–187.

(4). Dreaden, E. C.; Mackey, M. A.; Huang, X.; Kang, B.; El-Sayed, M. A. *Chem. Soc. Rev.* **2011**, 40, 3391–3404.

(5). Dreaden, E. C.; Alkilany, A. M.; Huang, X.; Murphy, C. J.; El- Sayed, M. A. *Chem. Soc. Rev.* **2012**, 41, 2740–2779.

(6). Plech, A.; Leiderer, P.; Boneberg, J. *Laser Photonics Rev.* **2009**, 3, 435–451.

(7). Hashimoto, S.; Werner, D.; Uwada, T. *J. Photochem. Photobiol. C* **2012**, 13,28–54.

(8). Zijlstra, P.; Orrit, M. *Rep. Prog. Phys.* **2011**, 74, 106401.

(9). Hühn, D.; Govorov, A.; Gil, P. R.; Parak, W. J. *Adv. Funct. Mater.* **2012**, 22, 294–303.

(10). Baffou, G.; Savatier, J.; Polleux, J.; Zhu, M.; Merlin, M.; Ringneault, H.; Monneret, S. *ACS Nano* **2012**, 6, 2452–2458.

(11). Fedoruk, M.; Lutich, A. A.; Feldmann, J. *ACS Nano* **2011**, 5, 7377–7382.

(12). Skirtach, A. G.; Kurth, D. G.; Mohwald, H. *Appl. Phys. Lett.* **2009**, 94, 093106.

(13). Carlson, M. T.; Khan, A.; Richardson, H. H. *Nano Lett.* **2011**, 11, 1061–1069.

(14). Honda, M.; Saito, Y.; Smith, N. I.; Fujita, K.; Kawata, S. *Opt. Express* **2011**, 19, 12375–12383.

(15). Bendix, P. M.; Reihani, S. N. S.; Oddershede, L. B. *ACS Nano* **2010**, 4, 2256–2262

(16). Setoura, K.; Werner, D.; Hashimoto, S. *J. Phys. Chem. C* **2012**, 116, 15458–15466.

(17). Keblinski, P.; Cahill, D. G.; Bodapati, A.; Sullivan, C. R.; Taton, T. A. *J. Appl. Phys.* **2006**, 100, 054305.

(18). Link, S.; El-Sayed, M. A. *J. Phys. Chem. B* **1999**, 103, 4212–4217.

(19). Liz-Marzan, L. M.; Mulvaney, P. *New J. Chem.* **1998**, 22, 1285–1288.

(20). Sumner, A. L.; Menke, E. J.; Dubowski, Y.; Newberg, J. T.; Penner, R. M.; Hemminger, J. C.; Wiegen, L. M.; Brauers, T.; Finlayson-Pitts, B. J. *Phys. Chem. Chem. Phys.* **2004**, 6, 604–613.

(21). Tanabe, T.; Tatsuma, T. *Nano Lett*. **2012**, 12, 5418–5421.

(22). Mie, G. *Ann. Phys*. **1908**, 25, 377–445.

(23). Bohren, C. F.; Huffman, D. R. *Absorption and Scattering of Light by Small Particles*; Wiley: New York, **1983**.

(24). Otter, M. *Z. Phys*. **1961**, 161, 539–549.

(25). Baffou, G.; Quidant, R.; Javier, F.; Garcia de Abajo, F. J. *ACS Nano* **2010**, 4, 709–716.

(26). Wilson, O. M.; Hu, X.; Cahill, D. G.; Braun, P. V. *Phys. Rev. B* **2002**, 66, 224301.

(26). Juvé, V.; Scardamaglia, M.; Maioli, P.; Crut, A.; Merabia, S.; Joly, L.; Fatti, N. D.; Vallée, F. *Phys. Rev.* B **2009**, 80, 195406.

(28). Merabia, S.; Shenogin, S.; Joly, L.; Keblinski,P.; Barrat, J.-L. *Proc. Natl. Acad. Sci. U.S.A.* **2009**, 106, 15113–15118.

(29). Baffou, G.; Rigneault, H. *Phys. Rev. B* **2011**, 84, 035415.

(30). Siems, A.; Weber, S. A. L.; Boneburg, J.; Plech, A. *New J. Phys*. **2011**, 13, 043018.

(31). Donner, J. S.; Baffou,G.; McCloskey, D.; Quidant, R. *ACS Nano* **2011**, 5, 5457–5462.

(32). Opitz, A.; Scherge, M.; Ahmed, S. I.-U.; Schaefer, J. A. A *J. Appl. Phys.* **2007**, 101, 064310.

(33). Baffou, G.; Quidant, R.; Girard, C. *Phys. Rev. B* **2010**, 82, 165424.

(34). Yamauchi, H.; Ito, S.; Yoshida, K.; Itoh, T.; Tsuboi, Y.; Kitamura, N.; Miyasaka, H. *J. Phys. Chem. C* **2013**, 117, 8388–8396.

(35). Mock, J. J.; Barbic, M.; Smith, D. R.; Schultz, D. A.; Schultz, S. *J. Chem. Phys.* **2002**, 116, 6755–6759.

(36). Sonnichsen, C.; Franzl, T.; Wilk, T.; von Plessen, G.; Feldmann, J.; Wilson, O.; Mulvaney, P. *Phys. Rev. Lett.* **2002**, 88, 077402.

(37). Itoh, T.; Uwada, T.; Asahi, T.; Ozaki, Y.; Masuhara, H. *Can. J. Anal. Sci. Spectrosc.* **2007**, 52, 130–141.

5. Stationary Bubble Formation and Marangoni Convection Induced by CW Laser Heating of a Single Gold Nanoparticle

ABSTRACT

As stated in previous chapters, gold nanoparticles (Au NPs) efficiently convert incident light into heat under the resonant condition of localized surface plasmon. Controlling mass transfer through plasmonic heating of Au NPs has potential applications such as manipulation and fabrication within a small space. Here, we describe the formation of stationary microbubbles and subsequent fluid convection induced by CW laser heating of Au NPs in water. Stationary bubbles about 1 – 20 μm in diameter were produced by irradiating individual Au NPs with a CW laser. Spatial profiles and velocity distribution of fluid convection around the microbubbles were visualized by wide-field fluorescence imaging of tracer nanospheres. To evaluate the bubble-induced convection, numerical simulations were performed on the basis of general heat diffusion and Navier-Stokes equations. A comparison between experimental and computational results revealed that a temperature derivative of surface tension at the bubble surface is a key factor to control the fluid convection. Temperature differences of a few Kelvin at the bubble surface resulted in convective velocities ranging from 10^2 to 10^3 μm s^{-1}. The convective velocity gradually saturated with increasing bubble diameter. This result covers both natural and Marangoni convection induced by plasmonic heating of Au NPs.

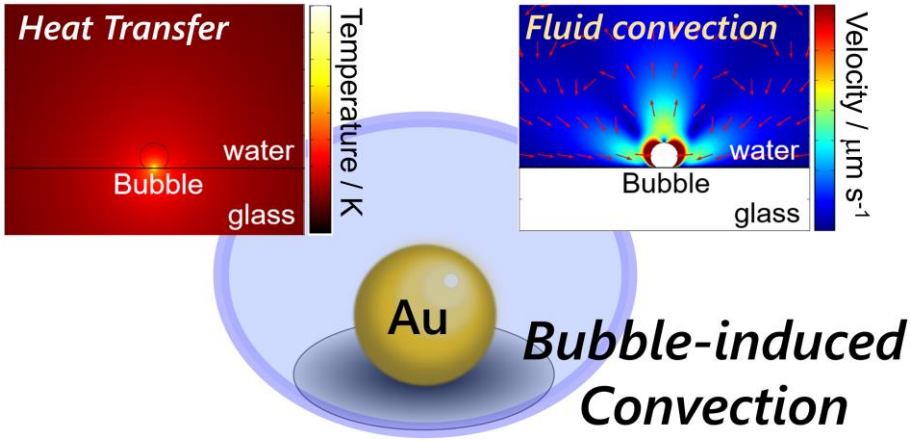

5-1. INTRODUCTION

As have already mentioned in previous chapters, noble metal nanoparticles (NPs) have been attracting much attention in the field of photoscience from various viewpoints. One of the characteristic features of noble metal NPs is the localization and enhancement of optical fields arising from Localized Surface Plasmon Resonance (LSPR)[1–3]. Photoexcitation of LSPR band promotes 10^6-fold enhancement of incident electric field in near-field regime. This field enhancement effect has been widely utilized as nanoscale optical antennas for photochemical reactions[4,5] and surface enhanced spectroscopy[6,7]. Another feature of noble metal NPs is their effective photothermal conversion efficiency. The photo-energy absorbed by NPs turns into heat via electron-phonon coupling within a few picosecond after the photoexcitation[8,9]. This rapid photothermal conversion is of great use as nanoscale heat sources. Among various noble metals, gold nanoparticles (Au NPs) are utilized as ideal local heaters because of their physicochemical stability and high conversion efficiency[10]. Elevation in local temperature through plasmonic heating of Au NPs leads to potential applications such as photothermal cancer therapy[11], photothermal imaging[12,13], and nanofabrication[14,15].

Because photoresponses including the surrounding medium of NPs is strongly dependent on the temperature of NPs, excitation light intensity is an important factor in the application of the photothermal effect. Temperature of Au NPs under laser illumination with 10^5- 10^7 W cm^{-2} is more than 10^3 K, leading to melting of NPs and/or evaporation of surrounding matrices. By irradiating Au NPs inside a tumor with pulsed lasers[16,17], Lukianova-Hleb *et al.* applied transient vapor bubbles generated via the evaporation of the medium surrounding NPs to the cancer therapy and drug delivery. Dynamics and mechanism of the bubble formation around heated NPs have been also investigated by means of the time-resolved X-ray scattering[18] and transient absorption spectroscopy[19,20]. These studies revealed that transient vapor bubbles in aqueous medium was produced by the spinodal decomposition of surrounding water adjacent NPs surface at temperatures around 550 K[18,19,21,22] and the lifetime was in a few tens of nanoseconds, depending on the pulse width and excitation intensities.

Not only the pulsed excitation but also the CW laser irradiation can lead to the formation of bubbles[23,24] in the

stationary state[25,26] around Au NPs in water. This stationary bubble can induce thermal convections of fluid around the focal spot of a laser beam (Scheme 5-1), which has emerged as a method to control the motion of fluid in microscopic region[27]. In general, thermal convection of fluid can be classified into two cases: natural convection and Marangoni convection. The former natural convection arises from buoyancy force generated by the density difference of liquid in the temperature gradient. Under the CW laser irradiation of a single Au NP in water, the convective velocity of the natural convection is ca. 10 nm s^{-1} around the single NP[28] and, at most, 1.0 μm s^{-1} in a dense array consisting of Au nanostructures[29]. Accordingly, the natural convection has small contribution for micro-manipulation or micro-fabrication. On the other hand, the latter Marangoni convection, originating from the surface tension of stationary bubbles, has much higher convective velocities[30,31] such as 1000 μm s^{-1}. By utilizing the Marangoni convection through plasmonic heating of Au NPs, several applications such as controlling fluid flow in microfluidic channels[30], assembling of colloidal nanoparticles[31–34], size selection of polystyrene beads[35], and crystallization of glycine[36] have been demonstrated.

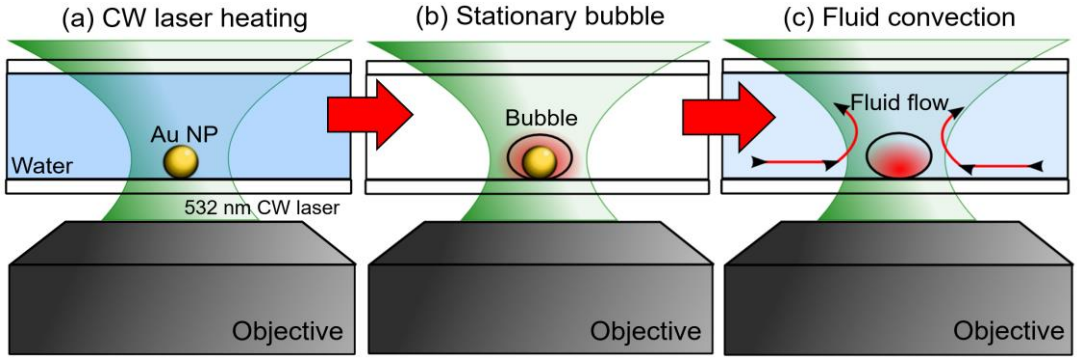

Scheme 5-1. Schematic illustrations of time evolution of an Au NP supported on a substrate under CW laser illumination.

For advanced applications of the local heating, basic physical features of the Marangoni convection are of crucially importance. Along this line in the present work, we have investigated the formation of stationary microbubbles and subsequent fluid convection induced by CW laser heating of individual Au NPs in water by employing experimental methods and numerical simulation. Fluid convection around the stationary bubble was experimentally visualized by wide-field fluorescence imaging of polystyrene nanoparticles (FL-beads) as tracers, of which results were analyzed by numerical simulations of thermal convection on the basis of general heat diffusion and Navier-Stokes equation. By integrating the present results with our previous works on the thermometry of single NPs (Chapter 2 and 4)[37] and aggregates consisting of Au NPs[38], and bubble formation in water triggered by CW and pulsed laser irradiation (Chapter 2 and 3)[19,39], we have presented a model of photothermal convection by including all the components such as a single Au NP, the bubble, water, and a glass substrate.

5-2. MATERIALS and METHODS

Sample Preparation. The specimen was prepared in the following manner. Aqueous suspension of Au NPs with nominal diameters of 150 nm (EMGC 150, British Biocell International) were used as received. Glass coverslips (24 × 32 × 0.17 mm, Matsunami) were put into acetone in a small vessel and sonicated for 30 min, followed by immersion in 5 wt % aqueous solution of sodium hydrate for 30 min to purify the surface. After rinsing them with ultrapure water, the coverslips were dried with a nitrogen gun. Then Au NPs were spin-coated onto the well-cleaned coverslips. The Au NPs-coated coverslips were washed three times with ultrapure water on the spin coater. In addition to this sample preparation, Au NPs were submerged in medium, in a 120-μL chamber consisting of two coverslips and a 0.3-mm thick silicone rubber spacer. To observe the formation of stationary bubbles, ultrapure water was used as a surrounding medium. For visualization of fluid convection, a 0.05 wt % aqueous colloidal solution of dyes-loaded polystyrene nanospheres (F8795, 40-nm diameter, Molecular Probes) was employed as tracer nanospheres.

Optical Measurements. The specimen of coverslips was mounted on an *x*-*y* scanning stage (BIOS-150T, Sigma) of an inverted optical microscope (IX-70, Olympus). A schematic illustration of an optical setup is shown in Figure 5-1. Scattering images of individual Au NPs and stationary bubbles were obtained using a dark-field condenser (U-DCD (NA = 0.8 – 0.92), Olympus) and transmission imaging was performed with a bright-field condenser (IX-LWUCD, Olympus). Monochromatic CCD (Infinity 3-1 URM, Lumenera,) was used for both bright- and dark-field imaging. Transmission and scattering images of individual Au NPs are shown in Fig. 5-1. To characterize the optical properties of Au NPs, the forward light scattering spectra were measured by a fiber-coupled spectrometer (SD-2000, Ocean Optics). For all optical imaging, micro-spectroscopy, and laser illumination, a microscope objective (UPlanFl, 40× NA = 0.75, Olympus) was used. The excitation of a single Au NP was performed using a tightly-focused 532 nm CW DPSS laser (Exelsior 532, Spectra Physics). The spot size of the 532 nm laser light was estimated to be 0.9 μm in diameter (FWHM), by measuring the fluorescence intensity distribution of a thin amorphous film of fluorescent dyes on a well-cleaned coverslip under photoexcitation. To visualize the fluid convection by wide-field fluorescence imaging, a 488 nm CW laser (Exelsior 488, Spectra Physics) was employed as an excitation light source. The 488 nm CW laser was coaxially introduced into the optical path of the focused 532 nm CW laser. Irradiation of the two CW lasers was performed with mechanical shutters for each laser. For the wide-field fluorescence imaging, the laser power was set to 2.0 mW at the backport of the optical microscope. While monitoring the fluid convection by tracing the fluorescent polystyrene nanospheres (FL-beads), scattered laser light from the sample volume was blocked with a long-pass filter (BLP01-532R-25, Semrock). A time interval in fluorescence imaging was 36 ms: 6 ms for exposure time and 30 ms for data acquisition. The laser power was measured using a photodiode power meter (S120UV & PM100, Thorlabs).

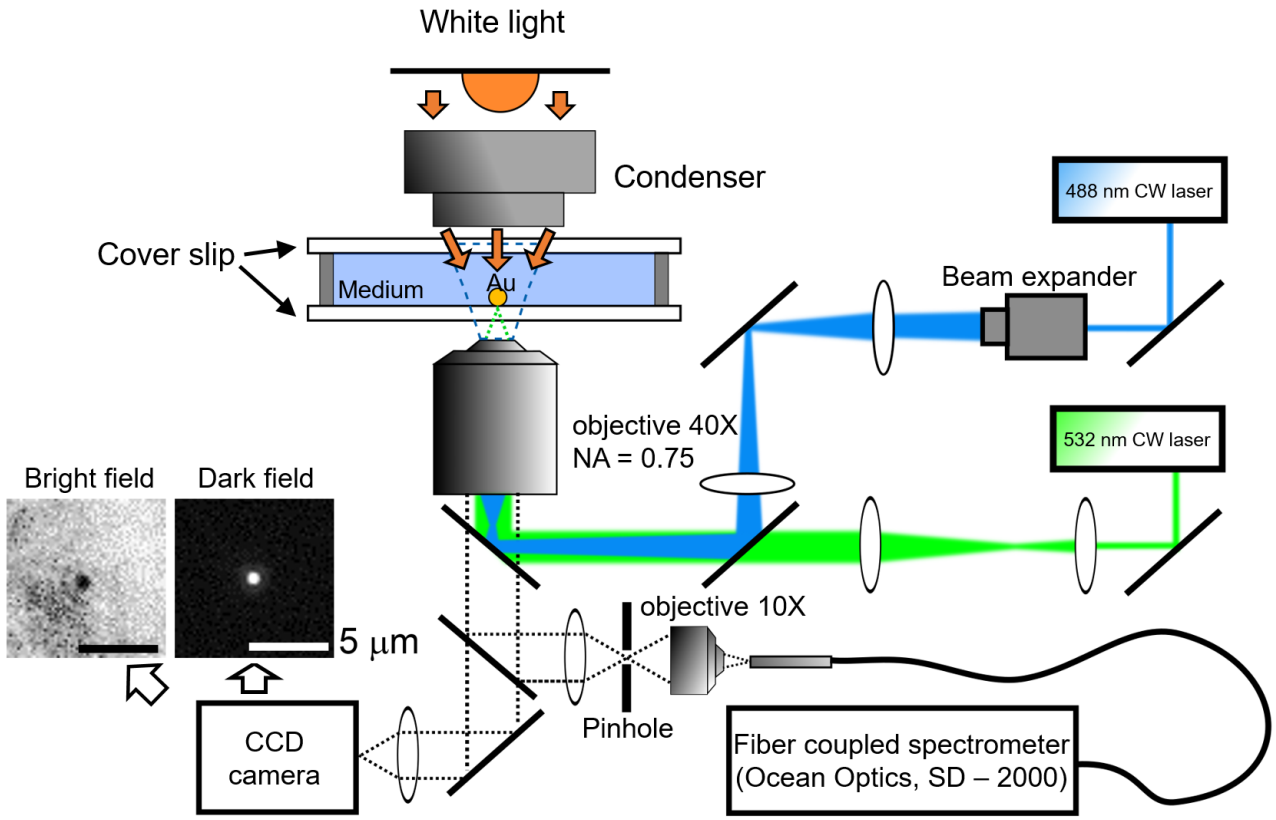

Figure 5-1. Experimental setup.

5-3. RESULTS and DISCUSSION

Formation of stationary bubbles under the CW laser heating.

First, we examined the stationary bubble formation induced by CW laser heating of a single Au NP with a diameter of 150 nm. Figure 5-2a shows the transmission image of a single Au NP without laser irradiation. The single Au NP with 150-nmdiameter was observed as a diffraction-limited point with a diameter of 0.6 μm at the center of the image corresponding to the irradiation spot. As shown in Figure 5-2b, c and d, under the CW laser irradiation at 532 nm, images larger than the diffraction limited size can be clearly observed with Airy diffraction patterns. Because the appearance of the Airy diffraction pattern is due to the disparity in refractive indices arising from the formation of a domain with a refractive index smaller than that of the surrounding water, these images show the generation of bubbles under this irradiation condition. These images were almost unchanged during the laser irradiation, indicating that the bubble is in a stationary state and the expansion was much faster than the time resolution in the present transmission and wide-field fluorescence imaging (typically a few tens of ms). From a heat conduction equation, temperature of a single NP can be estimated to reach a steady-state within a few μs under the CW laser illumination[40]. Actually, it was revealed, by means of time-resolved photothermal microscopy for a single Au NP, that the time scale on the expansion of vapor nanobubbles produced by CW laser heating was less than a few μs[41]. After stopping the irradiation, the bubble gradually decreased its size by transferring the gas molecules into the liquid phase[26] and disappeared within several seconds. It is worth mentioning the stability of the bubble under the CW laser irradiation. It has been reported that nanobubbles smaller than 200 nm in diameter produced by CW laser heating of a single Au NP repeat the periodic generation and contraction every ca. 500 ns.[41] This behavior, however, is observed only in the limited experimental conditions. For the system with n-pentane ($T_{boiling}$: 309 K at atmospheric pressure) as a surrounding medium, this oscillating behavior was observed only in the case where the excitation intensity was just above the threshold of the bubble formation (*e.g.* 100 μW). Under the excitation condition with the intensity higher than the threshold, the stationary bubble was confirmed under CW laser illumination[41], as reported by many researchers[23,24,26]. The excitation condition in the present work is much higher

than the threshold of the bubble formation and thus we can safely conclude that the microbubbles observed by diffraction-limited optical imaging, shown in Figure 5-2, are in a steady-state under CW laser illumination.

Figure 5-2e shows excitation intensity dependence of the bubble diameter that was defined as the circumference of the middle dark circle as shown in Figure 5-2c. The diameter, which were averaged over 5-7 measurements, monotonically increases with an increase in the excitation power. Small deviations in the measurements at the same excitation power indicate good controllability of bubble diameter through CW laser heating of a single Au NP. Formation of bubbles was not observed at low excitation intensities < 10 mW μm^{-2} by optical transmission imaging. This might be due to the detection limit in the transmission image. For the evaluation of nanobubbles smaller than the diffraction limit, the dark-field imaging and light-scattering spectroscopy have been reported to be powerful tools[24]. Actually, we have conducted same experiment under dark-field illumination, and obtained results similar to those shown in Figure 5-2e (See Figure 5-3). As will be discussed later, however, it is rather difficult to measure the fluid convection around the stationary bubble with a diameter < 1 μm. Hence, we concentrate our discussion on the bubble observed at photoexcitation intensities ≥ 10 mW μm^{-2}.

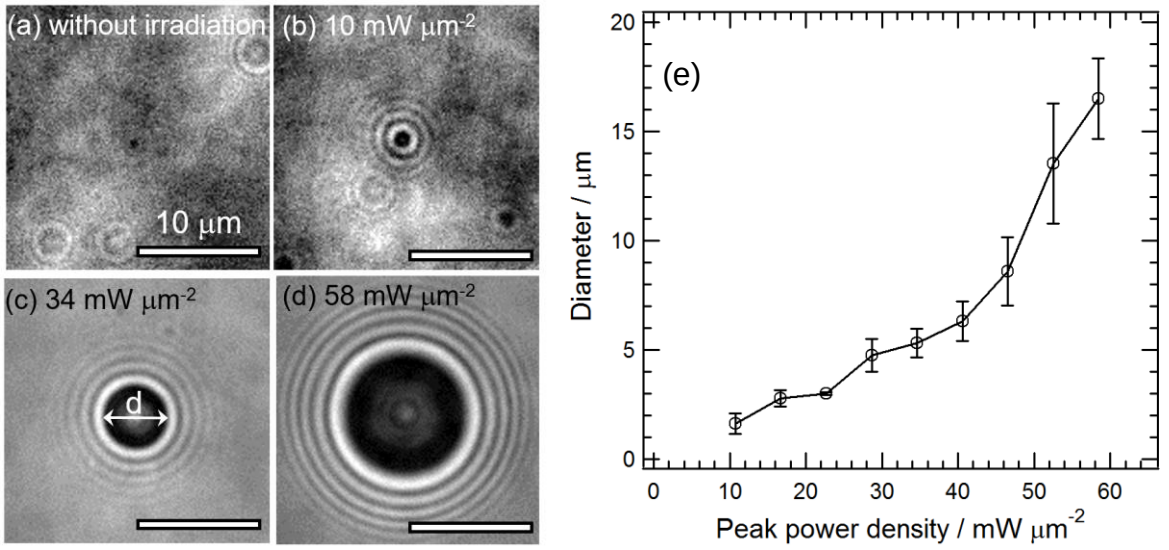

Figure 5-2. (a-d) Optical transmission images of the bubble formation at the laser powers of 0, 10, 34, and 58 mW μm^{-2}. (e) The bubble diameter as a function of laser peak power density.

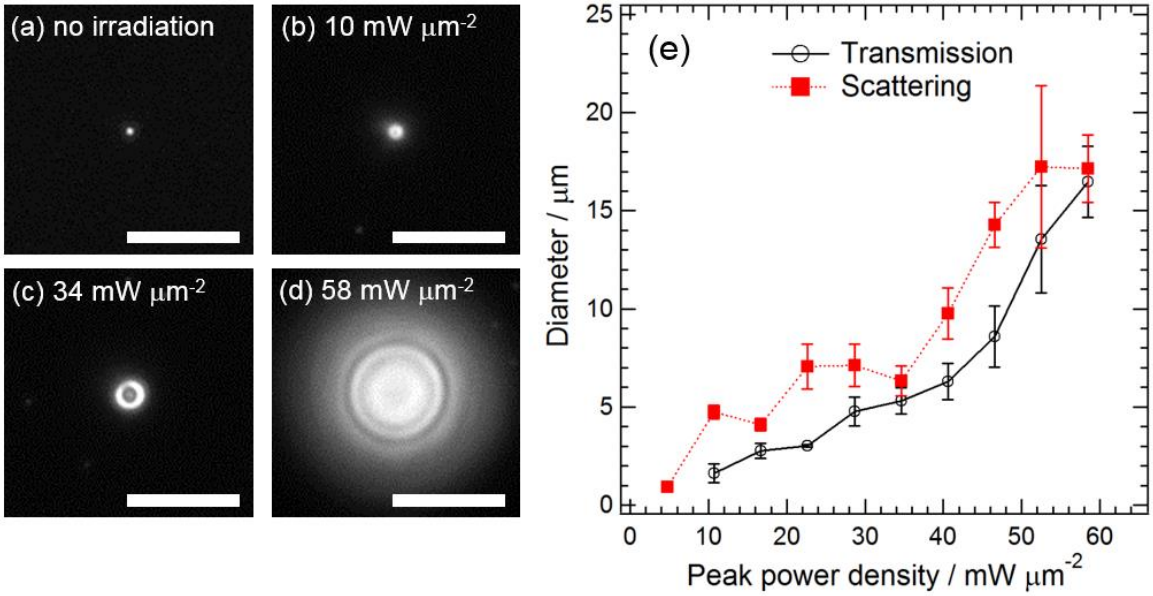

Figure 5-3. (a-d) Optical scattering images of the bubble formation at the laser peak power densities of 0, 10, 34, and 58 mW μm^{-2} (scale bar: 10 μm). (e) The bubble diameter as a function of laser peak power density.

Analysis of the condition for the stationary bubble formation.

The bubble in the stationary state is based on the balance between the energy input by continuous photoabsorption of the Au NP and the release of heat from the inside to the outside of the bubble. Quantitative analyses of the stationary state could provide various physical parameters around the Au NP and the surrounding water. In actuality, these analyses were reported for micrometer-sized aggregates[23], thin films[31,32] and periodic arrays consisting of Au NPs[26]. Although these reports have yielded various parameters, rather complex structures of local heaters needed several assumptions on the surface temperature of the bubble[31], structure of the heat source and the boundary condition[26]. On the other hand, present system of a single isolated spherical Au NP could serve as one of ideal systems of the heat source, which could lead to better elucidation on the total amount of generated heat in the bubble and the temperature gradient at bubble surface.

Figure 5-4a shows the schematic representation of the calculation, which is based on the 1D heat conduction model consisting of a spherical NP immersed in a homogeneous medium. Under the actual experimental condition, however, surrounding environment of Au NPs consists of a glass substrate and water. To take into account the disparity in thermal conductivities between the two different media, we employed the effective thermal conductivity that has been devised for steady-state optical heating of a single Au NP supported on a dielectric substrate and immersed in medium[37,42]. Accordingly, the local temperature increase around a single Au NP is given by[10,37,40],

$$T(r) = \frac{C_{abs}\, I}{4\pi\, k_{eff}\, r} + T_{\infty} \quad (r = a) \qquad (5\text{-}1)$$

where C_{abs} [m^2] is the absorption cross section of an Au NP at excitation wavelength, I [W m^{-2}] peak power density, r [m] radial distance from NP center, a [m] nanoparticle radius, k_{eff} [W m^{-1}K^{-1}] effective thermal conductivity, and T_{∞} [K] ambient temperature. The peak power density I (mW μm^{-2}) is represented by I = (P_{laser} (2.3546)^2) / 2π(fwhm)^2, where P_{laser} [mW] is the laser power, and fwhm [μm] the laser beam diameter assuming a Gaussian beam profile. We used the effective thermal conductivity, k_{eff} of 0.8 [W m^{-1}K^{-1}], which value was reported[37,42] for

the surrounding environment consisting of a glass substrate (k_{glass} = 1.0 [W m^{-1}K^{-1}]) and a water medium (k_{water} = 0.6 [W m^{-1}K^{-1}]). Effective refractive index (n_{eff}) of the surrounding medium was employed to calculate C_{abs} from the Mie theory. Because of the temperature continuity at the interface between NP and medium under steady-state conditions, the temperature of NP (T_{NP}) can be obtained at the boundary where r equals to the radius of NP[43]. For pulsed laser hearing of Au NPs, it is known that there is a huge temperature gap at gold-water interface[44]. This discontinuity in temperature arises from the thermal boundary conductance at the surface. However, this parameter plays no role in steady-state regime[45]. Hence, eq 5-1 is applicable to the calculation of the temperature of a single NP under the CW laser illumination. Temperature from the surface of NP to the surrounding medium was assumed to be inversely in proportion with r as shown in Figure 5-4a, while it was assumed that the temperature in the NP was uniform due to the high thermal conductivity of gold (k_{gold} = 314 W m^{-1}K^{-1}). On the basis of this model with these parameters, we calculated the dependence of T_{NP} on peak power density.

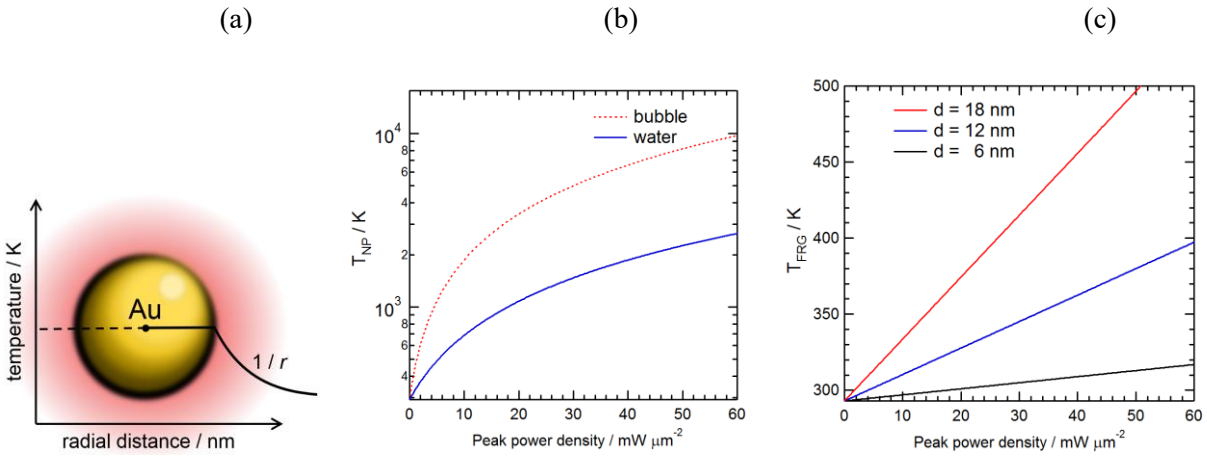

Figure 5-4. (a) Schematic representation of steady-state heating of a single Au NP immersed in a homogeneous medium. (b) Relation between the peak power density and T_{NP} calculated by eq 1 for a 150-nm-diameter Au NP in the bubble and water. (c) Relation between the peak power density and T_{FRG} calculated by eq 1 for fragments of Au NP in the bubble.

Figure 5-4b shows the excitation intensity dependence of T_{NP} in the matrix consisting of water/glass (blue solid line) and in the bubble/glass (red break line). In water/glass, T_{NP} linearly increased with an increase in peak power density, and reached the melting point of bulk gold ($T_{m.p.}$: 1337 K) at I = 28 mW μm^{-2}. As was shown in the previous section, the formation of the bubble was clearly confirmed at the peak power density ≥ 10 mW μm^{-2}. T_{NP} in the calculation at the peak power intensity of 10 mW μm^{-2} is 686 K, which is well above the spinodal temperature of water. Under CW illumination, it has been reported that the bubble formation takes place at the kinetic spinodal temperature, which is rather around 500 K.[22] The threshold temperature on the bubble formation in the present case seems to be overestimated compared with that of the literature[22], probably due to the resolution limit of optical imaging. In the experiment, the numerical aperture of the microscope objective employed is 0.75, which is not so high. It should be mentioned that the small nanobubbles invisible in transmission images were reported to appear at temperatures around 500 K[18,19]. Hence, as mentioned in the previous section, nanobubbles smaller than the diffraction-limited size might be produced at temperature range from 500 to 600 K (*i.e.*, I = 5 - 10 mW μm^{-2}). Accordingly, we conclude that our calculation on T_{NP} in water supports the mechanistic aspects on the bubble formation at temperatures around the kinetic spinodal temperature.[22]

After the bubble is generated, the Au NP is thermally insulated from water due to a poor thermal conductivity of the bubble, resulting in the huge T_{NP} jump[15]. Precise calculation of the T_{NP} jump in the bubble permits to estimate proper temperatures at the bubble surface, which is important for computational modeling of fluid convection. Effective thermal conductivity of 0.2 W m^{-1}K^{-1} was reported[37,39] for the steady-state optical heating of a single Au NP in the stationary bubble supported on the glass substrate. In addition, the absorption cross section of a single Au NP in a bubble, C_{abs}, is largely different owing to the change in the surrounding environment and its temperature. Hence, we calculated T_{NP} in the stationary bubble, by taking into account the effective thermal conductivity of 0.2 W m^{-1}K^{-1} and refractive index of 1.12 for the surrounding environment consisting of the bubble and the glass substrate. The red dotted curve in Figure 5-4b shows that, at the threshold of bubble formation (10 mW μm^{-2}), T_{NP} jumps from 686 to 2000 K. In the excitation intensity range from 10 to 60 mW μm^{-2}, maximum T_{NP}

reached 7000 K which is much higher than the boiling point of gold ($T_{b.p.}$: 3129 K). At such high temperatures, thermal induced morphological changes of an Au NP are induced under laser irradiation [15,46]. In our previous work, the dynamics on the CW laser-induced morphological changes of a single Au NP was investigated by means of light scattering micro-spectroscopy and scanning electron microscopy[39]. From this study, it was revealed that the dynamics on morphological changes in the bubble can be divided into three steps;

i) At temperatures above $T_{b.p.}$, an original single Au NP was fragmented into a larger core NP and small satellite NPs owing to the evaporation from NP surface within a few milliseconds after bubble formation, ii) After a remarkable progression in evaporation of the core NP within a few seconds, the small fragments whose diameters ranging from 10 to 20 nm remained at the center of stationary bubble, and, iii) Owing to the much smaller C_{abs} of the fragments, a temperature of fragments (T_{FRG}) fell down below the $T_{m.p.}$. As a result, the fragments could work as stable heat sources to maintain the bubble in the steady state.

To estimate the increase in the local temperature for the step iii), collective photothermal effect of fragments in the bubble might be taken into account. It has been reported that infinite arrays of Au NPs exhibit collective photothermal effect in the entire region of the laser spot[43]. For the two-dimensionally dispersed Au NPs such as the fragments on a glass substrate, Baffou et al. provided an analytical formula to evaluate the collective photothermal effect[47]. The formula ζ_2 is represented by $\zeta_2 = p^2 / 3LR$, where p [m] is the interparticle distance of the array, L [m] the characteristic length of the illuminated area, and R [m] radius of the nanoparticle. Smaller values of ζ_2 indicates significant contribution of the collective photothermal effect; for instance, the collective effect is negligible when $\zeta_2 > 1.0$, whereas $\zeta_2 < 0.1$ predicts the temperature distribution similar to that of laser heating of a metal thin film. From our previous investigation on the CW laser-induced fragmentation of a single Au NP in the bubble, we assumed R = 6 nm, p = 14 nm, and L = 400 nm. Applying these values to the equation, one can expect the moderate contribution of the collective effect. However, in principle, the collective effect appears only for the large number of NPs under illumination, such as the infinite periodic array.[47] In the present case, an averaged number of fragments in the bubble was only ca. 20. Although the interparticle distance p is relatively small, we

could estimate minor contribution of the collective photothermal effect owing to this small number. Thus, we neglected the collective effect and we employed eq 5-1 for the temperature calculation of the fragments (T_{FRG}) in the bubble from.

To compute T_{FRG} from eq 5-1, we assumed three typical diameters of the individual fragments (d = 6, 12, and 18 nm), because the nominal diameter of the fragments was obtained to be 12 $\pm$ 6 nm in our previous work[39]. For individual fragments in the bubble, the absorption cross section, C_{abs}, was calculated on the basis of the Mie theory with the temperature-induced damping in LSPR. All parameters to compute T_{FRG} were thus obtained. Figure 5-4c shows the T_{FRG} as a function of the peak power density. T_{FRG} linearly increased with an increase in the peak power density. The temperature increase of a fragment with an 18-nm diameter was several times larger than that for the fragment with a 6-nm diameter, reflecting the diameter dependent C_{abs}. Compared with T_{NP} for an Au NP with a 150-nm diameter as shown in Figure 5-4b, all T_{FRG} values were one order of magnitude lower because of the smaller C_{abs} of fragments. Hence, we conclude that the local temperature at the focal spot of the laser beam increases up to 500 K in the microbubble under intensive CW laser illumination. Thermally-induced fragmentation of Au NPs in the bubble has been already reported for the case of ultrashort pulsed laser[18,19,48] and CW laser[39] excitation. Temperature jump triggered by the bubble formation, however, has not been considered in previous reports on bubble-induced fluid convection. Thus, the local temperature increase in the stationary bubble under CW laser illumination was estimated on the basis of steady-state heat conduction equations.

Direct Detection of Fluid Convection around the bubble.

Using wide-field fluorescence microscopy of fluorescent (FL) beads, fluid convection around the bubble was directly detected. Figure 5-5 shows a series of snapshots on the formation of a bubble and subsequent fluid convection at the 532-nm excitation intensity of 40 mW μm^{-2}. Before the irradiation by the focused 532-nm CW laser, Brownian motion of FL-beads was observed as shown in Figure 5-5a. Once the bubble was produced by CW laser irradiation, individual FL-beads started to move toward the bubble (Fig. 5-5b and -c) and, a few second after the bubble formation, FL-beads exhibited a ring-like structure with a 3-μm diameter around the focal spot of 532 nm CW laser (Fig. 5-5d and -e). After forming the ring-like structure, the number of FL-beads gradually increased at the interface between water and the bubble, while keeping almost constant diameter of the ring-like structure (Fig. 5-5e to –h). These images clearly show spatial and temporal profiles of fluid convection around the bubble in such a manner that it whirls from the glass surface to the upper part of the bubble as depicted in Scheme 1c.

So as to more quantitatively elucidate the convention, we have evaluated the convective velocity of FL-beads by tracking the location of individual fluorescence spots for each frame in the movie. As stated in the previous section, in the region within 20 μm in radial distance from the bubble center, the motion of FL-beads could not be detected at the excitation intensities larger than 40 mW μm^{-2} owing to the convective velocity much faster than the time resolution of the fluorescence imaging. Accordingly, we measured the average velocity between the radial coordinates r = 40 and r = 20 μm. Figure 5-5i shows the dependence of the convective velocity on the peak power density. At peak power densities < 10 mW μm^{-2}, no clear convective motion of FL-beads was detected as already mentioned in previous sections. The velocity at the threshold peak power density (I = 10 mW μm^{-2}) of microbubble formation was 20 μm s^{-1} and it increases with increasing peak power density in the range of 10 to 30 mW μm^{-2}. In the range above 45 mW μm^{-2}, the convective velocity gradually saturated and reached 500 μm s^{-1}.

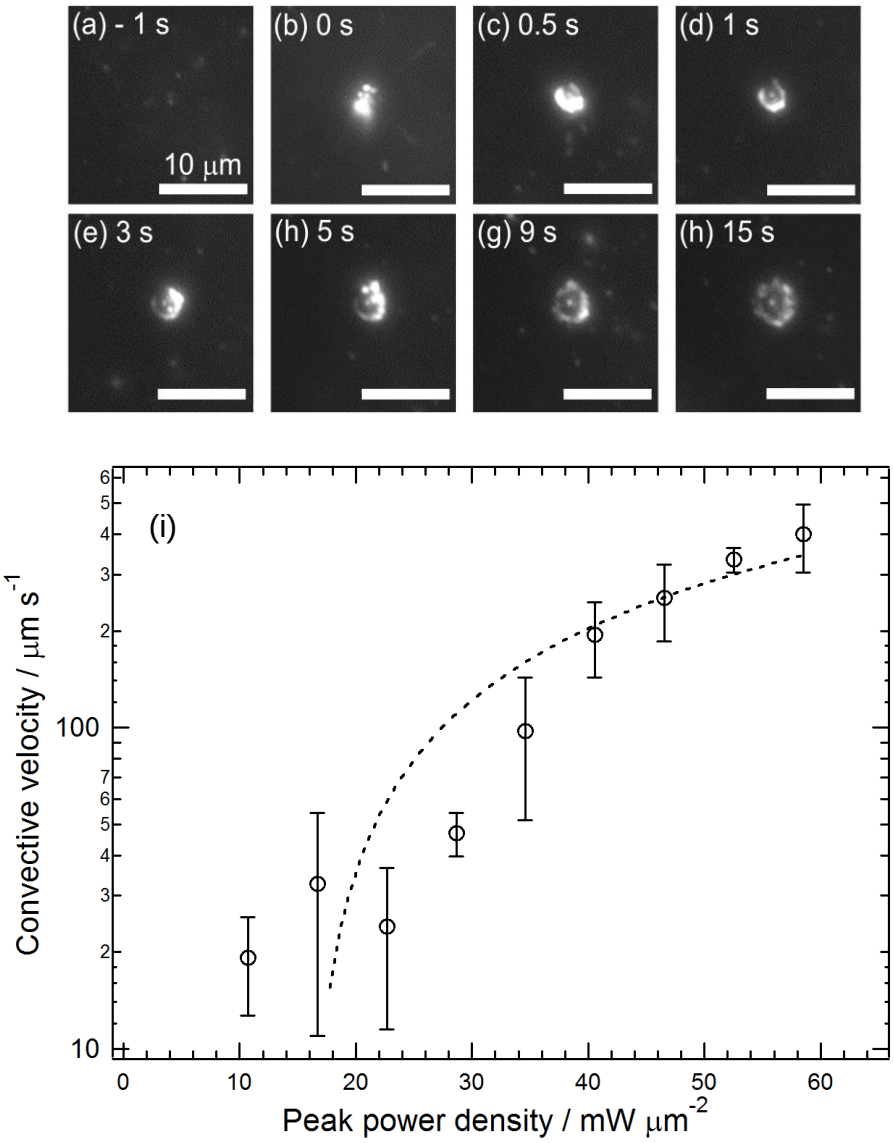

Figure 5-5. (a-h) A time course of fluorescence images of FL-beads around the stationary bubble at the laser peak power density I = 40 mW μm^{-2}. (i) The convective velocity as a function of laser peak power density determined with wide-field fluorescence imaging of FL-beads. The dotted black line is included as a visual guide.

Figure 5-6a, -b, and –c show the optical images observed after the laser irradiation at an excitation intensity of 40 mW μm^{-2} at 532 nm for 30 s. In all the optical images, a ring-like structure with the diameter similar to each other was observed at the position where the bubble existed. Since the ring-like structure could be clearly observed also in the fluorescence image, it is indicated that this ring-like structure consists of FL-beads. The excitation intensity dependence of the diameter of the ring-like structure is plotted in Fig. 5-6d, showing that the diameters increase with the peak power density with no remarkable difference among the three methods of detection. Notably, the excitation intensity dependence of the diameter of the ring-like structure is almost identical with that of the bubble diameter observed in transmission image shown in Fig. 5-2d. This similarity allows to estimate a contact angle of the bubble on the glass substrate for the computational modeling of fluid convection. Although fabrication of a ring-like structure by bubble-induced convection has been already demonstrated[31–33], the formation process of the ring-like structure was monitored only by static imaging methods with a lower time resolution. In the present work, fluid convection around the microbubble was clearly observed by wide-field fluorescence imaging of FL-beads with time resolution sufficient to detect its dynamics: especially from a viewpoint on the excitation intensity dependence of the convective velocity and the bubble diameter. It is worth mentioning that, within a small space, the driving force of the motion for small objects is not limited only to fluid convection. For instance, radiation pressure and thermophoresis should be generally taken into account. In the present irradiation condition of the CW laser, however, the radiation pressure is negligible because the bubble formation was indispensable to induce the motion of FL-beads. Moreover, it has been reported that the thermophoretic force acting to nanoparticles in the temperature gradient is less than a few pico-Newton,[49] of which value is much smaller than the drag force of fluid convection. Hence, we conclude that the motion of FL-beads around the bubble is driven by Marangoni convection.

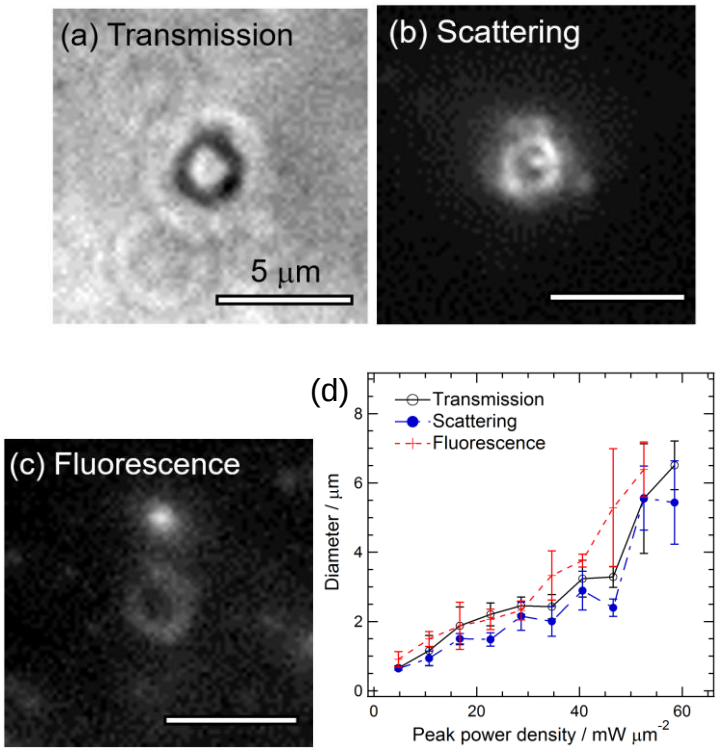

Figure 5-6. Optical microscope images of ring-like structures monitored after laser irradiation at $I = 40$ mW μm^{-2}: (a) transmission, (b) scattering, and (c) fluorescence. (d) Relationship between laser peak power density and the diameter of a ring-like structure obtained with transmission, scattering, and fluorescence imaging

Analysis of the fluid convection.

In this section, we show results of the fluid convection around the bubble on the basis of heat transfer and Navier-Stokes equations. As already mentioned in the introductory part, fluid convection is divided into natural convection and Marangoni one. Because the contribution from the natural convection has been reported[28,29] to be much smaller than that from the Marangoni one and, in actuality, the small contribution from the natural convection was quantitatively evaluated (See details, Figure 5-11), we have assumed that the Marangoni convection entirely dominates the fluid convection around the bubble. As already discussed in previous sections, tightly focused 532-nm CW laser induces an increase in the local temperature around an Au NP and a bubble is produced in water (Scheme 5-1a and -b). The temperature in the bubble is dependent on the distance from the Au NP. The highest temperature is attained at the focal spot of laser, while the surface temperature at the top of the bubble is the lowest due to the long distance from the heat source. The temperature difference in the bubble induces the gradient in the surface tension at the bubble surface and a large temperature coefficient of the surface tension gives rise to a strong shear force at the bubble surface[50]. This temperature dependent shear force at the bubble surface is an origin of Marangoni convection (Scheme 5-1c). Accordingly, temperature gradient at the bubble surface is essential for the analysis on the basis of heat transfer and Navier-Stokes equations.

Navier-Stokes equation is given by[51],

$$-\eta \nabla^2 \mathbf{u} + \rho \mathbf{u} \cdot \nabla \mathbf{u} + \nabla p = \mathbf{F} \qquad (5\text{-}2)$$

$$\nabla \cdot \mathbf{u} = 0 \qquad (5\text{-}3)$$

where η [kg m^{-1}s^{-1}], ρ [kg m^{-3}], $\mathbf{u}$ [m s^{-1}], and p [Pa] are respectively the dynamic viscosity, the density, the velocity vector, and the pressure. The $\mathbf{F}$ term represents external forces per unit volume. Temperature field for eqs 5-2 and 5-3 is given by[51] the following equation,

$$\nabla \cdot \left(-k\nabla T + \rho C_p T\,\mathbf{u}\right) = Q \qquad (5\text{-}4)$$

Here, k [W m^{-1}K^{-1}], C_p [J kg^{-1} K^{-1}], and Q [W m^{-3}] are respectively the thermal conductivity, the heat capacity, and the heat source term. As confirmed in the experiment results in previous sections, the bubble diameter and the convective velocity were in the stationary state under the laser irradiation. In the actual calculation, we numerically solve these equations using the finite element method (FEM)[51]. A contact angle of the bubble on the glass substrate was determined from experimental results. At the maximum temperature (T_{FRG}) in the bubble shown in Fig. 5-4c, a large number of fragments were produced. For the treatment of the fragmented NPs, a point heat source was assumed for the source term Q in eq 4 in this FEM analysis.

Figure 5-7a shows the 2D geometry for FEM analysis. The geometry consists of a glass substrate, water, a bubble, and a point heat source. The height of water domain (H_{water}) was set to 300 μm, which is the same as the thickness of silicone rubber spacer used in the experiment. Other heights and widths were determined considering Rayleigh number. The point heat source was put at the position of the single NP. A contact angle of the bubble on the glass substrate was estimated to be 140^{o} on the basis of experimental results. In this FEM analysis, computational variables were only two: input energy for the heat source and the bubble diameter. Physical constants of the domains are summarized in Table 5-1. For the calculation of temperature field, the boundary condition of a room temperature (293 K) was set at the all outer boundaries. To calculate Marangoni convection, a shear force represented in eq 5-5 was applied at the bubble surface. A temperature derivative of the surface tension of water is -1.6×10^{-4} [N m^{-1} K^{-1}] as shown in Fig. 5-7b. For other boundaries in water domain, $u = v = 0$ (no slip) was applied. Eqs 5-3, 5-4, and 5-5 were numerically solved with COMSOL multiphysics (https://www.comsol.com/), which is a commercially available finite element method (FEM) solver.

$$F = \begin{pmatrix} \tau_x \\ \tau_y \end{pmatrix} = \begin{Bmatrix} \gamma \dfrac{\partial T}{\partial x} \\ \gamma \dfrac{\partial T}{\partial y} \end{Bmatrix} \qquad (5\text{-}6)$$

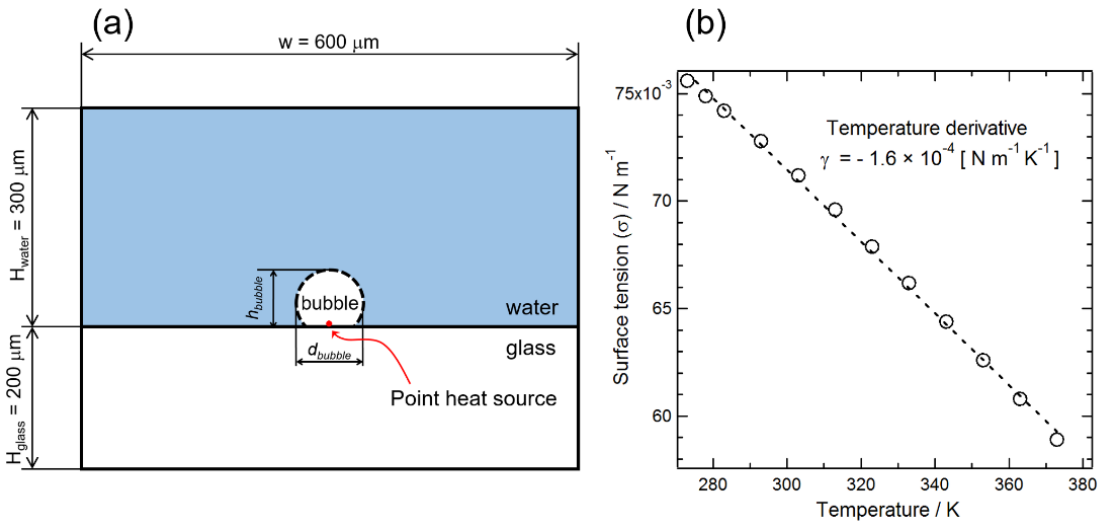

Figure 5-7. (a) FEM geometry and (b) temperature derivative of surface tension of water.

Table 5-1. Physical constants for FEM analysis (at room temperature)

	Thermal conductivity [W $m^{-1}K^{-1}$]	Density [kg m^{-3}]	Dynamic viscosity [Pa s]	Heat capacity [J $kg^{-1}K^{-1}$]
water	0.6	998	0.84×10^{-4}	4180
bubble (air)	0.024	1.2	0.18×10^{-4}	1020
glass	1.0	2650	N/A	860

Figure 5-8a shows 2D temperature distribution calculated for the peak power density at 46 mW μm^{-2} and the diameter of the bubble at 8.6 μm (corresponding to the results in Figures 5-2 and 5-4), indicating that the temperature is highest, 440 K, at the center of the bubble and lower temperature is observed at the surface area. Moreover, the surface temperature at the top of the bubble is slightly lower than the interfacial region between water and the glass substrate. To more precisely clarify the temperature gradients, we plotted temperature profiles along *x*-coordinate at various heights (*y*-distance) from the glass surface (Fig. 5-8b). Whereas a steeper temperature gradient is observed within the initial 10 nm, the temperature in the bubble decreases with an increase in the *y*-distance to 500 nm. At the surface, temperature was ca. 300 K. Outside the bubble, temperature gradually decreased with *x*-distance at each *y*-distance, and reached the room temperature (293 K) at an *x*-distance of 100 μm. Significant reductions in the temperature gradient outside the bubble is ascribable to the higher thermal conductivity of water (0.6 W $m^{-1}K^{-1}$) compared with that of air (0.024 W $m^{-1}K^{-1}$). Govorov *et al.* have provided analytical solutions to calculate the 1D steady-state heat conduction for a system consisting of a single NP, polymer shell layer, and a surrounding liquid medium[43]. In this case, the temperature gradient in a polymer matrix was proved to be steeper than that in a medium owing to a poor thermal conductivity of the polymer. Thus we have concluded that the computational results of 2D temperature distribution are consistent with the heat conduction theory. At the same time, the 2D distribution of convective velocity was obtained on the basis of temperature calculation.

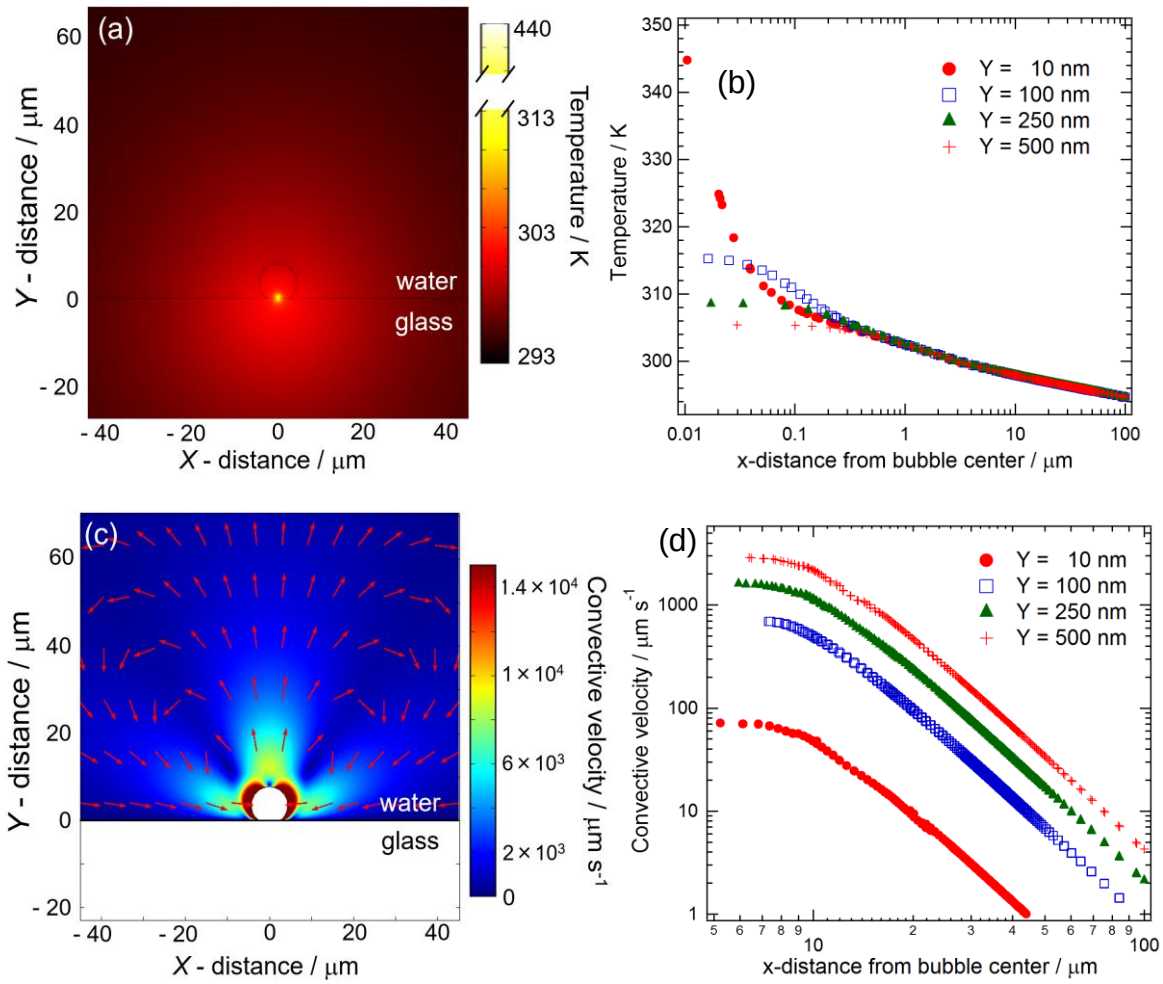

Figure 5-8. Computational 2D temperature distribution (a), and velocity field (b) for the system consisting of the bubble with a 8.6-μm diameter, water, and the glass substrate: The peak power density of 46 mW μm^{-2} was applied. (c) Temperature profiles along *x*-axis at various *y*-distances obtained from 2D temperature distribution. (d) Velocity profiles along *x*-axis at various *y*-distances obtained from 2D velocity field.

Figure 5-8c shows the calculated 2D distribution of the convective velocity. Red arrows in the figure indicate normalized velocity vectors. The whirling motion of convection flow around the bubble was clearly shown by the velocity vectors; this result well reproduces the experimental one on the convective motion of FL-beads observed by wide-field fluorescence imaging (Fig. 5-5). Figure 5-8d shows the velocity profiles along *x*-axis at various *y*-distances, indicating that the convective velocity monotonically increased with y-distance. While the convective velocity larger than 1.0×10^4 μm s^{-1} was observed at the position adjacent to the bubble surface owing to the huge temperature gradient (Fig. 5-8c), it decreased to 10 μm s^{-1} with increasing *x*-distance up to several tens of micrometers. This drastic decrease in the velocity at a longer *x*-distance well agrees with the experimental result that the convective motion of FL-beads was only detectable within 40 μm from the bubble center in radial distance. As shown above, numerical simulation revealed the strong x-distance dependence of the convective velocity with 4 orders of magnitude. From Figure 5c, we can safely conclude that the permanent sticking of FL-beads observed in Figure 5-6 is due to strictly localized velocity maximum being in contact with the bubble, which markedly differs from the situation of natural fluid convection (see Figure 5-11).

In order to comprehensively elucidate the driving force of Marangoni convection, we investigated the excitation intensity dependence of the convective velocity for the bubble with a 8.6-μm diameter. Figure 5-9a shows the temperature calculated at three points; the point heat source, the top of the bubble, and the bottom, under various peak power densities. The temperature at the heat source linearly increased up to 500 K with an increase in the peak power density. In contrast, the temperature at the top and bottom of the bubble increases only by less than 10 K from the room temperature (293 K). As already discussed in the previous section, these temperature differences arose from the disparity in thermal conductivities of the materials.

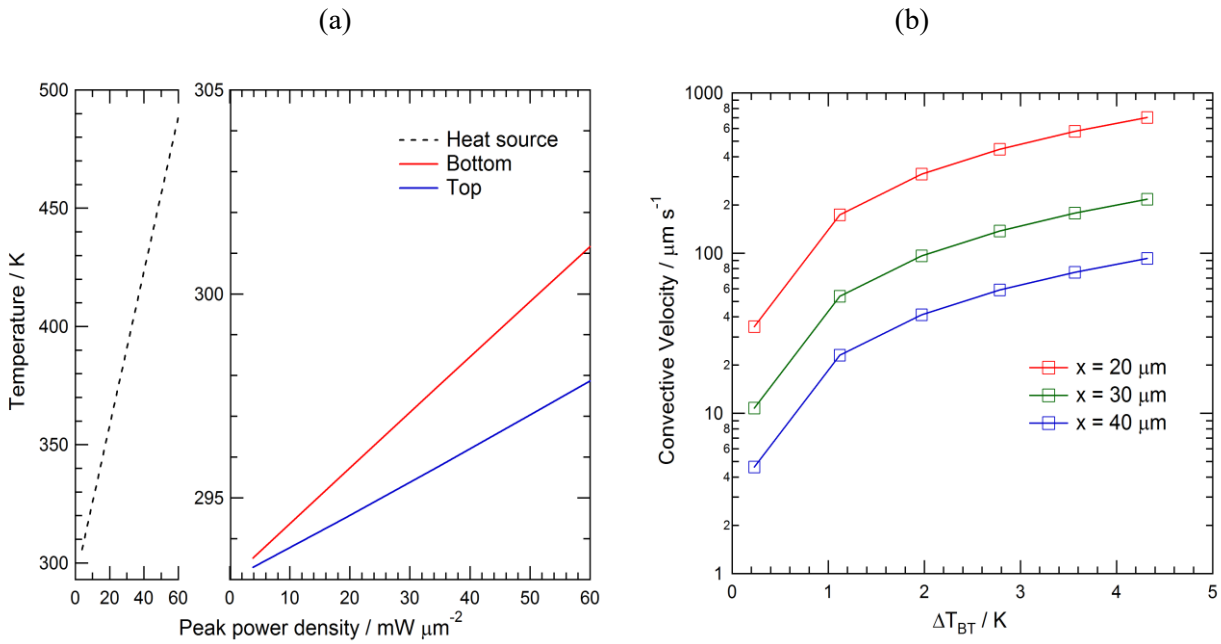

Figure 5-9. (a) Calculated temperatures at the heat source, the bottom of the bubble, and the top of the bubble as a function of laser peak power density for the bubble with a 8.6-μm diameter. (b) Convective velocities *vs* ΔT_{BT}, calculated at the constant *y*-distance of 500 nm for three different *x*-distances.

Because the increase in the temperature at the top and the bottom of the bubble is small, the difference in the temperature between the top and bottom of the bubble (ΔT_{BT}) is not large. The maximum ΔT_{BT} was only 4 K even at a peak power density of 60 mW μm^{-2} in this calculation. As stated in previous sections, Marangoni convection is quite sensitive to ΔT_{BT} because the shear force is strongly dependent on the temperature gradient at the bubble surface. To quantitatively elucidate the effect of ΔT_{BT}, excitation intensity dependence of convective velocity was examined. Figure 6c shows the convective velocities at the constant *y*-distance of 500 nm and various *x*-distances as a function of ΔT_{BT}. In this plot, ΔT_{BT} was obtained from the calculated result shown in Figure 5-9b. At all *x*-distances, the convective velocity increases to 1.0×10^2 μm s^{-1}, as ΔT_{BT} increases to 4 K. In the calculation at ΔT_{BT} = 3.4 K (= 46 mW μm $^{-2}$), the convective velocities for the *x*-distance of 40, 30, 20 μm were respectively 40, 90, and 280 μm s^{-1}. On the other hand, a similar convective velocity of 250 ± 67 μm s^{-1} was obtained at the

same peak power density of 46 mW μm^{-2} in the experiment. The agreement in the convective velocities between the experimental and calculated results supports that the fluid convection around the bubble is mainly regulated by the small ΔT_{BT}, which is less than several Kelvin at the bubble surface.

To more clearly confirm the role of ΔT_{BT}, we investigated the relation between the convective velocity and the size of the bubble. Diameters and contact angles of the bubble for the numerical simulation were determined by referring the experimental results in the present work. Temperature at the point heat source as a function of peak power density was estimated from Fig. 5-4c for each bubble diameter. As performed in previous sections, 2D numerical simulation on heat transfer and fluid convection was carried out. Figure 5-10a shows the convective velocities at a constant *y*-distance of 500 nm and three *x*-distances as a function of the bubble diameter. Experimental results are also plotted for the comparison. Convective velocities at each *x*-distance noticeably increased as the bubble expanded to 10 μm in diameter. Further expansion in the bubble diameter resulted in a gradual saturation of the convective velocity around 1.0×10^3 μm s^{-1}. Experimental plots are reproduced by the calculated convective velocity at a *x*-distance of 20 μm. In particular, the characteristic rise of experimental results is well reproduced by the calculated curve in the diameter range from 2 to 10 μm.

To elucidate an origin of the gradual saturation in convective velocity, ΔT_{BT} between the top and bottom of the bubble was extracted from Fig. 5-10a. Figure 5-10b shows ΔT_{BT} as a function of the bubble diameter. ΔT_{BT} increased 2.4 K to 2.8 K as the bubble expanded to 10 μm in diameter. In contrast, an increase in ΔT_{BT} was not remarkable at the bubble diameters larger than 10 μm, indicating that the gradual saturation in convective velocity is due to the bubble diameter dependence of ΔT_{BT}. This result confirms again that the Marangoni convection is sensitive to the small difference of ΔT_{BT}.

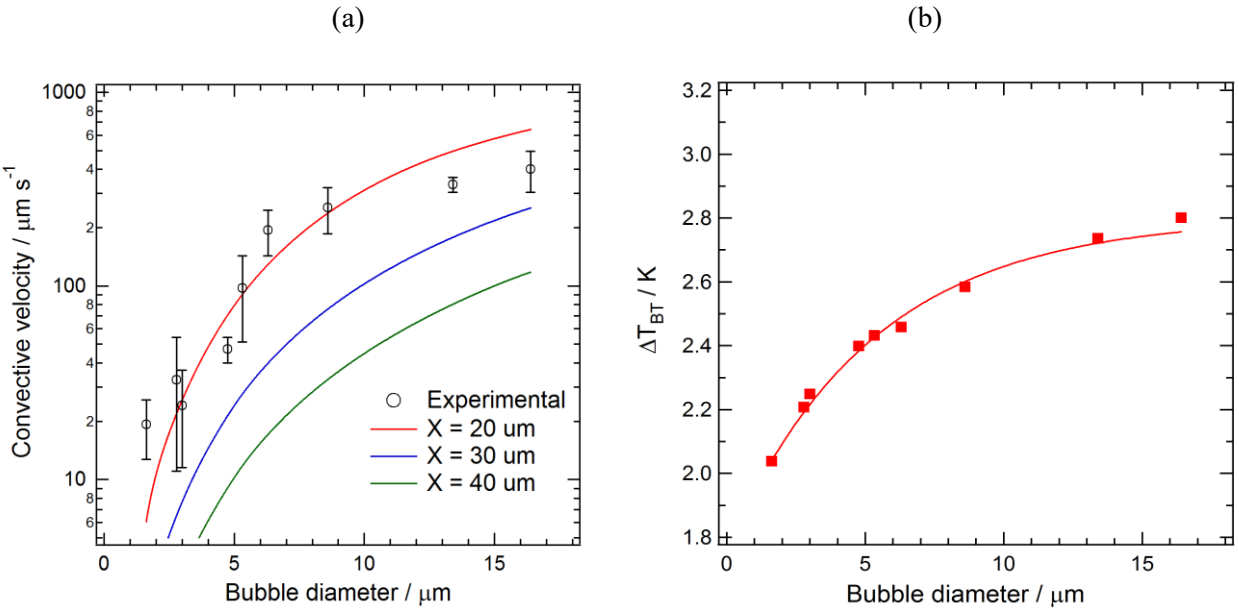

Figure 5-10. (a) The convective velocity as a function of the bubble diameter at *y*-distances of 500 nm, calculated for three different *x*-distances. Experimental data is also plotted together. (b) ΔT_{BT} at the bubble surface as a function of the bubble diameter calculated from Fig. 5-10a.

Finally, we show computational results of the natural convection to quantitatively compare with Marangoni convection. To calculate the natural convection, the same geometry shown in Figure 5-7 was used. However, the shear force applied at the bubble surface was canceled to clarify the contribution of natural convection. Instead, a volume force to describe the buoyancy force in water domain is given by[29]

$$F = \begin{pmatrix} F_x \\ F_y \end{pmatrix} = \begin{Bmatrix} 0 \\ \alpha g \rho (T - T_{ref}) \end{Bmatrix} \qquad (5\text{-}7)$$

where α [K^{-1}] is the thermal expansion coefficient of water, g [$m\ s^{-2}$] gravitational acceleration, ρ [$kg\ m^{-3}$] density of water, and T_{ref} [K] the reference temperature (room temperature, in this case). The temperature dependence of α was not considered. In the calculation, the bubble diameter was fixed at 8.6 μm, and accordingly the computational

variable was only the surface temperature of the bubble. Figure 5-11a and -b show 2D temperature distribution and corresponding velocity field at a fixed bubble temperature of 373 K. The 2D temperature distribution in Figure 5-11a shows the concentric temperature gradients from the bubble center. The corresponding convective flow whirls in water domain as shown in Figure 5-11b, which is typical flow of the natural convection[29]. The highest convective velocity, 40 μm s^{-1}, was obtained at x-distance of 0 μm and y-distance of 120 μm (around the center of the water domain). In addition, the convective velocities at the side of the bubble (around x = ± 100 μm and y = 50 μm) were faster than that at other region. Figure 5-11c shows the convective velocities at the center and the side as a function of the bubble temperature (T_{Bubble}). Almost linear behavior in the convective velocity can be ascribed to the constant thermal expansion coefficient of water. Although the utmost bubble temperature of 373 K (the bulk boiling temperature of water) was applied, the convective velocity adjacent to the glass surface was less than 1 to 2 μm s^{-1}. These values are much smaller than those by Marangoni convection and we can safely conclude that the contribution of natural convection is negligible.

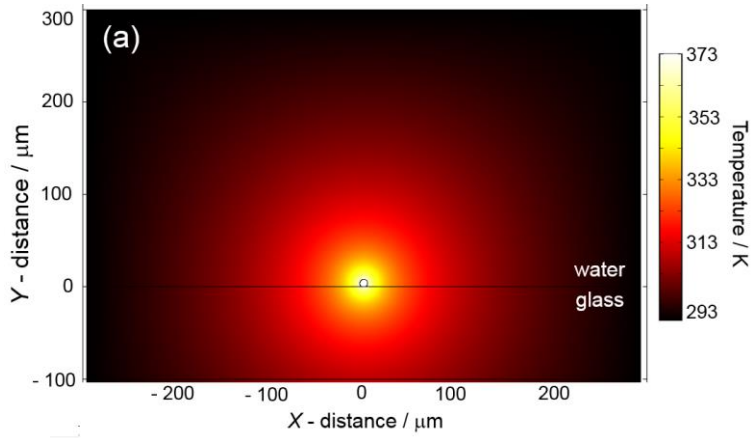
(a)
water
glass
Y - distance / μm
X - distance / μm
Temperature / K
373
353
333
313
293
300
200
100
0
- 100
- 200
- 100
0
100
200

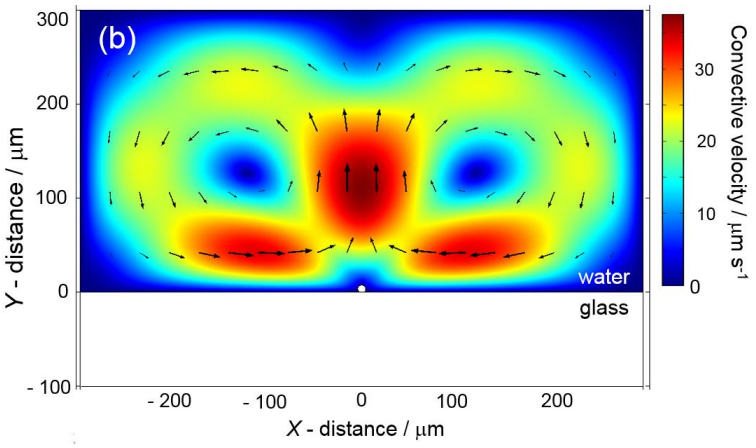
(b)
water
glass
Y - distance / μm
X - distance / μm
Convective velocity / μm s-1
30
20
10
0
300
200
100
0
- 100
- 200
- 100
0
100
200

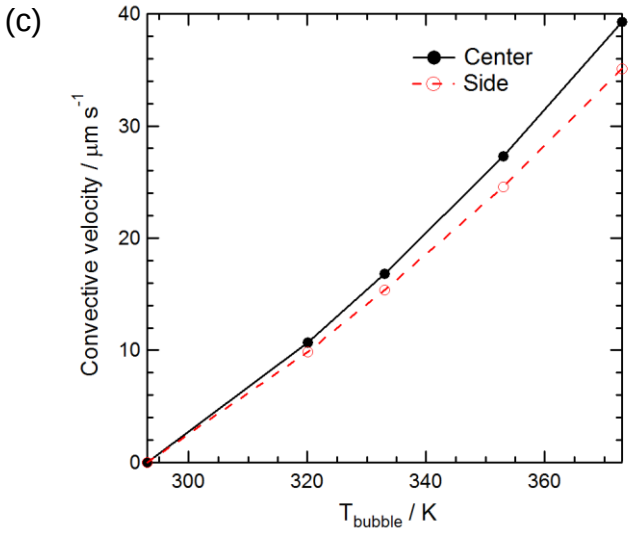
(c)
Center
Side
Convective velocity / μm s-1
Tbubble / K
40
30
20
10
0
300
320
340
360

Figure 5-11. (a) Computational 2D temperature distribution and (b) velocity field for the system consisting of the 8.6-μm-diameter bubble, water, and the glass substrate. The surface temperature of the bubble was set to 373 K. (c) Calculated convective velocities at the center of water domain and the side of the bubble as a function of the surface temperature of the bubble (T_{bubble}).

5-4. CONCLUSION

In the present study, we have elucidated the following properties of the stationary microbubble and subsequent Marangoni convection under CW laser illumination.

i) The diameter of bubble increased with peak power density.

ii) No detectable convection was observed without the formation of microbubble.

iii) Convective velocity increased to 1.0×10^3 μm s^{-1} with ΔT_{BT} at the bubble surface. Effective convection took place within 100 μm from the bubble center in radial distance.

iv) Once the bubble diameter exceeded a certain size, convective velocity gradually saturated owing to the gradual saturation in ΔT_{BT} at the bubble surface.

v) Owing to lower temperatures at the bubble surface, the contribution of natural convection was minor.

Basically, above findings are also applicable when an aggregates or a thin film consisting of Au NPs is employed as a heat source. The surface temperature of the bubble was estimated to be around 300 K, which is much lower than the bulk boiling point of water. This can be advantageous to assemble or manipulate soft materials which cannot withstand at high temperatures.

REFERENCES

(1) S. Link and M. A. El-Sayed, *Annu. Rev. Phys. Chem.*, 2003, **54**, 331–366.

(2) P. Mulvaney, *Langmuir*, 1996, **12**, 788–800.

(3) N. J. Halas, S. Lal, W.-S. Chang, S. Link and P. Nordlander, *Chem. Rev.*, 2011, **111**, 3913–3961.

(4) K. Watanabe, D. Menzel, N. Nilius and H. J. Freund, *Chem. Rev.*, 2006, **106**, 4301–4320.

(5) K. Ueno and H. Misawa, *J. Photochem. Photobiol. C*, 2013, **15**, 31–52.

(6) X.-M. Qian and S. M. Nie, *Chem. Soc. Rev.*, 2008, **37**, 912–920.

(7) P. L. Stiles, J. A. Dieringer, N. C. Shah and R. P. Van Duyne, *Annu. Rev. Anal. Chem.*, 2008, **1**, 601–626.

(8) H. Inouye, K. Tanaka, I. Tanahashi and K. Hirao, *Phys. Rev. B*, 1998, **57**, 11334.

(9) G. V Hartland, *Chem. Rev.*, 2011, **111**, 3858–3887.

(10) A. O. Govorov and H. H. Richardson, *Nano Today*, 2007, **2**, 30–38.

(11) N. S. Abadeer and C. J. Murphy, *J. Phys. Chem. C*, 2016, **120**, 4691-4716.

(12) D. Boyer, P. Tamarat, A. Maali, B. Lounis and M. Orrit, *Science*, 2002, **297**, 1160–1163.

(13) M. Selmke, M. Braun and F. Cichos, *ACS Nano*, 2012, **6**, 2741–2749.

(14) A. S. Urban, S. Carretero-Palacios, A. A. Lutich, T. Lohmüller, J. Feldmann and F. Jäckel, *Nanoscale*, 2014, **6**, 4458–4474.

(15) S. Hashimoto, D. Werner and T. Uwada, *J. Photochem. Photobiol. C*, 2012, **13**, 28–54.

(16) E. Y. Lukianova-Hleb, X. Ren, R. R. Sawant, X. Wu, V. P. Torchilin and D. O. Lapotko, *Nat. Med.*, 2014, **20**, 778–84.

(17) E. Y. Lukianova-Hleb, Y.-S. Kim, I. Belatsarkouski, A. M. Gillenwater, B. E. O'Neill and D. O. Lapotko, *Nat Nanotechnol.*, 2016, **11**, 525-532.

(18) A. Siems, S. A. L. Weber, J. Boneberg and A. Plech, *New J. Phys.*, 2011, **13**, 043018.

(19) T. Katayama, K. Setoura, D. Werner, H. Miyasaka and S. Hashimoto, *Langmuir*, 2014, **30**, 9504–9513.

(20) E. Lukianova-Hleb, Y. Hu, L. Latterini, L. Tarpani, S. Lee, R. a. Drezek, J. H. Hafner and D. O. Lapotko, *ACS Nano*, 2010, **4**, 2109–2123.

(21) K. Sasikumar and P. Keblinski, *J. Chem. Phys.*, 2014, **141**, 234508.

(22) K. Metwally, S. Mensah and G. Baffou, *J. Phys. Chem. C*, 2015, **119**, 28586-28596.

(23) D. Hühn, A. Govorov, P. R. Gil and W. J. Parak, *Adv. Funct. Mater.*, 2012, **22**, 294–303.

(24) Z. Fang, Y.-R. Zhen, O. Neumann, A. Polman, F. J. García de Abajo, P. Nordlander and N. J. Halas, *Nano Lett.*, 2013, **13**, 1736-1742.

(25) M. T. Carlson, A. J. Green and H. H. Richardson, *Nano Lett.*, 2012, **12**, 1534–1537.

(26) G. Baffou, J. Polleux, H. Rigneault and S. Monneret, *J. Phys. Chem. C*, 2014, **118**, 4890–4898.

(27) M. Wang, C. Zhao, X. Miao, Y. Zhao, J. Rufo, Y. J. Liu, T. J. Huang and Y. Zheng, *Small*, 2015, **11**, 4423–4444.

(28) J. S. Donner, G. Baffou, D. McCloskey and R. Quidant, *ACS Nano*, 2011, **5**, 5457–5462.

(29) B. J. Roxworthy, A. M. Bhuiya, S. P. Vanka and K. C. Toussaint, *Nat. Commun.*, 2014, **5**, 3173.

(30) G. L. Liu, J. Kim, Y. Lu and L. P. Lee, *Nat. Mater.*, 2006, **5**, 27–32.

(31) L. Lin, X. Peng, Z. Mao, W. Li, M. N. Yogeesh, B. B. Rajeeva, E. P. Perillo, A. K. Dunn, D. Akinwande and Y. Zheng, *Nano Lett.*, 2015, **16**, 701–708.

(32) S. Fujii, K. Kanaizuka, S. Toyabe, K. Kobayashi, E. Muneyuki and M. A. Haga, *Langmuir*, 2011, **27**, 8605–8610.

(33) V. I. Yusupov, S. I. Tsypina and V. N. Bagratashvili, *Laser Phys. Lett.*, 2014, **11**, 116001.

(34) Y. Nishimura, K. Nishida, Y. Yamamoto, S. Ito, S. Tokonami and T. Iida, *J. Phys. Chem. C*, 2014, **118**, 18799–18804.

(35) K. Namura, K. Nakajima, K. Kimura and M. Suzuki, *Appl. Phys. Lett.*, 2015, **106**, 43101.

(36) T. Uwada, S. Fujii, T. Sugiyama, A. Usman, A. Miura, H. Masuhara, K. Kanaizuka and M. Haga, *ACS Appl. Mater. Interfaces*, 2012, **4**, 1158–1163.

(37) K. Setoura, Y. Okada, D. Werner and S. Hashimoto, *ACS Nano*, 2013, **7**, 7874–7885.

(38) H. Yamauchi, S. Ito, K. Yoshida, T. Itoh, Y. Tsuboi, N. Kitamura and H. Miyasaka, *J. Phys. Chem. C*, 2013, **117**, 8388–8396.

(39) K. Setoura, Y. Okada and S. Hashimoto, *Phys. Chem. Chem. Phys.*, 2014, **16**, 26938–26945.

(40) P. Keblinski, D. G. Cahill, A. Bodapati, C. R. Sullivan and T. A. Taton, *J. Appl. Phys.*, 2006, **100**, 54305.

(41) L. Hou, M. Yorulmaz, N. R. Verhart and M. Orrit, *New J. Phys.*, 2015, **17**, 13050.

(42) G. Baffou, R. Quidant and C. Girard, *Phys. Rev. B*, 2010, **82**, 165424.

(43) A. O. Govorov, W. Zhang, T. Skeini, H. Richardson, J. Lee and N. A. Kotov, *Nanoscale Res. Lett.*, 2006, **1**, 84–90.

(44) Z. Ge, D. G. Cahill and P. V. Braun, *J. Phys. Chem. B*, 2004, **108**, 18870–18875.

(45) G. Baffou and H. Rigneault, *Phys. Rev. B*, 2011, **84**, 035415.

(46) G. González-Rubio, A. Guerrero-Martínez and L. M. Liz-Marzán, *Acc. Chem. Res.*, 2016, **49**, 678-686.

(47) G. Baffou, P. Berto, E. Bermúdez Ureña, R. Quidant, S. Monneret, J. Polleux and H. Rigneault, *ACS Nano*, 2013, **7**, 6478–6488.

(48) D. Werner, T. Ueki and S. Hashimoto, *J. Phys. Chem. C*, 2012, **116**, 5482–5491.

(49) J. Gargiulo, S. Cerrota, E. Cortés, I. L. Violi and F. D. Stefani, *Nano Lett.*, 2016, **16**, 1224–1229.

(50) N. b. Vargaftik, B. N. Volkov and L. D. Voljak, *J. Phys. Chem. Ref. Data*, 1983, 12, 817–820.

(51) F. Mechighel, M. El Ganaoui, B. Pateyron and M. Kadja, *Proceedings COMSOL Conference*, 2007, Grenoble, France, 24-25.

6. General Conclusion

In this thesis, I described photothermal responses of gold nanoparticles (Au NPs) and their related phenomena under the laser irradiation, as investigated by spatially and temporally resolved measurements and numerical calculations. First, I introduced heat transfer from NPs to the surrounding environments, including gas, liquid, and dielectric substrates. Second, the bubble formation around NPs in liquid media was studied in cases of pulsed and CW laser excitation. Third, I elucidated the spatial distribution of temperature gradients and corresponding convective velocity around a stationary bubble produced by CW laser heating of a single Au NP. Here, I summarize the outcomes and achievements in this thesis as a general conclusion.

After the introductory part in Chapter 1, I described, in Chapter 2, the numerical model that was developed for the spectroscopic thermometry of Au NPs, on the basis of a concentric core-shell model with Mie theory describing optical absorption and scattering of a dielectric nanosphere. The effect of laser heating was taken into account by considering the temperature-dependent dielectric function of gold, and the refractive index of the medium. Spectral damping and blue shifts were mainly attributed to the decrease in refractive index of water, whereas red shifts were observed in air arising from the temperature-dependent intrinsic optical property of gold. From these results, we could quantitatively estimate the particle temperature under continuous irradiation.

In Chapter 3, the photothermal generation of nanoscale vapor bubbles around Au NPs was investigated. Picosecond pump−probe optical measurements directly revealed the dynamics of the formation and evolution of nanobubbles around colloidal Au NPs. The dynamics of nanobubbles was evaluated on the basis of bubble-size-dependent spectral changes. Extinction spectra of nanobubbles with different diameters were simulated by considering a concentric spherical core−shell model within the framework of Mie theory. Results of these studies indicated that the nanobubbles generated around Au NP with a 60-nm diameter under the fluence of 5.2 mJ cm^{-2} had a maximum diameter of 260 ± 40 nm and a lifetime of ca. 10 ns. The combination of fast transient extinction spectral measurements and spectral simulations could provide insights into dynamics of plasmonic nanobubbles.

In Chapter 4, laser-induced heating and thermal equilibration of Au NPs supported on different substrates and immersed in several media were studied. Single-particle spectroscopy was employed to monitor the temperature of NPs under the laser excitation. Because of changes in the refractive index of the surrounding medium through the temperature change, Au NPs shows the change of the spectral shape and extinction maximum. The increase in the temperature is dependent on both the surrounding medium and the supporting substrate. I furthermore modeled the NP temperature using a simplified 1-D heat conduction with an effective thermal conductivity taking into account both substrate and medium. Results calculated by this model were compared with those analyzed by a more detailed 2-D heat transfer calculation. From these results, it was found that a substrate in conjunction with the surrounding media regulated particle temperature. These results clearly indicated the crucial role of the substrate as well as the medium on steady-state heating and heat dissipation in nanoscales.

In Chapter 5, I described the formation of stationary microbubbles and subsequent fluid convection induced by CW laser heating of Au NPs in water. Stationary bubbles with ca. 1 – 20-μm diameter were produced by irradiating individual Au NPs with a CW laser. Spatial profiles and velocity distribution of fluid convection around the microbubbles were visualized by wide-field fluorescence imaging of tracer nanospheres. To evaluate the bubble-induced convection, numerical simulations were performed on the basis of general heat diffusion and Navier-Stokes equations. A comparison of experimental result with computational ones revealed that a temperature derivative of surface tension at the bubble surface was a key factor to regulate the fluid convection. Temperature differences of a few Kelvin at the bubble surface resulted in convective velocities ranging from 10^2 to 10^3 μm s^{-1}. In addition, it was also confirmed that the convective velocity gradually saturated with increasing bubble diameter. From these results, it was demonstrated that manipulation and nanofabrication within a small space could be attained by plasmonic heating of Au NPs.

These studies revealed the fundamental aspects of laser-induced heating and its related phenomena of Au NPs, and could serve as important information for the application of plasmonic heating to nanofabrication and theranostics such as diagnostics and therapy.

Scientific Achievements

Publications Related to This Thesis

1. "Optical Scattering Spectral Thermometry and Refractometry of a Single Gold Nanoparticle under CW Laser Excitation"

○**Setoura, K.**; Werner, D.; Hashimoto, S

J. Phys. Chem. C **2012**, 116, 15458−15466.

2."Observation of Nanoscale Cooling Effects by Substrates and the Surrounding Media for Single Gold Nanoparticles under CW-Laser Illumination"

○**Setoura, K.**; Okada, Y.; Werner, D.; Hashimoto, S

ACS Nano **2013**, 7, 7874-7885.

3. "Picosecond-to-Nanosecond Dynamics of Plasmonic Nanobubbles from Pump−Probe Spectral Measurements of Aqueous Colloidal Gold Nanoparticles"

Katayama, T.; ○**Setoura, K.**; Werner, D.; Miyasaka, H.; Hashimoto, S.

Langmuir **2014**, 30, 9504-9513.

4. "Stationary Bubble Formation and Marangoni Convection Induced by CW Laser Heating of a Single Gold Nanoparticle"

○**Setoura, K.**; Ito, S.; Miyasaka, H.

Nanoscale **2017**, 9, 719-739.

Publications Not Related to This Thesis

5. "Computational Modeling of Pulsed Laser-Induced Heating and Evaporation of Gold Nanoparticles"

Strasser, M.; ○**Setoura, K.**; Langbein, U.; Hashimoto, S.

J. Phys. Chem. C **2014**, 118, 25748-25755.

6. "CW-Laser-Induced Morphological Changes of Single Gold Nanoparticles Supported on a Glass Substrate: Observation of Surface Evaporation"

○**Setoura, K.**; Okada, Y.; Hashimoto, S.

Phys. Chem. Chem. Phys. **2014**, 16, 26938-26945.

7. "Laser-driven phase transitions in aqueous colloidal gold nanoparticles under high pressure: picosecond pump–probe study"

Hashimoto, S.; Katayama, T.; ○**Setoura, K.**; Strasser, M.; Uwada, T.; Miyasaka, M.

Phys. Chem. Chem. Phys. **2016**, 18, 4994-5004.

8. "Two-photon Induced Fast Photoswitching via Electron Transfer in Higher Excited States of Photochromic Imidazole Dimer"

Kobayashi, Y.; Katayama, T.; Yamane, T.; ○**Setoura, K.**; Ito, S.; Miyasaka, H.; Abe, J.

J. Am. Chem. Soc. **2016**, 138, 5930-5938.

Awards

1. “Picosecond Pump-probe Study of Gold Nanoparticles in Aqueous Solution: Excitation Wavelength and Excitation Intensity Effects.”

Poster Prize,

8th Asian and Oceanian Photochemistry Conference 2014,

Asian and Oceanian Photochemistry Association. (November 13, Trivandrum, India)

2. “Photothermal response of gold nanoparticles: single and ensemble particle measurements”

Student Research Award,

The 1st International Symposium on Interactive Material Science Cadet Program,

Interactive Materials Science Cadet Program. (November 19, Suita, Japan)

3. “Light-induced Temperature Increase of a Single Gold Nanoparticle: Driving Thermophoretic Movement and Optofluidics”

CSJ Student Presentation Award 2015,

The 95th CSJ Annual Meeting

The Chemical Society of Japan (March 27, 2014, Funabashi, Japan)

4. “Stationary bubble formation and optofluidics induced by CW laser heating of a single gold nanoparticle”

Photochemical & Photobiological Sciences Presentation Prize,

Annual Meeting on Photochemistry 2015

Royal Society of Chemistry and The Japanese Photochemistry Association. (September 9, Osaka, Japan)

Acknowledgements

I would like to express the deepest appreciation to Prof. Hiroshi Miyasaka of Division of Frontier Materials Science and Center for Promotion of Advanced Interdisciplinary Research, Osaka University, for his advices, encouragement, and stimulating discussions.

I would like to thank Prof. Syoji Ito of Division of Frontier Materials Science and Center for Promotion of Advanced Interdisciplinary Research, Osaka University, for fruitful discussions on scientific problems.

I am deeply grateful to Prof. Shuichi Hashimoto and Dr. Daniel Werner, of the Department of Optical Science and Technology, The University of Tokushima, for their helpful advices and supports.

I am grateful to Prof. Takayuki Uwada of the Department of Chemistry, Josai University, for assistance with the numerical simulations.

I would like to thank to all members in Miyasaka Lab. for their supports and encouragement in my laboratory life and study. At the end, I would like to express my gratitude to my family for their supports throughout my entire life.

KENJI SETOURA

MARCH 2017